The Dissertation Committee for Li-Hsin Han Certifies that this is the approved version of the following dissertation:

Light Driven Microactuators: Design, Fabrication, and Mathematical Modeling

Committee

Shaochen Chen, Supervisor

John R. Howell

Li Shi

Xiaojing Zhang

Wolfgang Frey

Thomas E. Milner

Light Driven Microactuators: Design, Fabrication, and Mathematical Modeling

by

Li-Hsin Han, B.S., M.S.

Dissertation

Presented to the Faculty of the Graduate School of
The University of Texas at Austin
In Partial Fulfillment
Of the Requirements
For the Degree of

Doctor of Philosophy

The University of Texas at Austin
August 2009

Dedication

To my Lord God,
my excellent wife Erica,
my parents, and
my baby girls, Camille and Kaelyn

Acknowledgements

First, I would like to thank my supervisor, Dr. Shaochen Chen, for his guidance and support throughout the years of my study. Special thanks to current Chen group members, Shaomin Wu for his help in building a rarefied gas system and synthesizing nanospheres, Wande Zhang for his help in constructing the DMD system, Wei Wang for his help in developing electrodynamics models, David Fozdar, and Daniel Eils for many fruitful discussions. I would especially like to recognize Shalu Suri and Dr. Christine Schmidt for our great collaboration on cell engineering project and Jonathon Condit and Dr. Thomas Milner for our collaboration on the OCT project, which motivated the study of light-driven turbine. I would also like to thank Dr. Tingji Tang (UT PhD) and Dr. Stephen Webber for teaching me organic synthesis and Jeffrey Easley and Dr. Christopher Ellison for their help in chemical characterization. Special thank to former Chen group members Yi Lu (UT PhD) for initiating the DMD project, Arvind Battula (UT PhD) for his help in developing multiphysics models, Senthil Theppakuttai (UT PhD) for his help learning Nd:YAG laser, Dongbing Shao (UT PhD), Shifeng Li (UT PhD), and Carlos Arguilar for their input, and also for their friendship.

I gratefully acknowledge my committee members: Dr. Thomas Milner, Dr. John Howell, Dr. Li Shi, Dr. Xiaojing Zhang, Dr. Wolfgang Frey, and Dr. Shaochen Chen for their patience and advice.

Light Driven Microactuators: Design, Fabrication, and Mathematical Modeling

Publication No.____________

Li Hsin Han, Ph.D.
The University of Texas at Austin, 2009

Supervisor: Shaochen Chen

This dissertation is concerned with design, fabrication, and mathematical modeling of three different microactuators driven by light. Compared to electricity, electromagnetic wave is a wireless source of power. A distant light source can be delivered, absorbed, and converted to generate a driving force for a microactuator. The study of light-driven microsystems, still at its early stage, is already expanding the horizon for the research of microsystems.

The microactuators of this dissertation include micro-cantilevers driven by pulsed laser, photo-deformable microshells coated with gold nanospheres, and a nano-particles coated micro-turbine driven by visible light. Experimental investigation and theoretical analysis of these microactuators showed interesting results. These microactuators were functioned based on cross-linked, multiple physics phenomenon, such as photo-heating, thermal expansion, photo-chemistry effect, plasomonics enhancement, and thermal

convection in rarefied gas. These multiple physics effects dominate the function of a mechanical system, when the system size becomes small. The modeling results of the microactuators suggest that, to simulate a microscale mechanical system accurately, one has to take account the minimum dimension of the system and to consider the validity of a theoretical model.

Examples of the building of different microstructures were shown to demonstrate the capacity of a digital-micromirror-device (DMD) based apparatus for three-dimensional, heterogeneous fabrication of polymeric microstructures.

TABLE OF CONTENTS

LIST OF TABLES

LIST OF FIGURES

Chapter 1 : Introduction

This dissertation is concerned with design, fabrication, and mathematical modeling of three different microactuators driven by light. The term “microactuator” is defined hereinafter as a mechanical system with a characteristic length below 100 micrometers (µm). A characteristic length is a key dimension important to the major function of the mechanical system.

1.1 Light as Power Source for Microactuators

Started in the 1990’s, the development of microactuators was originated from the semiconductor technology [1]. Standard semiconductor procedures, such as wet-etching and vapor deposition, were used to build microscale components from metals or metal oxides. Following the similar process to build micro-circuits and transistors, metals and metal oxides were pattern, deposited, etched, and released to build microcomponents, such as micro-cantilevers, gears, channels, hinges, coils, electrodes, or magnets [2]. Many studies in this field were industrialized. Commercialized products of semiconductor-based microactuators include the accelerometers for air-bag triggering systems and the inkjet heads for desk-top printers. These microactuators were mostly driven by electricity, so they were generally named as micro-electro-mechanical systems (MEMS).

The requirement of voltage source has limited the applications of MEMS. The connections to a substrate or wirings made it impossible to build a stand-alone system for the applications which require motilities of microsystems. Moreover, because MEMS are normally driven at high voltages, extra efforts to build reliable isolating packaging become necessary, especially for MEMS working in conductive environments.

Compared to electricity, electromagnetic wave is a wireless source of power. A distant light source can be delivered, absorbed, and converted to generate a driving force for a microactuator. For example, a mechanical bending can take place at the boundary between two distinct materials when a bimorph (composite, double-layered) microcantilever is heated by light [3]. The study of a microcantilever driven by light will be discussed at Chapter 2. While photo-heating is a straight forward mechanism, there are many more photoenergetic mechanisms to power a microactuator. For example, photo-chemical reactions can also generate forces; one study using a phenomenon called photoisomerization to build micromachine will be discussed in Chapter 3 [4]. Also, microactuators with photo-voltaic batteries can be driven by voltage without wirings. The study of light-driven microsystems, still at its early stage, is already expanding the horizon for the research of microsystems.

1.2 Polymeric Microfabrication in 3-Dimension

As the dimension of a mechanical system decreases, the chemical properties of a microstructure gradually become dominant to the function of the system. Thus, microstructures built by MEMS technology are sometimes modified with binding chemicals to gain certain chemical properties. For example, silicon dioxide micro-channels for micro-pumping system are normally treated with different silanes to create hydrophobic or hydrophilic channel walls [5]; the surface properties of walls can significantly affect the wetting efficiency of the microchannels by either an aqueous solution or a hydrocarbonate liquid. The chemical modification of metal/oxide microstructures can only reach the surface of microstructure; volumic chemical modification, which is applicable to build, for example, microactuators based on volume expansion/contraction [6], cannot be realized using the semiconductor based materials.

Compared to metals or metal oxides, polymers are inherited with high flexibility in chemical and mechanical properties to build microactuators. Chapter 4 of this dissertation is focused on the fabrication of three-dimensional polymeric microstructure. The author of this dissertation constructed a microfabrication device which includes an active photo-mask. The pattern of this photo-mask is digitally reconfigurable. It forms ultraviolet (UV) images using a UV light source to turn photo-sensitive liquids into rigid layers of microstructures [7]. This apparatus, which is called digital micro-mirror device (DMD) system, allows one to build a microstructure of random geometry at a fast speed. In addition to homogeneous fabrication, the DMD system can also build a microsystem heterogeneously; the materials can be efficiently switched to build microstructures of localized, multiple materials. A microturbine built by two distinct materials will be introduced in Chapter 4. This turbine has different chemical properties at each side of its blades. The difference of chemical properties at the turbine blades enabled a selective coating of gold nanoparticles, which absorb light and generate an angular momentum in diluted air to cause turbine rotation. The study of the polymeric microturbine highlights the potential of using chemical materials to build microactuator.

Also included in Chapter 4 is the synthesis of several special chemicals for 3D, polymeric microfabrication. These materials include hydrolysable monomers, photo-reactive monomers, and a sacrificial material to control the fabrication resolution at Z-axis (direction of microstructure thickness).

1.3 Multi-physics Modeling

The physics behind the functions of the three light-driven microactuators will be explored using theoretical models. Newtonian mechanics [8] will be used as the foundation theory to construct the dynamics of moving objects of a system. Mathematical technique for multidimensional system, such as Lagrangian formula [9], will be applied to handle the Newtonian dynamics of mechanically interacting components, such as the link-and bar model for cantilever beam in Chapter 2. To simulate a dynamics system inherited with high level of uncertainty, statistical Newtonian mechanics will be applied to simulate the system dynamics, using variables generated according to theoretical distributions [10, 11]. In Chapter 4, the modeling of gas dynamics around the light-driven microturbine will be based on a statistical approach, the Direct Simulation Monte Carlo (DSMC) method [12]. The generation of theoretically distributed variables by computer program will be discussed in the last section of Chapter 4.

Electrodynamics based on the Maxwell's equations [13] will be used in Chapter 3 to analyze the optical interaction among multiple nanospheres. Rigorous, analytical solutions for the electromagnetic interactions of single and multiple spheres with light will be used to build the core equations for computer modeling. Mie's scattering theory [14] and also the modified Mie theory [15] will be used to analyze the distribution of electromagnetic field in a multiple-sphere system.

Using mostly analytic calculations, this dissertation aims to highlight the physics behind the functioning of the three light-driven microactuators. Numerical analysis will be either unused or minimized for modeling. For example, a link-and-bar model in Chapter 2 is designed to approach the continuous material property of a bimorph cantilever beam; however, the calculation of the model yields the analytical solutions based on Newtonian and Lagrangian dynamics. In Chapter 3, another numerical approach will be used to approximate the total electromagnetic energy stored at a microshell system; the approximation will be based on analytical calculation of the electric dipoles in each simulated nanosphere.

1.4 References

1. Madou, M. J., 2001, Fundamentals of Microfabrication: the Science of Miniaturization. New York, CRC Press, pp. 1-71.
2. Madou, M. J., 2001, Fundamentals of Microfabrication: the Science of Miniaturization. New York, CRC Press, pp. 77-118.
3. Choi, J.; Yamaguchi, J.; Morales, S.; Horowitz, R.; Zhao, Y.; Majumdar, A., 2003, "*Design and control of a thermal stabilizing system for a MEMS optomechanical uncooled infrared imaging camera,*" Sens. Actuators A, **104**, pp.132–142.
4. Feringa B. L., 2001, Molecular Switches, Wiley-VCH, GmbH, Weinheim, Germany, pp.399.
5. Huang, T.T; Mosier, N.S.; Ladisch, R.L, 2006,"*Surface engineering of microchannel walls for protein separation and directed microfluidic flow*", Journal of Separation Science, 29, 1733-42.
6. Yu, Y. and Ikeda, T., 2005, "*Photodeformable Polymers: A New Kind of Promising Smart Material for Micro- and Nano-Applications*", Macromolecular Chemistry and Physics, **206**, pp. 1705-08.
7. Han, L, et al. 2008, "*Projection Micro-Printing of Three-Dimensional Scaffolds for Tissue Engineering*." Journal of Manufacturing Science and Engineering, **130**, pp. 021005-1-4.
8. H. Goldstein, Classical Mechanics, Addison-Wesley, 1950, p. 347.
9. D. Karnopp, D.L. Margolis, R.C. Rosenberg, System Dynamics—Modeling and Simulation of Mechanical System, Wiley, 2000, pp.124.

10. Garcia, Alejandro L. Numerical Methods for Physics. NJ : Prentice-Hall, 1994. pp. 319-347.
11. Huang, Kerson. Statistical Mechanics. 2. New York : John Wiley & Sons, 1987. pp. 56-59.
12. Bird, G. A. Molecular Gas Dunamics. Oxford : Clarendon Press, 1976. pp. 311.
13. Jackson J D 1999 Classical Electrodynamics 3rd ed John Wiley & Sons, USA, pp. 407-411.
14. Mie, G., 1908, “Beiträge zur Optik trüber Medien speziell kolloidaler Metallösungen,” *Ann. Phys.* **25** 376-445.
15. Mackowski, D. W. 1991 “Analysis of Radiative Scattering for Multiple Sphere Configurations,” *Proceedings: Mathematical and Physical Sciences*, **433** (1889), pp. 599-614.

Chapter 2 : Transient Displacements of Micro-Cantilevers upon Pulsed Laser Heating

2.1 Introduction

Bimorph micro-cantilevers (BMC) are basic components for micro-electromechanical systems (MEMS). A BMC is typically used to convert the energy from a specific power source to a mechanical potential, which produces bending moments and structural deformation. Mechanisms to produce a bending include material phase-change, capacitive-electrical force, and thermal expansion [1–3]. Despite the wide variety of possible mechanisms for bending, most BMCs are electrically powered. Such micro-systems require electric-wiring, which may limit their use due to the difficulties at packaging against a conductive environment, like water, or an enlarged device size.

A possible solution for wireless actuation is to use light as the power source to heat the BMC. This concept has been demonstrated in laser-heated micro-cantilevers for biological detection [4]. A continuous-wave (CW) laser was applied to heat and bias the position of the bimorph micro-cantilevers in water. BMCs were also used to develop photo-detectors where a BMC-array was employed to interact with the heating from an infrared source, such as a human body [5,6]; the intensity distribution of the infrared sources was characterized by the cantilever-deformations at the BMC array. Moreover, a CW laser was applied to actuate micro-mirrors and a micro-cantilever [7,8]. The reported photo-actuations for BMCs were mostly done by using continuous light sources.

When heating a BMC by light, the thermomechanical deformation of the BMC is decided by the heat stored in the BMC. This stored heat is a difference between the rate of photo-heating and the rate of heat-dissipation from the BMC to its surroundings. The amount of stored heat decides what temperature a BMC will have and thus the amount of deformation the BMC can generate.

For some applications, to generate large or fast deformations of BMC using a constant light source, one has either to raise the intensity of light or to reduce the thermal conductivity of the BMC by changing materials. Either way has its problem. For applications that involve temperature-sensitive samples, such as biological cells, large illumination may cause unwanted heating of the samples. As well, a slow dissipation of heat increases the period of thermal cycle at a BMC system and reduces the speed of MEMS.

In some applications of laser heating, such as micro-pumping or micro-propelling, it is more preferable to create pulse-like deformations rather than smooth changes in the microstructure. A pulsed laser is an effective tool to provide the energy for pulse-like deformation. For example, a nanosecond-pulsed laser can deposit a small amount of thermal energy to a microstructure within nanoseconds, before a substantial amount of heat is dissipated. A pulse laser thus creates a high, transient temperature within the microstructure [9]. The sudden increase in the temperature of the microstructure generates structural vibrations, which are a result of a sudden thermal expansion. These effects have been reported in sound generation by high-power laser-heated gas [10]. These photo-thermal vibrations in microstructures are promising for applications of micro-pumping or micro-propelling by MEMS.

In this chapter, we report the experimental and theoretical investigation of pulsed-laser interaction with BMCs which have a gold layer on a polysilicon (poly-Si) layer. A Nd:YAG laser of wavelength of 355 nm and pulse width of 12 ns was used to heat the BMC. The bending of the BMC was optically measured with a displacement detector. To better understand the experimental observation, a 2D discrete model was built to simulate the motion of the BMC induced by short-period heating. Numerical results were compared with the experimental results to reveal the physics mechanisms of laser-BMC actuation.

2.2 Design and Fabrication of Bimorph Micro-cantilever Beams

The design of the BMCs is shown in Figure 2.1. The structure was designed by a Poly-MUMPS® process provided by MEMSCAP. The BMCs are on a silicon substrate coated with a 600 nm silicon nitride layer. The length of the BMCs are 1000, 850, and 500μm, respectively. The bilayer structure is made of a 1.5 μm thick poly-Si layer and a 0.5μm thick Au layer. After release by using buffered hydro-fluoride acid (BHF), it was discovered that the cantilever bended upward because of the internal stress between the two layers (Figure 2.2) The internal stress was a result of different thermal expansion coefficients of the poly- Si and Au layers. The initial bending angle θ of 1000, 850, and 500μm BMCs were approximately 23°, 20°, and 12°.

The experimental setup of a laser-actuated BMC is shown in Figure 2.3. A laser pulse from a Nd:YAG laser (“heating laser”, wavelength = 355 nm, pulse width = 12 ns) was delivered to the top gold layer to heat the BMCs. A beam splitter was used to deliver a portion of the laser to an energy detector to measure the laser power. To detect the movement of the BMC, a commercial diode laser displacement sensor (DLD sensor, MICROTRAK®)was used. The DLD sensor included a diode laser (CW) of wavelength at 635 nm and a position sensitive diode (PSD) module. The diode laser (“probing laser”) probed the bending of BMCs heated by the heating laser. The reflected probing laser beam was collected by the PSD module. The PSD module has a position-sensitive diode, which is sensitive to the projected location of the reflected probing laser beam. When the sample (cantilever) surface moves, the reflected laser spot was shifted and the resistance of the PSD changes. A central unit of the DLD sensor analyzes the variation of the PSD resistance and calculates the distance from the BMC surface to the PSD. To optimize the detecting signal, the angle β between the surface gold layer and the DLD sensor, (Figure 2.4), was set to 40°, the angle at which most of the incident energy of the diode laser could be reflected to the PSD. The DLD sensor has a port to output a voltage proportional to the distance measured. The range of the output voltage is ±5V, corresponding to the range of the DLD sensor, ±1.25 mm. We used an oscilloscope with a 500MHz bandwidth and a 1 GSa/s sampling rate operated on single-shot acquisition mode (1 ns time resolution) to receive the voltage and to generate a displacement waveform in real time. A CCD-coupled microscope was used to monitor the laser spots to ensure that both the heating laser and the probing laser spots were targeted on the BMC.

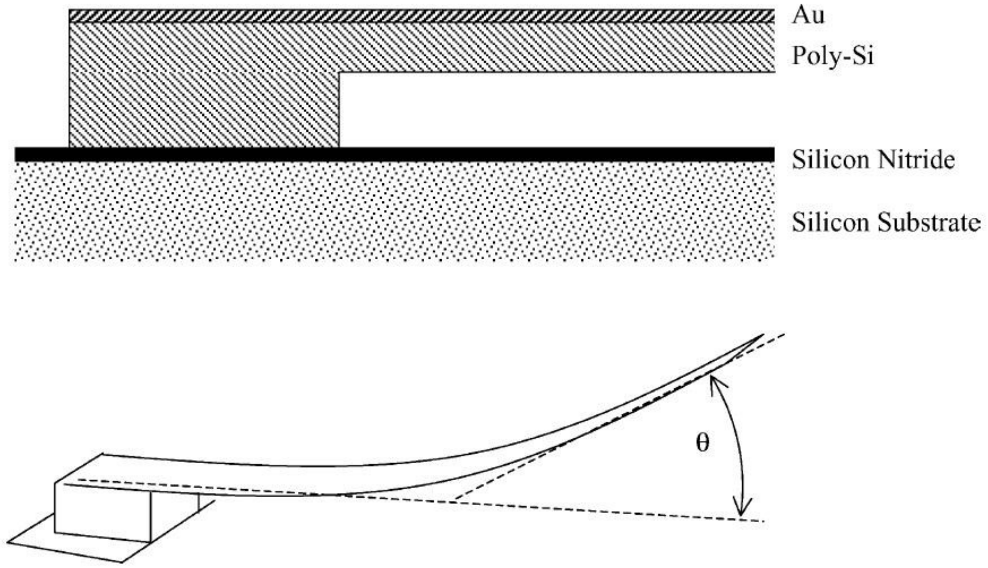

Figure 2.1 Schematic diagram of a BMC.

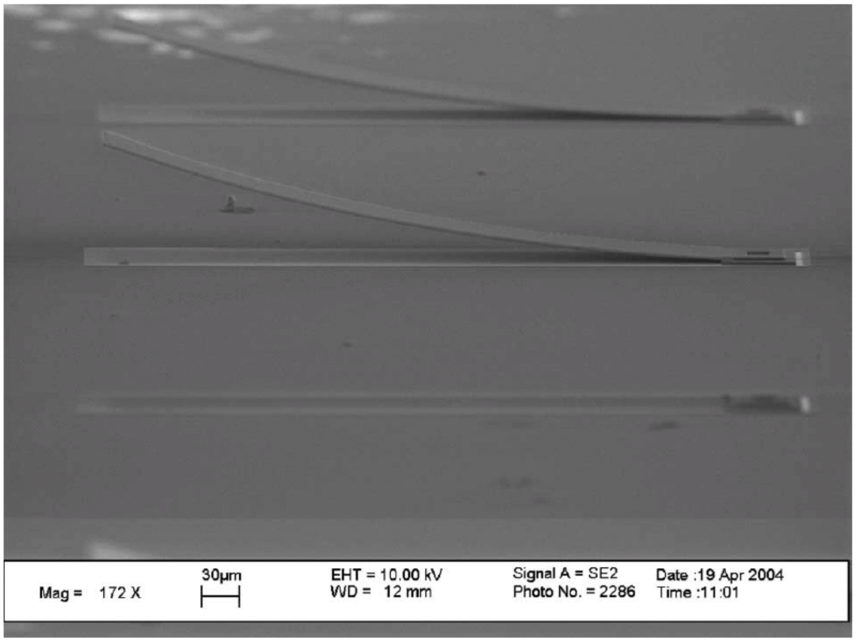

Figure 2.2 SEM picture of the BMCs with initial bending.

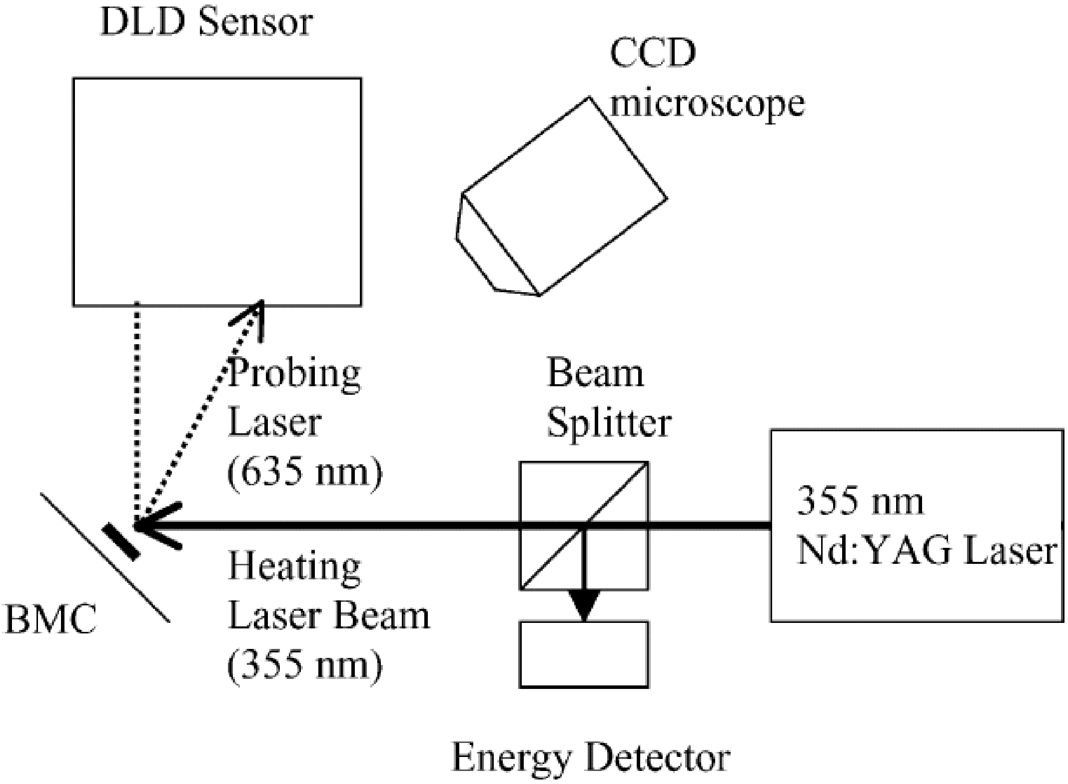

Figure 2.3 This figure shows the experimental setup to measure laser-actuated motions at BMCs. The 355 nm Nd:YAG laser is for BMC actuation, while the 635 nm diode laser is for displacement detection.

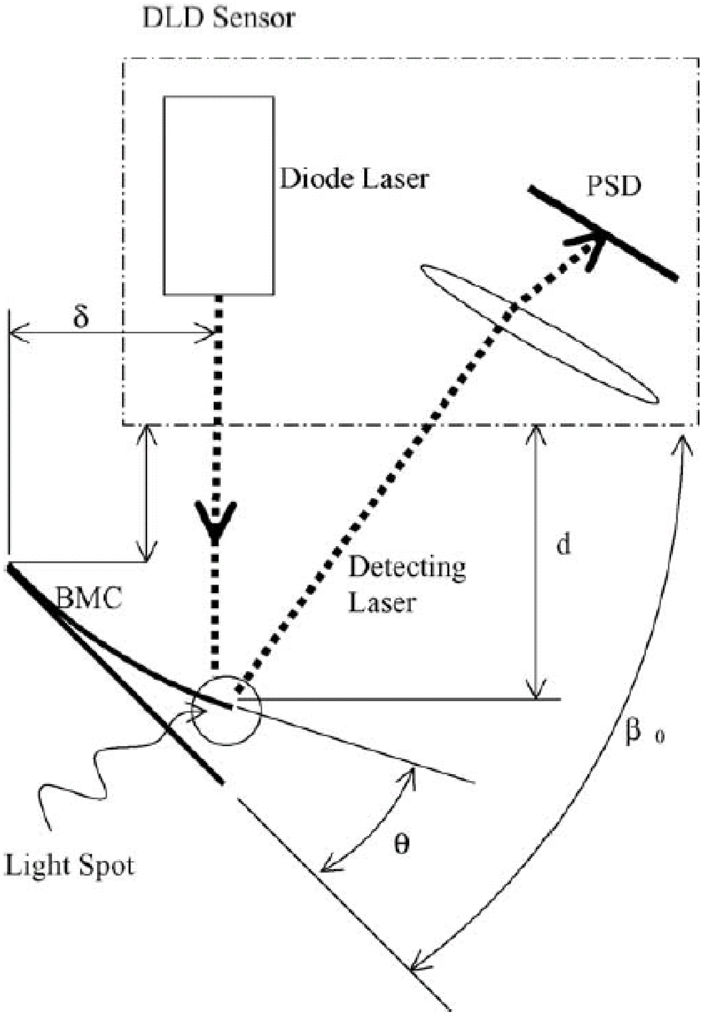

Figure 2.4 Components of the diode laser displacement sensor system (DLD). It detects the distance d in real time. θ is the bending angle of the BMC and δ the horizontal distance from the BMC base to the light spot. The angle β was about 40˚ at which most of the energy from the laser spot could be reflected to the PSD module. These values have also been used for the simulation of BMC vibration.

2.3 Finite-Element Model to Simulate the Thermomechanical Effect at BMC

Bernoulli–Euler beam theory [15] is a simple model widely used for cantilever beam problem. However, the theory assumed that the beam movement in the X-direction (the direction along the cantilever beam) is negligible. This assumption is valid only when the bending of a cantilever is minor. To build a model feasible to cantilever motion at large-scale, we developed a discrete 2D model to simulate the dynamics of the BMC. Figure 2.5 illustrates this model. The cantilever was simulated with N identical rigid rods connected in series by rotary linkages. Each of the rotary linkages has a torsional spring with spring constant $K_{elastic}$. The first of the rods connects to a fixed wall by one of the rotary linkages, so that a clamp-free cantilever model is built. The coordinate system of the model is an X–Y axis system. Each of the rods has mass m_{rod}, mass moment of inertia I_{rod}, and length l. $K_{elastic}$ is derived from the theoretical reactive-torque of a bimorph cantilever beam under a bending curvature ξ [11]:

$$\tau = \frac{E_1 I_{1c} + E_2 I_{2c}}{\xi} \tag{1.1}$$

I_{1c} and I_{2c} are moments of inertia of the two layers with respect to the centroidal axis of the beam's cross-section: $I_{ic} = I_{i0} + A_i d_i^2$, $I_{i0} = b a_i^3 / 12$, $A_i = b a_i$, $d_1 = \left(E_2 a_2^2 + E_2 a_1 a_2\right) / \left(E_1 a_1 + E_2 a_2\right)$, and $d_2 = \left(E_1 a_1^2 + E_1 a_1 a_2\right) / \left(E_1 a_1 + E_2 a_2\right)$. Since the length of each section of the model is l, from (1) we have

$$K_{elastic} = \frac{\left(E_1 I_{1c} + E_2 I_{2c}\right)}{\ell} \tag{1.2}$$

We generated the dynamics equations of the rods-and linkages model by the Lagrange formula [12,13]. Firstly, the position of the center of each rod $\vec{P}_k$ was given by:

$$\vec{P}_k = \left(\tfrac{\ell}{2}\cos\theta_k + \sum_{i=1}^{k-1}\ell\cos\theta_i\right)\hat{x} + \left(\tfrac{\ell}{2}\sin\theta_k + \sum_{i=1}^{k-1}\ell\sin\theta_i\right)\hat{y} \tag{1.3}$$

where θ_k (k=1,2,…,N) is the elevated angle for each rod. The kinetic co-energy [13] of the rod T_k is

$$\begin{aligned} T_k &= \tfrac{1}{2}m\left|\dot{\vec{P}}\right|^2 + \tfrac{1}{2}I\left(\dot{\theta}_k\right)^2 \\ &= m\ell^2\left[\tfrac{1}{6}\left(\dot{\theta}_k\right)^2 + \sum_{i=1}^{k-1}\tfrac{1}{2}\left(\dot{\theta}_i\right)^2 + \sum_{i=2}^{k-1}\sum_{j=1}^{i-1}\cos\left(\theta_i - \theta_j\right)\dot{\theta}_i\dot{\theta}_j + \sum_{i=1}^{k-1}\tfrac{1}{2}\cos\left(\theta_k - \theta_i\right)\dot{\theta}_k\dot{\theta}_j\right] \end{aligned} \tag{1.4}$$

Eqs. (1.3) and (1.4) lead to the kinetic co-energy of the whole system:

$$T = \sum_{k=1}^{N} T_k = m\ell^2\left[\sum_{i=1}^{N}\left(\tfrac{N-i}{2} + \tfrac{1}{6}\right)\left(\dot{\theta}_i\right)^2 + \sum_{i=2}^{N}\left(N - i + \tfrac{1}{2}\right)\sum_{j=1}^{i-1}\cos\left(\theta_i - \theta_j\right)\dot{\theta}_i\dot{\theta}_j\right] \tag{1.5}$$

The potential energy of the system is

$$V = \sum_{i=2}^{N}\tfrac{1}{2}K_{elastic}\left(\theta_i - \theta_{i-1}\right)^2 \tag{1.6}$$

and the Lagrangian of the system is simply

$$L = T - V \tag{1.7}$$

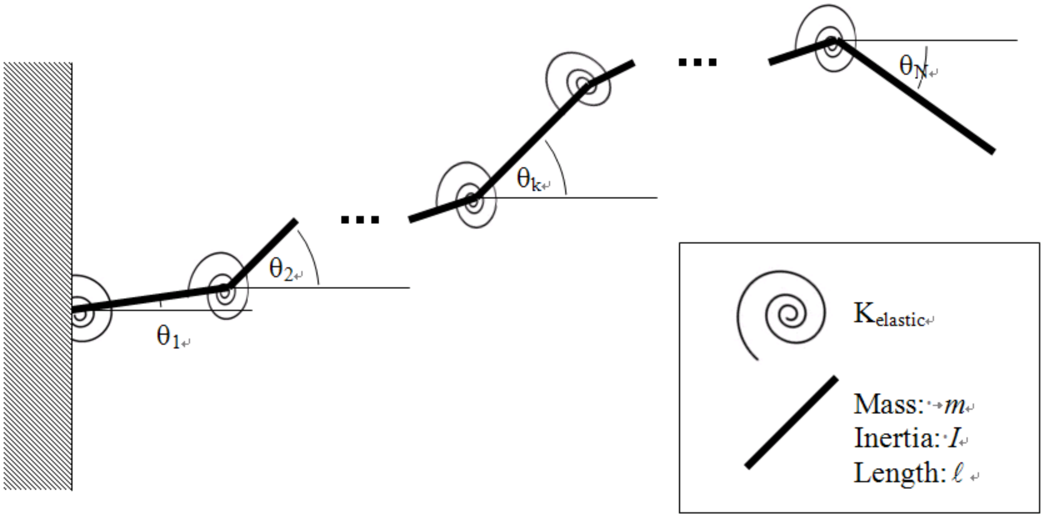

Figure 2.5 The cantilever was simulated with N identical rigid rods connected in series by rotary linkages. Each of the rotary linkages has a torsional spring with spring constant $K_{elastic}$. The first of the rods connects to a fixed wall by one of the rotary linkages, so that a clamp-free cantilever model is built. The motion of the simulated cantilever is characterized by the elevated angles θ_k (k=1, 2,…,N) of each rod.

Table 2.1 Assignment of Variables

Variable	Description	Given Value	Unit
a_1, a_2	Thickness of the first (silicon) and second (gold) layers	1.5 & 0.5	μm
b	BMC width	60	μm
E_1, E_2	Young's modules of materials of the first and second layers	122.4 & 77.2	GPa
α_1, α_2	Thermal expansion coefficients of the materials of the first and second layers	3.2e-6 & 14.5e-6	K^{-1}
L	BMC beam length	500, 850, 1000	μm
ρ_1, ρ_2	Material densities of the first and second layers	2328 &19320	kg/m^3
ρ_a	Air density	1.225	kg/m^3
C_{V1}, C_{V2}	Specific heat of the first and second layers	702.0 &132.3	J/kgK
k_1, k_2	Thermal conductivities of the first and second layers	124.0 &30	W/mK
R	Reflectivity of the top layer surface (gold) against 355 nm laser	0.2	—
D	Laser beam diameter	1.0	mm
t_w	Laser pulse width	12	ns
N	Number of rods in the rods & linkages model	—	—
θ_{equi}	Equilibrium bending angle at temperature *T0*	calculated	rad
θ_k	Elevated angle of the rod *k*	calculated	rad
I_1, I_2	$(I_{1,2} = ba_{1,2}^3/12)$ Area moment of inertias of the cross-section of the first and second layers relative to their own centroidal axis (parallel to the *Z*-axis in our model)	calculated	m^4
I_{1c}, I_{2c}	Area moment of inertias of the cross-section of the first and second layers relative to the centroidal axis (parallel to the *Z*-axis in our model) of the crosssection of the whole beam	calculated	m^4
ΔT	Temperature change from T0	calculated	K
l	$(= L/N)$ Length of each rod in the rods-and-linkages model	calculated	μm
m_{rod}	$(= lb(a_1\rho_1 + a_2\rho_2))$ The mass of each rod in the rods-and-linkages model	calculated	kg
I_{rod}	$(= m_{rod}l^2/12)$ Mass moment of inertias of each rod relative to its centroidal axis (parallel to the *Z*-axis in our model)	calculated	kgm^2

2.3.1. Free Vibration to Check the Validity of the Link and Bar Model

When there is no external force, i.e., bending moments or damping, the dynamics equation for the cantilever system is [12]

$$\frac{d}{dt}\left(\frac{\partial L}{\partial \dot{\theta}_k}\right)-\frac{\partial L}{\partial \theta_k}=0 \tag{1.8}$$

According to (1.8), we derived the dynamics equations in matrix form

$$\begin{bmatrix} A_{1,1} & A_{1,2} & \cdots & A_{1,N} \\ A_{2,1} & A_{2,2} & & \vdots \\ \vdots & & \ddots & \vdots \\ A_{N,1} & \cdots & \cdots & A_{N,N} \end{bmatrix} \cdot \begin{bmatrix} \ddot{\theta}_1 \\ \ddot{\theta}_2 \\ \vdots \\ \ddot{\theta}_N \end{bmatrix} = \begin{bmatrix} B_1 \\ B_2 \\ \vdots \\ B_N \end{bmatrix} \quad \text{or} \quad \tilde{\mathrm{A}}\left(\Theta,\dot{\Theta}\right)\cdot\ddot{\Theta}=\tilde{\mathrm{B}}\left(\Theta,\dot{\Theta}\right) \tag{1.9}$$

where $A_{i,j}=A_{i,j}\left(\theta_1,\theta_2,\ldots\theta_N,\dot{\theta}_1,\dot{\theta}_2,\ldots\dot{\theta}_N\right)$ and $B_i=B_i\left(\theta_1,\theta_2,\ldots\theta_N,\dot{\theta}_1,\dot{\theta}_2,\ldots\dot{\theta}_N\right)$. We used MATLAB® program to solve the linear equation (1.9) and simulate the free vibration of the BMC of 500 μm long. In the simulation, the BMC was initially stationary and was under a uniform bending moment parallel to the Z direction. The bending moment provided each of the elastic linkages an identical bending angle. At t = 0, the bending was released and the system began to experience a free vibration. We studied the simulation results with different linkage numbers (N). Fast Fourier transform (FFT) [14] was used to analyze the time-domain results (Figure 2.6a), such that the natural frequencies of the model were revealed (Figure 2.6b). The time of the simulation was set to be 10.6 μs, which was long enough to achieve a FFT frequency resolution of 100 Hz. We compared the results from the FFT analysis and those from theoretical calculation. According to the

Bernoulli–Euler beam theory [15], a clamped–free bi-layered beam has natural frequencies of

$$f_n = \frac{\lambda_n^2}{2\pi L^2}\sqrt{\frac{E_1 I_1 + E_2 I_2}{A_1\rho_1 + A_2\rho_2}}, \text{ n= 1, 2, 3...} \tag{1.10}$$

where $A_{1,2}$ and $\rho_{1,2}$ are the cross-sectional areas and the densities of the two layers, respectively. L is the length of the beam. Each eigenvalue λ_n satisfies $\cos\lambda_n \cosh\lambda_n = -1$ [15].

In Figure 2.6, we used dotted lines to mark the first four orders of theoretical natural frequencies derived from (1.10). It shows that, as N increases, the number of FFT peaks, which indicate the natural frequencies of the BMC, gradually converge to the theoretical values. To evaluate the accuracy of the model, we converted simulated natural frequencies $f_{n,sim}$ into the squares of simulated eigenvalues $\lambda_{n,sim}^2$:

$$\lambda_{n,sim}^2 = 2\pi L^2 f_{n,sim}\sqrt{\frac{A_1\rho_1 + A_2\rho_2}{E_1 I_1 + E_2 I_2}}, \text{ n= 1, 2, 3, . . .} \tag{1.11}$$

In Figure 2.7, we show the accuracy of $\lambda_{n,sim}^2$ compared to the theoretical λ_n^2. It shows that the precision of the first four λ_n^2 (as ratios $\lambda_{n,sim}^2 / \lambda_n^2$) become larger than 95% when N is over 20. Since f_n is proportional to λ_n and λ_n is non-dimensional, we know that by using the rod- and linkage model, the accuracy of the first four simulated natural frequencies can exceed 95% when the rod number N is over 20.

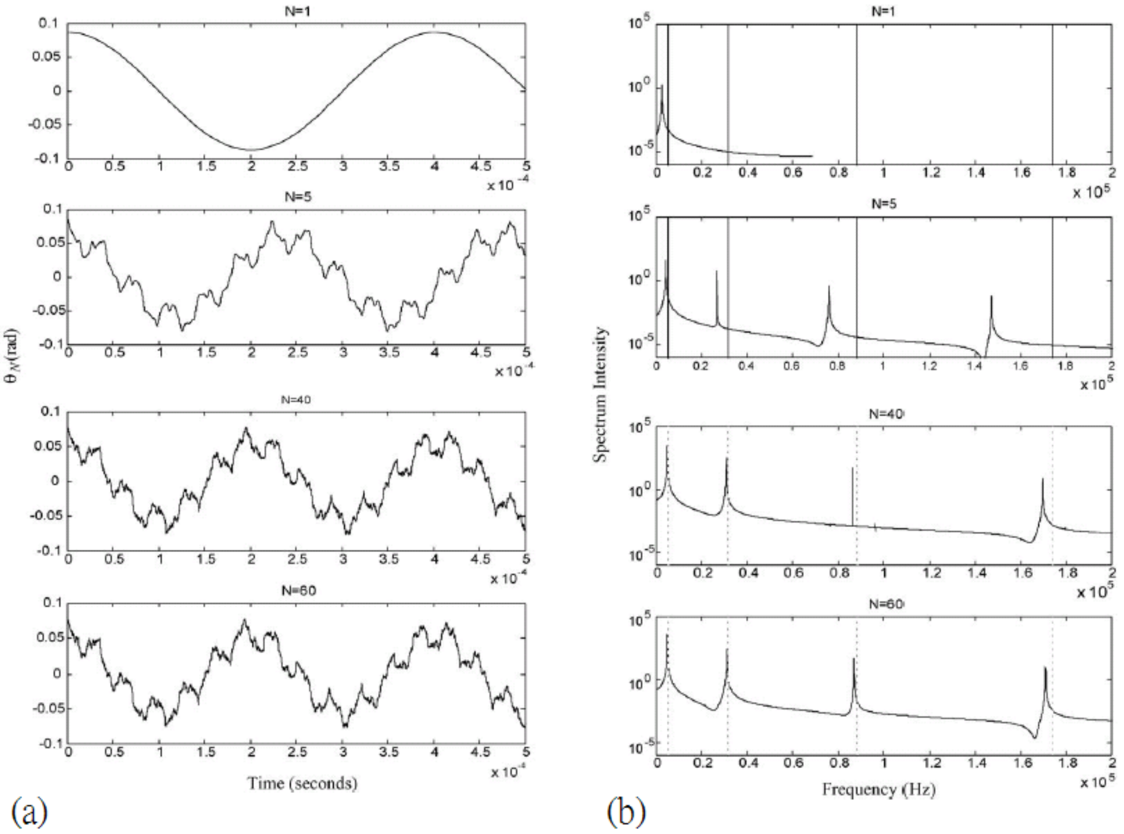

Figure 2.6 (a) The time-domain simulation result with respect to the models having different number of rods (N). The curves show the vibration of θ_N, tilting angle of the last rod that forms the free-end of the cantilever. (b) The FFT frequency spectrum of the simulation results of models having different number of rods (N). The dotted lines indicate the theoretical natural frequencies of the first four orders derived by Bernoulli–Euler beam theory: 5.06, 31.69, 88.73, and 173.88 kHz.

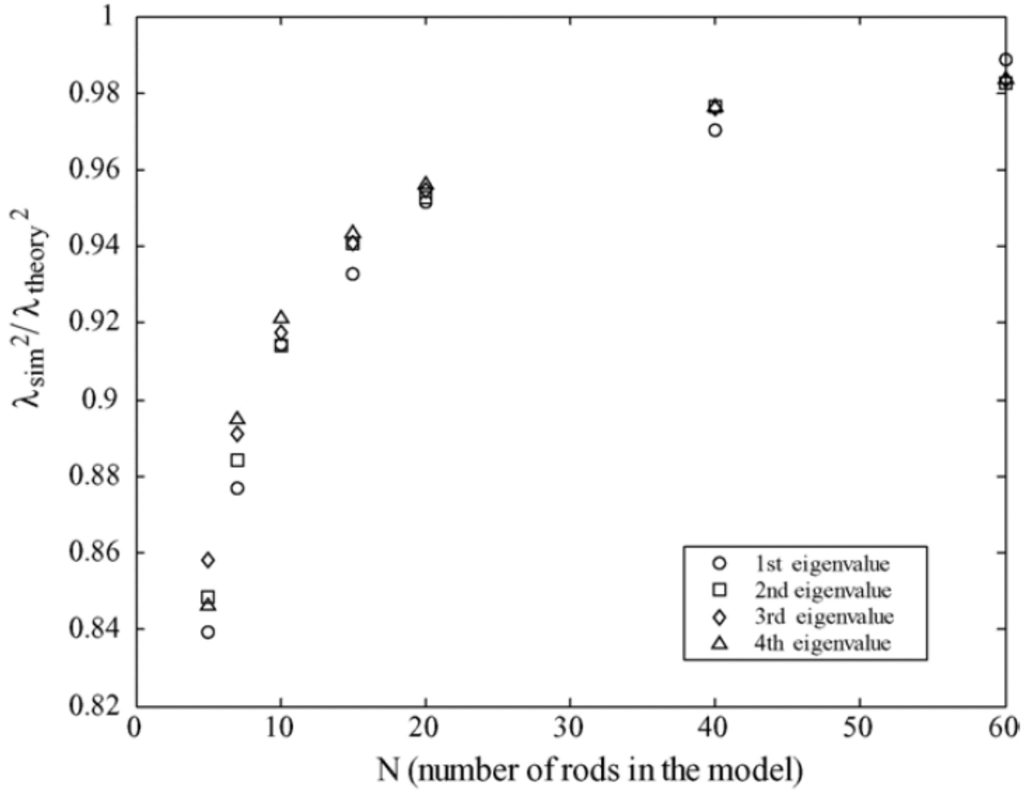

Figure 2.7 This figure shows the values of $\lambda_{n,sim}^2 / \lambda_{n,theory}^2$ with respect to the models having different number of rods (N). These values indicate the precision of the first four simulated natural frequencies with respect to the theoretical values. The symbols distinguish the $\lambda_{n,sim}^2$'s and $\lambda_{n,theory}^2$'s of the first four different vibration orders (circle: first order, square: second order, diamond: third order, and triangle: fourth order).

2.3.2. The effect of thermal bending moment

When there are external forces such as a thermal shock from a pulsed laser, the dynamics equation for the cantilever system becomes [12]

$$\frac{d}{dt}\left(\frac{\partial L}{\partial \dot{\theta}_k}\right)-\frac{\partial L}{\partial \theta_k}=\sum_i \vec{F}_i \frac{\partial(\vec{q}_i)}{\partial(\theta_k)},\ \mathrm{k} = 1, 2, 3\ldots, \mathrm{N} \tag{1.12}$$

where $\vec{F}_i$ represents a non-conservative force [12] and $\vec{q}_i$ is the displacement of the point at which the force is applied. Let us first discuss the effect of thermal bending. Assuming that there is a thin bimorph cantilever, and it was initially straight. When the local temperature in a position at the cantilever is raised by ΔT, the thin bimorph cantilever would be locally bended at that position by a bending curvature ζ [16]:

$$\frac{1}{\zeta}=\frac{\alpha_1-\alpha_2}{(E_1/a_2+E_2/a_1)\left[\dfrac{2(E_1I_1+E_2I_2)}{(a_1+a_2)}+\dfrac{(a_1+a_2)}{2(1/E_1a_1+1/E_2a_2)}\right]}\times\Delta T=C\Delta T \tag{1.13}$$

where C is a constant. The α_1 and α_2 are the thermal expansion coefficients of the two materials. The other variables in (1.13) follow Table 1.

Using Eq. (1.1), it shows that _T actually generates a local thermal bending moment $\tau_{thermal}$ to the cantilever as

$$\tau_{thermal}=(E_1I_{1c}+E_2I_{2c})C\Delta T=K_{thermal}\Delta T \tag{1.14}$$

The constant $K_{thermal}$ represent the thermal bending moment coefficient of the BMC.

We put the thermal bending effect into the model. Firstly, we describe the temperature rise at linkage i by substituting $\tau_{thermal}$ and ΔT in Eq. (1.14) with $\tau_{thermal,i}$ and ΔT_i, respectively. Secondly, we described $\tau_{thermal,i}$ $(= K_{thermal}\Delta T_i)$ as a torque applied at linkage i by substituting $\vec{F}_i$ in Eq. (1.12) with $\tau_{thermal,i}$. Finally, the displacement $\vec{q}_i$ resulted from $\tau_{thermal,i}$ becomes the change at elevated angle from link $(i-1)$ to link i

$$\vec{q}_i = \theta_i - \theta_{i-1} \tag{1.15}$$

and Eq. (1.12) becomes

$$\frac{d}{dt}\left(\frac{\partial L}{\partial \dot{\theta}_k}\right) - \frac{\partial L}{\partial \theta_k} = K_{thermal}\left(\Delta T_{k+1} - \Delta T_k\right) \quad \text{k = 2, 3,…, N-1} \tag{1.16}$$

The right-hand side of Eq. (1.16) becomes $K_{thermal}\left(-\Delta T_N\right)$ when k =N.

2.3.3. The effect of air dragging

In addition to thermal bending moments, we need to consider the non-conservative force provided by air dragging [17], which gradually stops vibrations. Again referring to (1.12), for rod number i, the dragging force $\vec{F}_i$ and the corresponding displacement $\vec{q}_i$ are

$$\vec{F}_i = \frac{1}{2} b\rho_a C_d \left(\dot{\vec{P}}_i \cdot \hat{n}_i\right)^2 \hat{n}_i \cdot l \tag{1.17}$$

and

$$\vec{q}_i = \vec{P}_i \tag{1.18}$$

where $\hat{n}_i$ is the normal vector perpendicular to the rod i, $\vec{P}_i$ and $\dot{\vec{P}}_i$ the central position and velocity of rod i, ρ_a the density of air, and C_d the air dragging coefficient [17]. Since the Reynolds number Re is small for the micro-cantilever beam (<< 2300), the airflow crossing the micro-cantilever is laminar [17]. Therefore $C_d = K_d / \mathrm{Re}_b$, where $\mathrm{Re}_b = \rho_a \left(\dot{\vec{P}}_i \cdot \hat{n}_i\right) b / \mu$, K_d is a geometric constant ranging from 10 to 100 for the BMC in this work [17], and μ the absolute viscosity of air.

We combined the effects of thermal bending moments and air dragging and derived the comprehensive dynamics equations for the rods-and-linkages model. The equations could be represented in a matrix form

$$\begin{bmatrix} A_{1,1} & A_{1,2} & \cdots & A_{1,N} \\ A_{2,1} & A_{2,2} & & \vdots \\ \vdots & & \ddots & \vdots \\ A_{N,1} & \cdots & \cdots & A_{N,N} \end{bmatrix} \cdot \begin{bmatrix} \ddot{\theta}_1 \\ \ddot{\theta}_2 \\ \vdots \\ \ddot{\theta}_N \end{bmatrix} = \begin{bmatrix} B_1 \\ B_2 \\ \vdots \\ B_N \end{bmatrix} + \begin{bmatrix} QT_1 \\ QT_2 \\ \vdots \\ QT_N \end{bmatrix} + \begin{bmatrix} QD_1 \\ QD_2 \\ \vdots \\ QD_N \end{bmatrix} \tag{1.19}$$

where $A_{i,j}$ and B_i are the same as the ones in (1.9). QT_i and QD_i represent the effect of thermal bending moment and air dragging, respectively, and they are both functions of $\{\theta_k\}$ and $\{\dot{\theta}_k\}$.

2.3.4. Heat Transfer Modeling in the BMC

Heat transfer in laser-heated BMC includes several modes: absorption of laser energy by the top layer, heat conduction from the top to the bottom layer, and heat sinking from the BMC to the base of the cantilever. Foe simplicity, we neglected the heat convection by air, which is relatively slow compared to the other modes of heat transfer. The BMC in our experiment is very thin (0.5 μm for the Au layer and 1.5 μm for the poly-Si layer) and highly thermal-conductive. We calculated and found that it takes less than 10 nanoseconds for the temperature at the BMC top to balance with the bottom. Note that the periods of the first four natural vibration modes of our BMC are in hundreds of microseconds, a very long time compared to the top-to-bottom transfer of heat. Therefore, we used a fin-model [18], considering only the heat transfer along the length of BMCs, to approach the problem. In this model, along the length (L) of a BMC, the initial temperature is uniformly T_0. As boundary conditions, the clamped-end of the substrate part is set to be constant at T_0, and the free-end of the BMC is isolated. The transient heat conduction model follows:

$$(a_1\rho_1 C_{V1} + a_2\rho_2 C_{V2})\frac{\partial T(x,t)}{\partial t} = (a_1 k_1 + a_2 k_2)\frac{\partial^2 T(x,t)}{\partial x^2} + (1-R) I_{in}(x,t)\sin(\gamma) \qquad (1.20)$$

where T is the temperature at position x and time t, R the reflectivity of the top surface, γ the laser's incident angle, and I_{in} the flux of laser energy applied to the top surface at position x and time t. The other coefficients in Eq. (1.20) follow Table 1. By using Fourier transform, Eq. (1.20) yields the temperature of the BMC as [14]

$$T(x,t) = T_0 + \sum_{n=1}^{\infty}\left[\int_0^t F_{in,n}(\tau)\sin(\gamma)e^{-\lambda_n^2\alpha^2(t-\tau)}d\tau\right]\times\sin(\lambda_n x) \tag{1.21}$$

where

$\alpha = \sqrt{\dfrac{k_1 a_1 + k_2 a_2}{a_1\rho_1 C_{V1} + a_2\rho_2 C_{V2}}}$,

$F_{in,n}(\tau) = \dfrac{2}{L}\int_0^L \dfrac{I_{in}(x,\tau)}{a_1\rho_1 C_{V1} + a_2\rho_2 C_{V2}}\sin(\lambda_n x)dx$,

and

$\lambda_n = (2n-1)\pi / 2L$.

For example, in the case of the 850 µm BMC heated by one laser pulse (laser energy: 0.057 J/cm2 per pulse; pulse width: 12 ns), the variation of temperature over simulated time is calculated according to Eq. (1.21) and is shown in Figure 2.8.

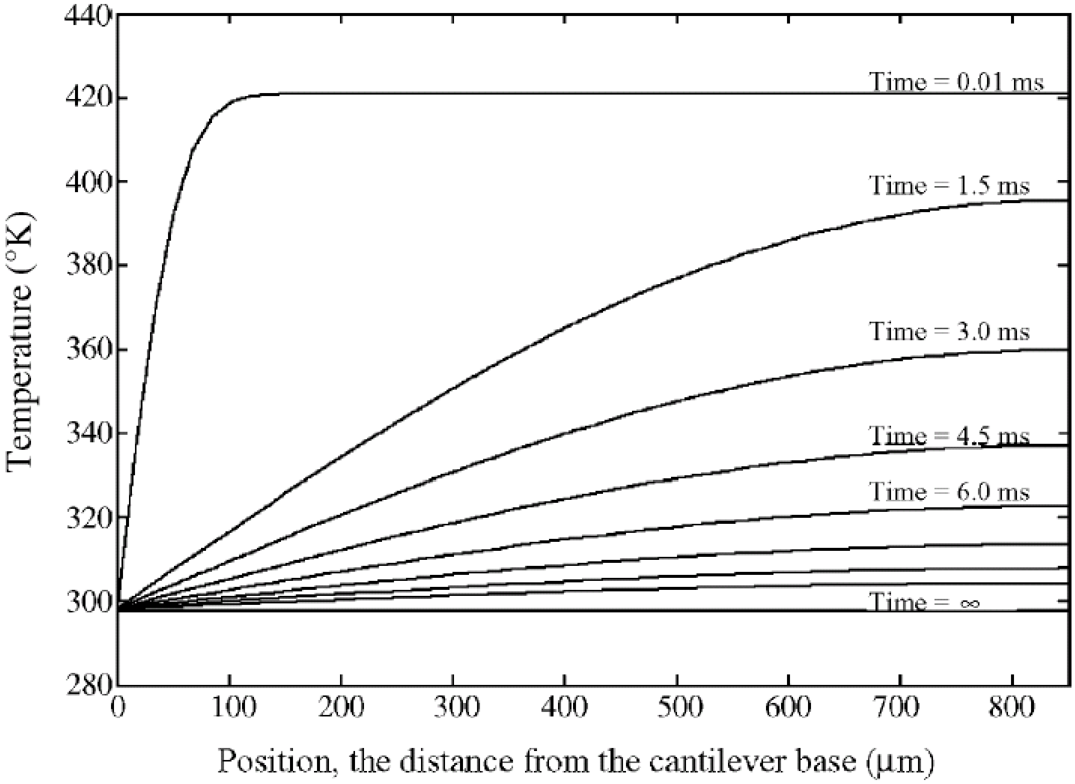

Figure 2.8 The time-variant temperature distribution of an 850 μm BMC heated by a laser pulse (laser energy: 0.057 J/cm2 per pulse; pulse width: 12 ns) is simulated with Eq. (21). Each curve represents the temperature distribution over the length of the BMC, and different curves represent the temperature distribution at a different time after the laser pulse is fired.

2.3.5. Simulation procedure

In our simulation, the initial conditions were: T(x, 0)= 25 ˚C, ˙ $\dot{\theta}_k(0) = 0$, and $\theta_{k+1}(0) - \theta_k(0) = \theta_{equi}\big|_{T=T_{room}} \div N$. $\theta_{equi}\big|_{T=T_{room}}$ is the total bending angle of the BMC caused by the temperature change from its fabrication temperature to room temperature, $T_0 - T_{fab}$.We calculated T_{fab} based on the real BMCs banding angles at 25 ˚C. For the boundary conditions, the temperature at the clamped end of the fin-model remained at T_0 and the thermal conduction at the BMC end of the fin-model was adiabatic, i.e. $T(0,t) = T_0$ and $\partial T(x,t)/\partial x\big|_{x=L} = 0$.

For I_{in}, we assumed that the laser power was uniform over the entire cantilever since the laser beam size (~1 mm wide) was much larger than the BMC. We used a step-function to simulate the laser energy, and the laser energy was non-zero only within the interval from t = 0 to tw (the laser pulse width). In each simulation cycle, we calculated the temperature at the position of each linkage ($x = l, 2\times l, ..., N\times l$) by using Eq. (1.21). These temperatures were applied to Eq. (1.19) to obtain $\theta_k(t)$. According to Figure 2.4, calculated $\theta_k(t)$ were converted into the distance d as follows:

$$d = d_0 + l \cdot \sum_{k=1}^{N} \sin(\beta - \theta_k) \tag{1.22}$$

The geometric coefficients follow those of the BMCs in our experiment. Material characteristic coefficients, as listed in Table 1, were from Ref. [19].

2.4. Results and discussions

2.4.1 Experiment Results vs. Simulation Results in the Time Domain

BMCs with lengths of 1000, 850, and 500 μm, were heated by a single pulse of 355 nm laser of different energies. The BMC response was measured by using the displacement sensor to detect the movement of the BMC tip. During the experiment, we analyzed the signal noises (from electronics, airflow, or mechanical vibrations other than BMC vibrations) and found that the frequencies and amplitudes of the noises did not cover at least the first order (and second order for 1000 and 850μm BMCs, which have lower vibration frequencies) BMC vibration signals.

In Figure 2.9 we show the experimental (solid curves) and simulated (dotted curves) responses of 1000, 850, and 500 μm BMCs heated by a single laser pulse of diameter 1 mm and powers of 84.4, 65.8, and 72.7 μJ/pulse. The vertical axis in each figure 2.2.shows the distance d that we used in Figure 2.4. Note that, an increase in the d means that the BMC is bending away from the DLD sensor and vice versa. The curves in Figure 2.9a–c show the BMCs vibration upon the delivery of laser pulses. In both the experimental and simulated curves, we found that the centers between the local maximum and minimum experience a shifting during the vibration. Beyond a settling time t_{ss}, the shifting vanished. Using our heat transfer model for temperature T(x, t) at section 2.3.4, we found that t_{ss} is about the time for the temperature of the cantilevers to recover to its initial temperature. On the other hand, our experimental result shows that the shifting is substantially proportional to the laser power. We thus believe that these shiftings were resulted from the change of equilibrium bending angles during the heating and cooling processes. Upon heating by a laser pulse, the equilibrium bending angles

θ_{equi} decreased suddenly (with d increased suddenly) when the cantilevers was heated by the laser pulse, and θ_{equi} recovered gradually during the cooling of BMC. In addition to the center-shifting, the maximum displacement of the BMC tip is also substantially proportional to the laser power. Figure 2.10 shows the simulation and experimental results of maximum displacements of the BMCs of 1000, 850, and 500μm long. These results suggest that increasing laser power can significantly enlarge the displacement of the BMCs. The difference between slopes of the experimental and simulated data is likely due to modeling errors from material parameters, like approximation of the BMC surface reflectivity and thermal expansion coefficients of the BMC materials.

Note that damping effect was also considered in our model. We assumed that the damping is generated by air dragging only and is determined by the non-dimensional coefficient K_d, which was expected to be in the range between 10 and 100. In Figure 2.9, K_d was selected to fit the decay tendencies of the experimental results, and the value was found to be about 60, which is within the theoretically expected range. For K_d is theoretically independent to the properties of fluids [17], our model could also predict the response of laser actuation of a BMC placed in liquids.

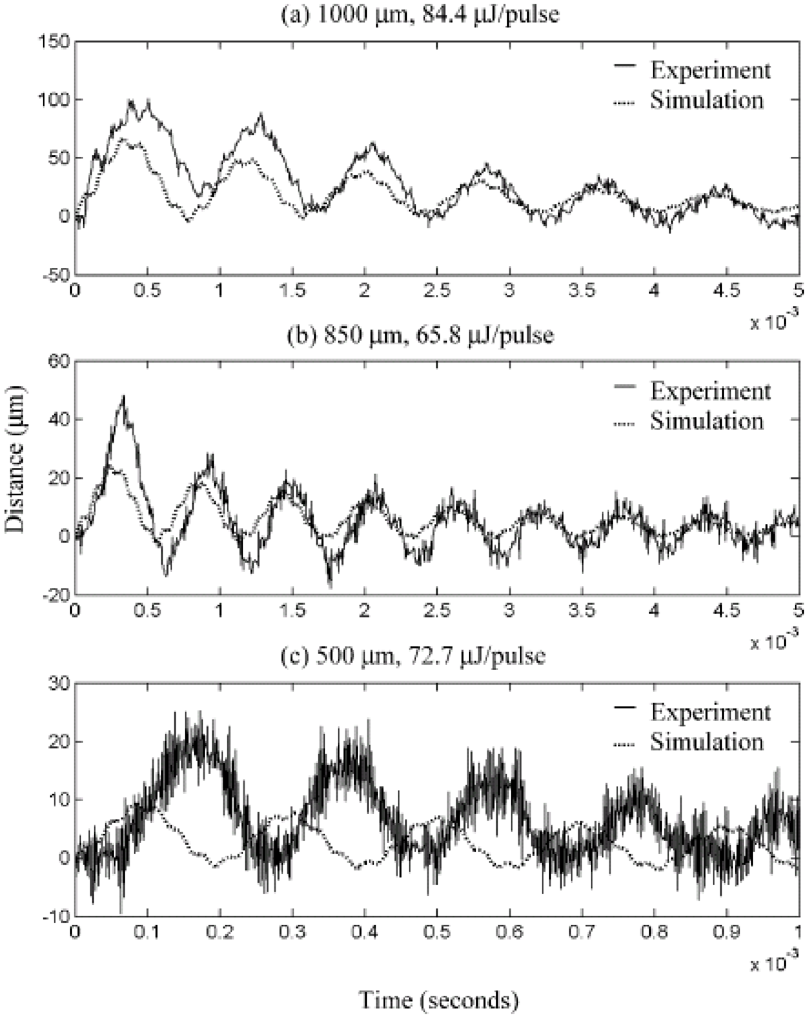

Figure 2.9 The experimental and simulated displacements of the tips on the BMCs shoot by single laser pulses. The BMCs were of different lengths: 1000m (a), 850m (b), and 500m (c). The diameter of the laser beam was fixed to be 1 mm, while the laser powers for each case were different. The parameters in the simulations follow the specific laser energy and BMC length.

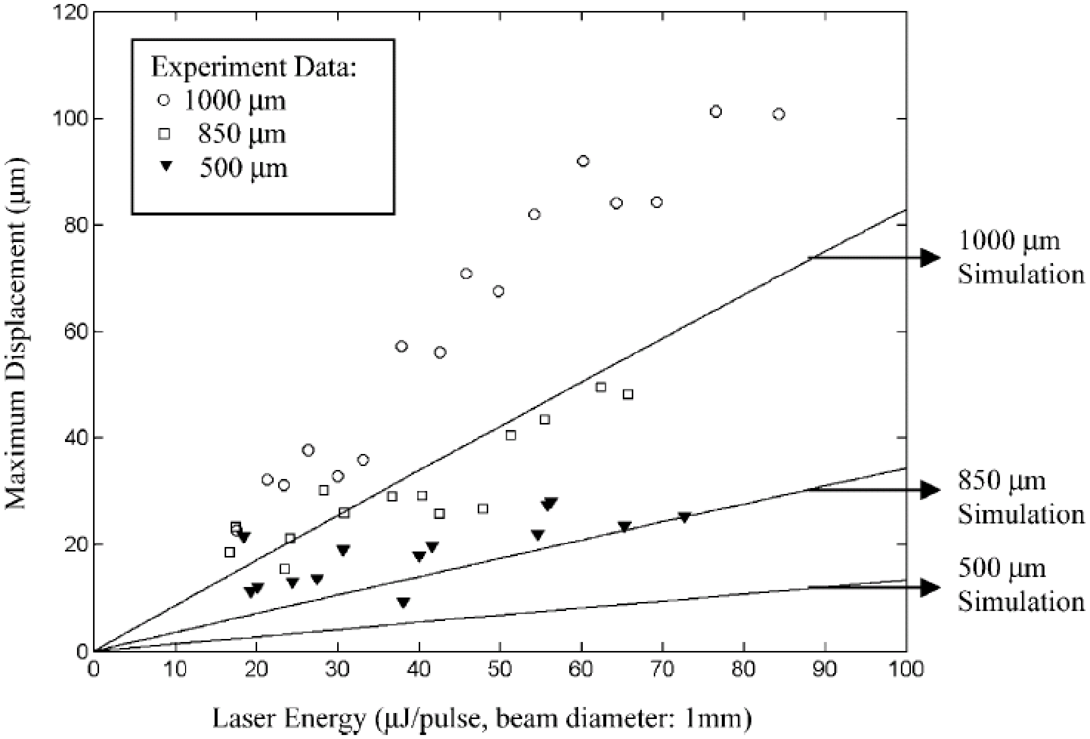

Figure 2.10 The effect of laser power to the maximum displacement of the BMC tips.

2.4.2 Experiment Results vs. Simulation Results in the Frequency Domain

The accuracy of the simulation was further investigated by frequency spectrum analysis as shown in Figure 2.11. The spectrums were derived by using fast Fourier transform [14], and the peaks on the spectrum curves were used to indicate the vibration frequencies of the BMCs. For example, Figure 2.11a shows the experimental spectrum of the 1000 μm BMC. These peaks indicate the first- and second-order vibrations [15] of the 1000 μm beam under pulsed laser heating. Limited by the bandwidth of the displacement sensor (~20 kHz), vibration frequencies higher than 10 kHz were not identified. Similarly, Figure 2.11b and c shows the vibration spectrums for BMCs of the 850 and 500 μm long. It is seen that the simulation results fit very well with the peaks of the experimental spectrums.

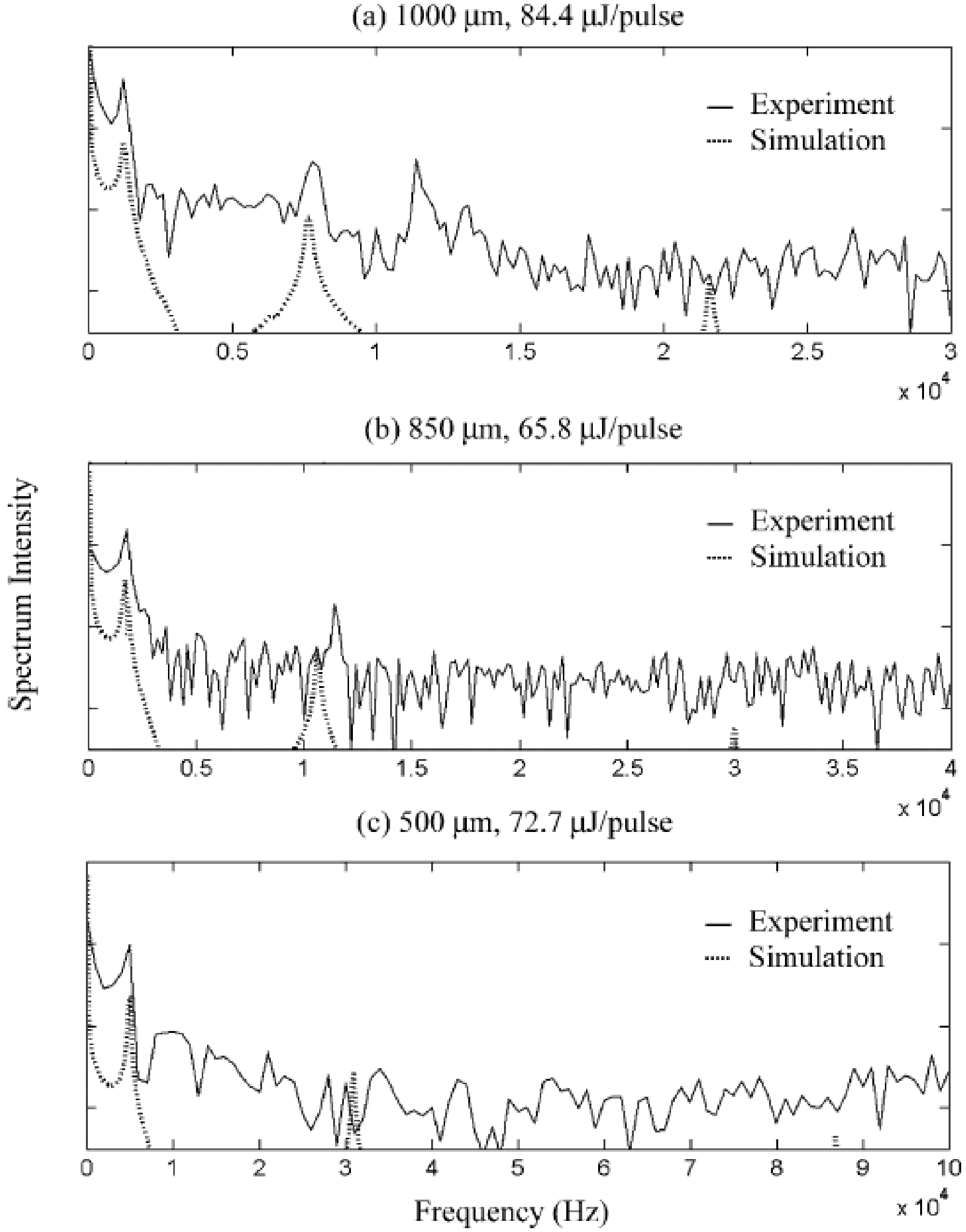

Figure 2.11 Experimental (solid curve) and simulated (dotted curve) frequency spectrums.

2.5. Conclusion

We have demonstrated wireless actuation of a BMC using pulsed laser heating. An experiment was developed to measure BMC vibrations using a displacement sensor. A 2D discrete model was built to simulate the BMC motion under laser heating, where abrupt and large deformations can be accurately simulated. Both the experimental results and numerical simulation revealed that the BMC responded by vibrations at the resonance frequency and significant shifting of the equilibrium position due to heat transfer from the laser to the BMC and finally to the substrate. From experimental data and the simulation results discussed above, we have evidently shown that the pulsed laser can effectively generate large movement in bimorph cantilevers. In the experiment using 1000 μm BMC, with the power of $84.4\ \mu J$ per pulse (laser beam diameter = 1 mm) one could generate a maximum displacement larger than $100\mu m$. This experiment has brought out the information about the feasibility and potential of using pulsed laser heating for wireless MEMS. We believe that this study can contribute to the remote actuation of micro-pumps or micro-propellers.

2.6 Reference

1. A. Camposeo, N. Puccini, F. Fuso, M. Allegrini, E. Arimondo, A. Tuissi, *Laser deposition of shape-memory alloy for MEMS applications*, Appl. Surf. Sci. 208–209 (2003) 518–521.
2. C. Sones, S. Mailis, V. Apostolopoulos, I.E. Barry, C. Gawith, P.G.R. Smith, R.W. Eason, *Fabrication of piezoelectric micro-cantilevers in domain-engineered LiNbO3 single crystals*, J. Micromech. Microeng. 12 (2002) 53–57.
3. S. Zhou, X. Sun, W.N. Carr, *A monolithic variable inductor network using microrelays with combined thermal and electrostatic actuation*, J. Micromech. Microeng. 9 (1999) 45–50.
4. C.A. Savran, A.W. Sparks, J. Sihler, J. Li, W. Wu, D.E. Berlin, T.P. Burg, J. Fritz, M.A. Schmidt, S.R. Manalis, *Fabrication and characterization of a micromechanical sensor for differential detection of nanoscale motions, J. Microelectromech*. Syst. 11 (2002) 703–708.
5. J. Choi, J. Yamaguchi, S. Morales, R. Horowitz, Y. Zhao, A. Majumdar, *Design and control of a thermal stabilizing system for a MEMS optomechanical uncooled infrared imaging camera*, Sens. Actuators A 104 (2003) 132–142.
6. E.A. Wachter, T. Thundat, P.I. Oden, R.J. Warmack, P.G. Datskos, S.L. Sharp, Remote optical detection using microcantilevers, Rev. Sci. Instrum. 67 (1996) 3434–3439.
7. J.M.Z. Ocampo, P.O. Vaccaro, T. Fleischmann, T. Wang, K. Kubota, T. Aida, T. Ohnishi, A. Sugimura, R. Izumoto, M. Hosoda, S. Nashima, *Optical actuation of micromirrors fabricated by the microorigami technique*, Appl. Phys. Lett. 83 (2003) 3647–3649.

8. S. Baglio, S. Castorina, L. Fortuna, N. Savalli, *Modeling and design of novel photo-thermo-mechanical microactuators*, Sens. Actuators A 101 (2002) 185–193.
9. S. Chen, C.P. Grigoropoulos, H.K. Park, P. Kerstens, A.C. Tam, *Photothermal displacement measurement of transient melting and surface deformation during pulsed laser heating*, Appl. Phys. Lett. 73 (1998) 2093–2095.
10. L.G. Shamanaeva, *Thermooptical mechanism of sound generation by high-power laser radiation propagating in the atmosphere*, Russ. Phys. J. 44 (2001) 1187–1196.
11. W.D. Callister, Materials Science and Engineering: An Introduction, Wiley, New York, 2003.
12. H. Goldstein, Classical Mechanics, Addison-Wesley, 1950, p. 347.
13. D. Karnopp, D.L. Margolis, R.C. Rosenberg, System Dynamics—Modeling and Simulation of Mechanical System, Wiley, 2000, p.124.
14. P.V. O’Neil, Advanced Engineering Mathematics, Belmont, 3rd ed., 1991.
15. J.H. Williams Jr., Fundamentals of Applied Dynamics, Wiley, 1996.
16. S. Timoshenko, *Analysis of bi-metallic thermostates*, J. Opt. Soc. Am. 11 (1925) 233.
17. R.W. Fox, A.T. McDonald, Introduction to Fluid Mechanics, Wiley, Canada, 1994, pp. 418–422.
18. F.P. Incropera, D.P. De Witt, Fundamentals of Heat and Mass Transfer, Wiley, New York, 1990.
19. MatWeb, http://www.matweb.com/.

Chapter 3 : Photo Deformable Microshells and Nanoparticles Coating

3.1 Introduction

3.1.1 Photo-Interaction among Close, Small Metallic Spheres

Being an attractive topic for over a century [1-6], the behavior of small particles in light has been generally characterized by their absorption and scattering properties. From microscopic point of view, absorption and scattering by particles are actually associated with energy transfer between photons and electrons. The electrons turn photons into kinetic energy but later discharge the energy in the form of light with shifted wavelength, phase angle, and changed power. When the dimension of a particle is small compared to the wavelength of an incident light, the behaviors of the entire electrons in a particle become interesting. Mie's scattering theory [1] shows that the electrons in a particle much smaller than the wavelength tend to move periodically and coherently. These electrons cause a periodic, coherent charge movement in the small particle and become physically similar to a large electronic dipole moment in the space. Indeed, Mie's theory suggests that light scattering by a single small particle can be approximated by radiation from an electronic dipole-moment, since it is mathematically similar to the dynamics of an electron in a dielectric material.

The optical property of a medium that includes many small particles can be sometimes correctly analyzed using a linear combination of the behaviors from each individual particle. The multi-particle medium is characterized by an effective dielectric constant, which takes into account the approximated dipole moments of the small particles. The bottom line assumption of this dipole approximation is that the particles are far away from each other.

In many real cases, however, the distances among particles are short compared to the wavelength of the incident light. The use of dipole combination becomes invalid to these circumstances. When the distance between two particles is close, the photo energy discharged by neighboring particle becomes as important as a secondary source of incident light, and an absorbed secondary-light may be scattered again and forms a tertiary light source of noticeable power. The multiple scattering phenomenon among close particles has to be considered when modeling a multi-particle system.

The multiple scattering phenomenon among metallic spheres is among the most complicated yet interesting physics problems. The solution to the multiple scattering problem can be very useful for scientific experiments or engineering design related to many fields. The multiple scattering processes among close, small metallic spheres induce particle interactions by surface charge interactions, i.e., surface plasmon coupling, and interparticle-field-enhancement. These interactions, which stem from the motions of free electrons on the surface of metallic particles [1], strongly depend on the spacing among neighboring particles. The particle interactions become significant when the particle spacing is small compared to the wavelength of the incident light [2]. A particulate medium (a medium that comprises small particles) with concentrated particles thus presents very different optical properties from that of diluted particles [1,2]. Recent technology advancement allows ones to use nanometer scale patterns to demonstrate the effects of changing the inter-particle spacing on the absorption of light [2,3]. The effects observed include the shifting and dividing of absorption wavelength, and the increase of absorption at a certain spectrum range. These studies have shed light on the possibility of developing a particulate medium of desirable optical-properties by choosing specific particle and by controlling the inter-particle spacing; these studies also became intuitive to many other studies, including the creation of photo-chemistry reagents, optical communication media, and different passive optical devices [4-6].

3.1.2 Photoisomerization as a Nanoscale Driving Force

Optically induced deformation of polymers containing azobenzene moieties has attracted considerable attention in recent years [7-10]. Through trans-to-cis-state isomerization induced by ultraviolet (UV) light, an azobenzene molecule changes its molecule length (from approximately 9.0 Å to 5.5 Å), space occupation, and polarity [7]; these changes can cause significant effects in the macroscale. The effect from photoisomerization of azobenzene could induce macroscale length reduction [8, 9], enabling AZO-polymers to directly convert photons to mechanical energy and cause observable deformation in a polymer matrix. Important applications of AZO-polymers include photo-bending of AZO-polymeric thin films for micro-devices [8], surface relief gratings (SRG) for maskless micro-groove formation, and SRG surfaces that record the enhancement patterns of surface plasmon [9]. The photo-isomerization effect was also used to produce ellipsoidal sub-micron particles by irradiating spherical azobenzene-micelles with polarized UV-light [10].

3.1.3 Photoisomerization in Combination with Plasmonic Interaction

We created an interesting microactuator by coating gold nanospheres (40 nm) on the surface of a polymeric microshell. The microshell contains “nanomachines” in its shell wall, which is built by polyelectrolytes that contains azobenzene molecules. The microshells shrink upon the irradiation of UV light, and this shrinkage is followed by the changing of the particle spaces among the nanospheres. Figure 3.1 shows an illustration of the microshell. In our previous study [11], we have successfully employed polyelectrolytes that comprise azobenzene molecules to build the photo-deformable microshells using a layer-by-layer (LBL) method [12], which is a self-assembly technique used to construct thin-films of tunable chemical and compositional properties. These microshells present significant contractions under the irradiation of UV light; in our testing, the maximum shrinkage of the microshells’ diameter was about 40%, corresponding to a volume change of 78%. In our testing of the Au microshells, we observed the similar mechanical behavior in response to a UV light source. We instigated the dynamics of electromagnetic interactions among the Au nanospheres by taking absorption spectrum of the geometrically changing microshells. The experiment data was explained by calculations based on a rigorous, multi-sphere Mie theory and also on an approximated simulation.

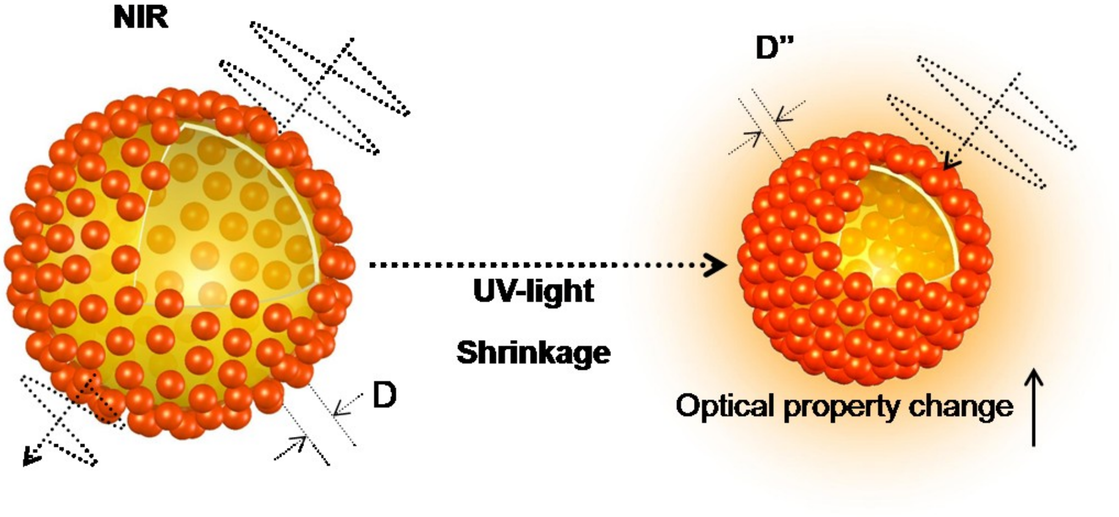

Figure 3.1 A nanospheres-coated microshell tuned by UV light.

3.2 Photo-deformable Microshells with Tunable Optical Properties

3.2.1 Fabrication of Photo-tunable Microshells

The polyelectrolytes, poly (1,4,3 carboxy-4-hydroxyphenylazobenzenesulfonaide-1,-ethanediyl, sodium salt) (PAZO, polyanion, MW 65 000–100 000), poly-allylamine hydrochloride (PAH, polycation, MW = 70 000), and poly (ethyleneimine) (PEI, polycation, MW = 25 000), were purchased from Sigma-Aldrich (St Louis, USA). Silica microspheres (diameter = 5.66μm) were purchased from Bangs' Laboratory (Fishers, USA). Gold nanospheres (40 nm in diameter, negatively charged on the surface by carboxylic groups) were purchased from British Biocell International (UK). All materials were used as received. The polyelectrolyteswere dissolved in deionized (DI) water at 2 mg ml−1. The pH values of PAZO, PAH, and PEI were about 7.0, 7.0, and 9.0, respectively. No other chemicals were added into the solution. The chemical structures of PAZO, PAH, and PEI are shown in Figure 3.2

Figure 3.3 shows the layer-by-layer (LBL) method we used to create the microshells. Silica microspheres were used as templates for the microshell formation. To enhance the surface charge, the microspheres, which are negatively charged by hydroxyl groups (–OH), were pre-coated with PEI. 0.1 ml of SiO2 microspheres (approximately 7 × 108 particles) were mixed into 14 ml of PEI solution. Then, the solution was stirred for 30 min to allow the PEI to coat the microspheres; this was followed by centrifuging and rinsing with DI water. After PEI, to build five LBL layers and form a photo-responsive shell, PAZO and PAH were alternatively coated onto the microspheres five times each through similar procedures. The positively charged microspheres were then mixed into 14 ml of the gold-nanosphere solution (concentration: approximately 1×10^{11} particles per ml). The Au-nanospheres were synthesized using citric acid as surfactant and thus became negatively charged, binding to the last LBL layer, PAH. The solution was gently stirred for 1 h to allow the gold nanospheres to coat onto the microspheres. The solution was then rinsed and centrifuged at 3000 rpm. To deposit concentrated Au nanospheres on the shell surfaces, this coating procedure was repeated five times. The microspheres were then coated with a final layer of PAH to help stabilize the Au nanospheres. Following the coatings, the silica cores of the microspheres were etched away to form microshells by using 1:20 buffered hydrofluoric acid (BHF) for 30 min. The microshells were rinsed seven times to remove the excess BHF and fluoride products. Following all the above procedures except the coating of nanospheres, another group of microshells were made with only the polymeric film. These unmodified microshells were used for the control experiments (3.2.3).

Figure 3.2(b) shows an image of the as-formed microshells under the optical microscope. In an aqueous environment, the microshells (approximately 6.2 μm in diameter) were spherical and swollen. An SEM picture of a dehydrated microshell is shown in figure 3.2(c). In addition, figure 3.2(d) shows an SEM picture of microspheres before the core removal. The bright dots in the picture are the Au nanospheres. According to the SEM pictures, the number of nanospheres covering one microshell is about 14 000. This number was used later for our simulation.

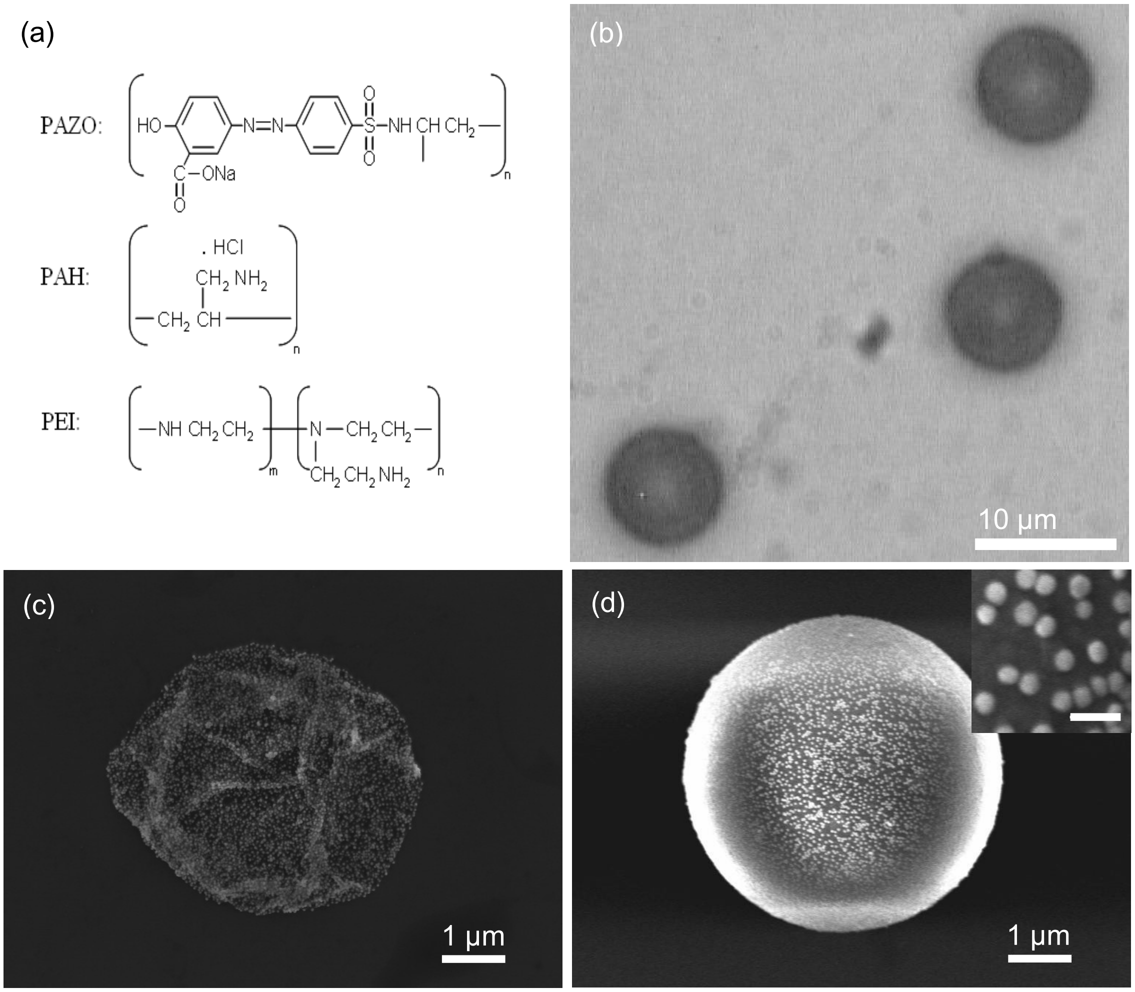

Figure 3.2 The Au-microshells: (a) the structures of the polyelectrolytes for building the microshells; (b) Au-coated microshells suspended in water; (c) an SEM picture of a dehydrated Au- coated microshell; (d) an SEM picture of an Au-coated microshell before the removal of the silica core. The inset in (d) shows the details on the surface; the bar indicates 100 nm.

Figure 3.3

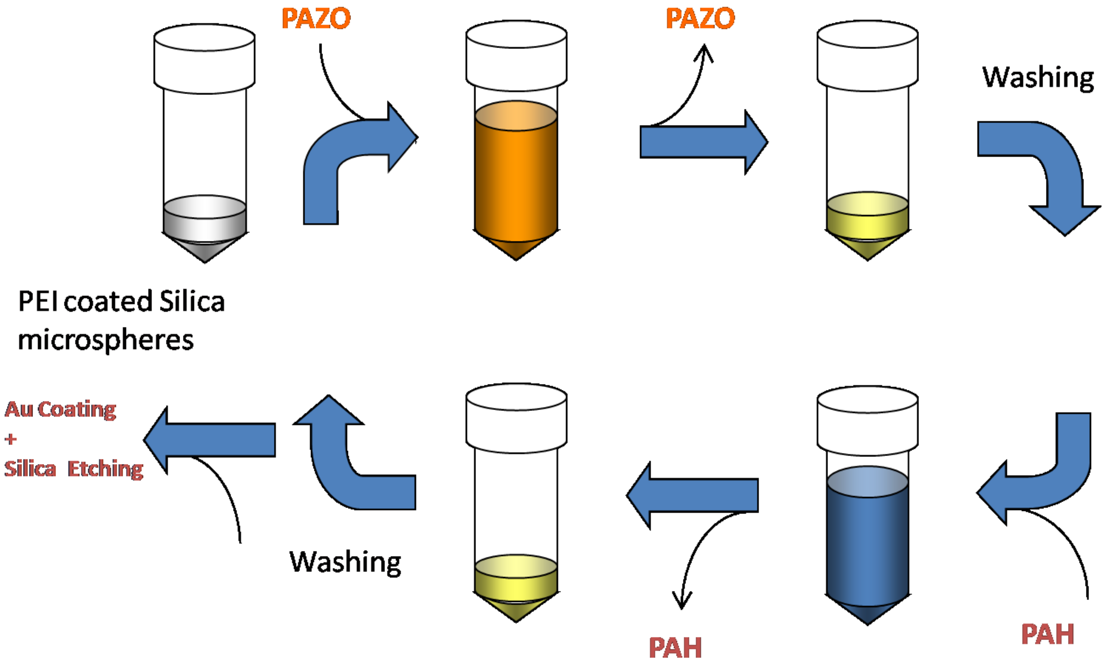

Figure 3.3 To build the microshells, silica microspheres (5.6 µm) was used as templates to coat the photo-responsive polymer. The polymer was coated using the layer-by-layer (LBL) method, in which polyelectrolytes of opposite charges were deposited one after another. After 5 double layers (PAH/PAZO) were coated, the silica cores were removed using BHF, which left the polymer intact.

3.2.2 Testing the Blank-Microshells and Au-Microshells

The microshells, suspended by water, were loaded into a quartz cuvette mounted on a UV–Vis spectroscope (HP 8453) to detect the absorption spectrum. UV light (about 2 Wcm−2 in intensity) from a UV lamp (Green Spot UV Source, 200 W) passed through the sample from the top of the cuvette. The absorption spectra of the microshells were recorded at different irradiation intervals. Sample drops were taken from the cuvette during the UV irradiation and were observed both by an optical microscope (Axiotron, Carl Zeiss, magnification: 50× to 1000×) in an aqueous environment and by a scanning-electrical microscope (SEM, LEO 1530) in a dehydrated state. An integrated CCD camera (CV-S3200CE, JAI Corporation) was used to capture the microscope images. The experiment was carried out at room temperature.

3.2.3 Photo-isomerization at the Uncoated (Blank) Microshells

We tested the photoisomerization effect of azobenzene at the microshells without Au nanospheres. The microshell solution was loaded onto a sample holder. The shape changes of hollow-shells were observed by an optical microscope (Axiotron, Carl Zeiss, magnification: 50× to 1000×). An integrated CCD camera (CV-S3200CE, JAI Corporation) was used to capture the microscope images.

First, we tested the photo-deformation of the blank microshells by using a non-polarized light source. A UV lamp was used to irradiate the microshells. The power of the irradiation at the microshells was about 10 W/cm^2. Under the optical microscope, we observed the blank microshells shrank to about 20% of their original volume within 10 minutes. The shapes of the microshells remained spherical, thus the shrinking of the blank microshells by UV lamp was isotropic.

For a new sample, we switched the light source to a polarized Nd:YAG laser (wavelength = 355 nm, pulse width = 12 ns, pulsing frequency = 10 Hz, energy= 5 mJ/cm^2 per pulse). The polarized light generated a very interesting deformation, which was not found by using the UV lamp.

Figure 3.4(a-c) shows the deformation of the microshells under polarized irradiation. The shape of the microshell gradually changed from spherical to ellipsoidal as the irradiation time elapsed; the long-axes of the ellipsoids were perpendicular to the polarization of the laser beam. To confirm the phenomenon, we changed the polarization of the laser beam for a new sample and found that the long-axes of the deformed microshells changed with the polarization. The testing showed that the microshells experienced anisotropic contraction in the direction parallel to laser polarization. Figure 3.4(a) shows the average changes of long axis, short axis, and the axis-ratio (the ratio of long axis to short-axis) of the microshells as a function of irradiation time. Longer irradiation times induced larger axis-ratios. At the onset of irradiation, the long and short axes contracted approximately equal distances. After 5 minutes, the contract of long axis stopped while the short axis continued to shrink. The axis-ratio of the short axis reached approximately 1.3 after 80 minutes before the shapes of the microshells became steady.

The azobenzene moieties were randomly aligned at the microshells during the LBL fabrication. This asymmetric deformation could be only related to the polarization of light. This result shows a selective absorption of electromagnetic wave by the azobenzene π-bonds; articles elsewhere reported this phenomenon [8(a), 8(d)]. According to those reports, the efficiency f_{iso} to isomerize an azobenzene molecule depends on the intensity of an incident electric field in the direction of the azobenzene π-bond:

$$f_{iso} \propto \left|\vec{E}\right| \cos(\theta) \tag{3.1}$$

where $\left|\vec{E}\right|$ is the intensity of the electric field of the incident light and θ is the angle between $\vec{E}$ and the π-bond. Thus, the π-bond of an azobenzene molecule prefers to absorb an electric wave parallel to the double bond direction, in which $\cos(\theta)$ is maximized. A polarized laser thus selectively isomerizes the azobenzene moieties parallel to the light polarization. Because isomerized azobenzene molecules shrink in the direction of π-bonds, the polarized light also caused the microshells shrinking asymmetrically.

Photo-isomerization of individual azobenzene molecules can be recovered by keeping the sample in darkness (for several days) or upon exposure to visible light [7]. We tested the recoverability of the deformed microshells using laser of a visible wavelength (VIS) (532 nm pulse laser, 10 mJ/ cm^2 per pulse, 10 Hz). The irradiation was maintained for 2 hours. However, the microshells did not present significant geometrical recovery after the VIS irradiation; the size of the deformed microshells remained roughly the same after the test. The stability of the deformed structure might stem from the electrostatic binding among the charge-abundant coating materials.

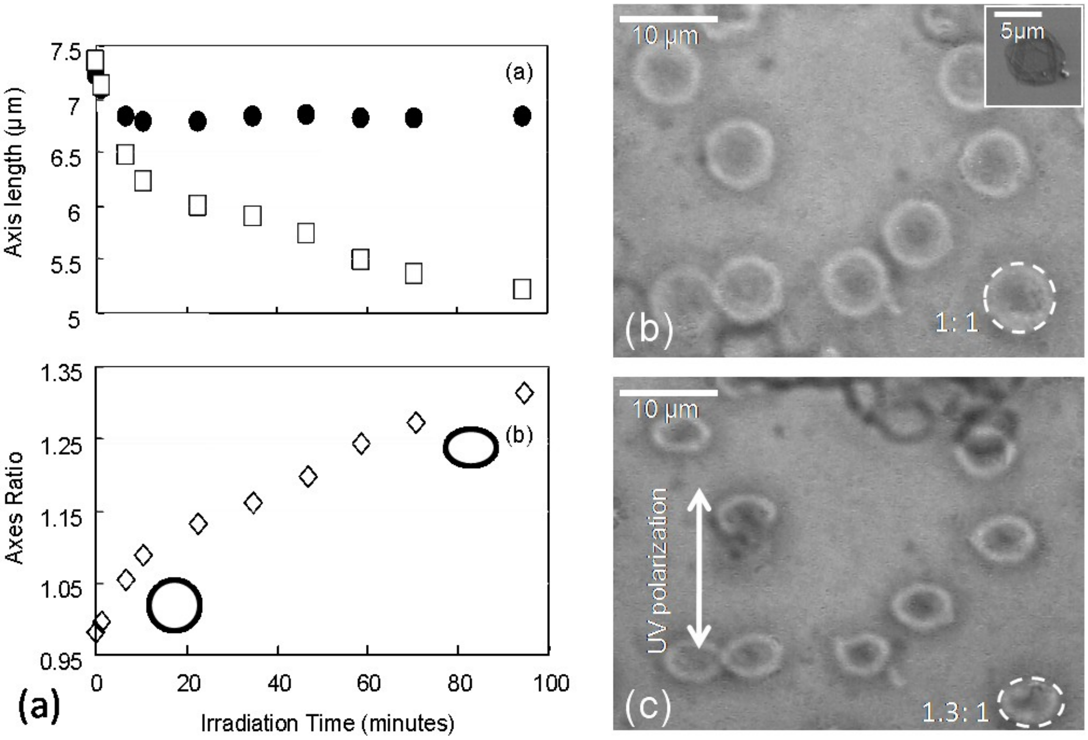

Figure 3.4 Asymmetric deformation of blank microshells under a polarized UV source: (a) the recorded change at the axis ratio of the microshells over the time of exposure; (b) microshells before UV irradiation (the inset shows a dehydrated microshell under SEM); and (c) microshells after irradiation. The contraction of the microshells was parallel to the polarization of incident UV light. This finding shows a selective absorption of electromagnetic (EM) wave by the azobenzene π-bonds, which prefer

3.2.4 Photo-isomerization in the Au coated microshells and Its Optical Effect

We used the same setup to test the photo-deformation of Au-microshells. The Au-microshells at different stages of deformation were characterized by taking UV-Vis absorption spectra. The test was focused on the optical property of the Au coating; the test for asymmetric deformation was not repeated for the Au-microshells.

The experimental results showed that the UV irradiation deforms the Au-coated microshells similar to the control group (the blank microshells). The diameters of Au coated microshell changed from 6.2 μm to about 4.0 μm in 14 min, as shown in figures 3.5 (a) and (b). The diameters of the irradiated polymeric microshells shrank about 40% before becoming stable. Figure 3.5(c) shows the changes of absorption spectra of the Au-coated microshells (concentration: approximately 3×10^6 microshells ml^{-1}).

The spectra of blank microshells (approximately 2×10^7 microshells ml^{-1}) and that of diluted Au nanospheres (approximately 9×10^9 particles ml^{-1}) are also shown in figures 3.5(d) and 3.5 (e). The characteristic absorption of the blank microshells (peak at 370 nm) and the Au nanospheres (peak at 530 nm) were observable in the spectrum of the Au-coated microshells before irradiation.

The UV-induced shrinkage considerably changed the absorption spectrum of the Au-coated microshells. Figure 3.5(c) shows a gradual rise in the near-infrared region (NIR) and also a gradual decay in the region around 560 nm. The peak at 560 nm was from the absorption peak (530 nm) of individual gold nanospheres. We also observed a significant decrease of the absorption in the UV region from 250 to 400 nm. The spectrum of the blank microshells under the same dose of irradiation showed negligible change in the UV and NIR regions (figure 3.5(d)), compared to those of the Au-loaded group.

Interestingly, the spectra show an evolving peak at the enhanced NIR absorption. We observed a drastically enhanced absorption around 970 nm, as marked by an arrow in figure 3.5(c). The location of the 970 nm peak matches the second-overtone band of water in the NIR region [13]. This peak is normally found as a minor absorption peak at the spectrum of regular polymers; we also see this peak at the spectrum of the blank microshells. The 970 nm peaks were weak but observable in the spectra of both Au-microshells and blank microshells before irradiated by UV light. After the UV irradiation, the 970 nm peak in the spectra of Au-microshells was increased by more than tenfold in 14 min, as marked in figure 3.5 (c). The change of this peak was negligible in the blank-microshell spectra.

In the later sections about our simulation models, we will show that this enhanced absorption at 970 nm is an evidence of surface plasmonic enhancement by the gold nanospheres, which create a resonance of elevated, strong electromagnetic filed in the space between adjacent particles by scattering light.

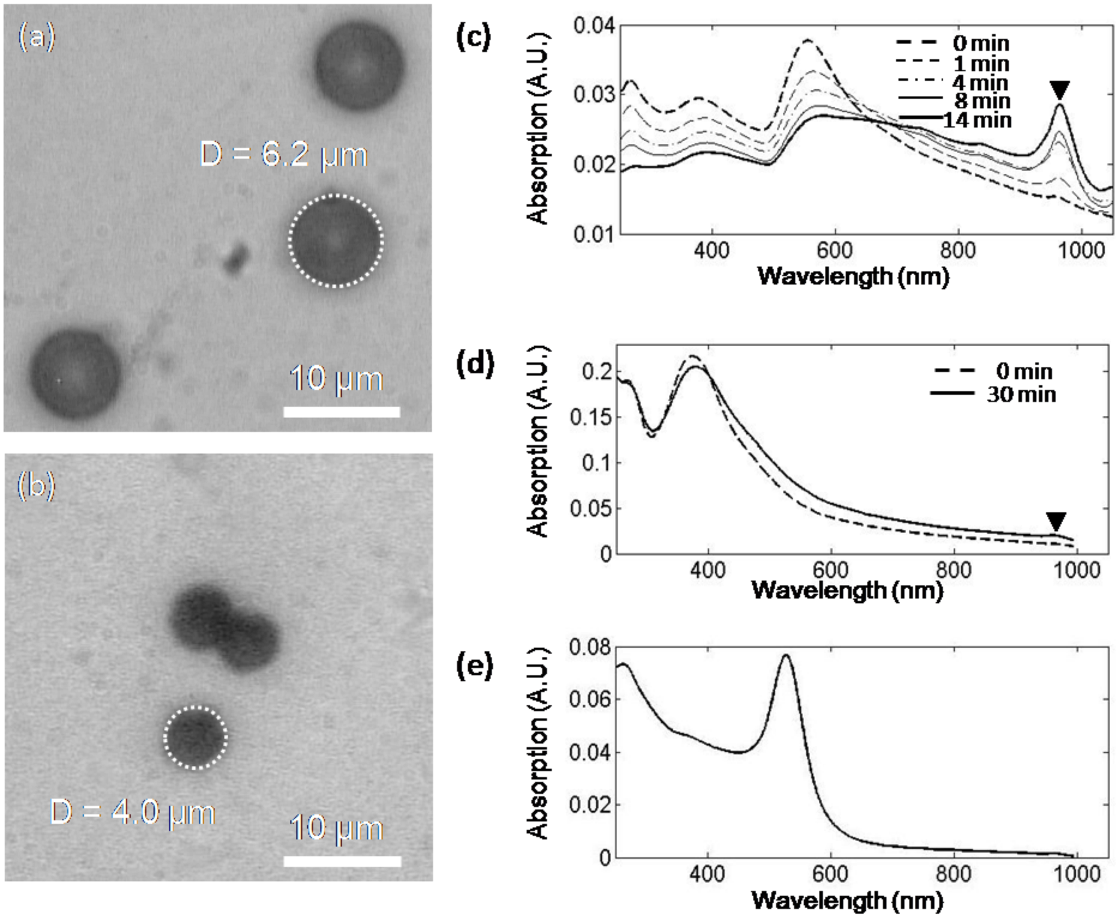

Figure 3.5 Experimental results: (a) the Au-microshells before irradiation; (b) the Au-microshells after irradiation; the shell diameters reduced from 6.2 µm to 4.0 µm; (c) the change in the absorption spectrum of the Au-coated microshells at different intervals of irradiation; (d) the change in the absorption spectrum of the control group (microshells without Au nanospheres); (e) The absorption spectrum of diluted Au nanospheres. The arrow at (c) and (d) mark the peaks observed at 970 nm. This peak at the spectra of UV-irradiate Au-microshell grew drastically upon irradiation.

3.3. Analytical Analysis of Electromagnetic Field Enhancement among Nanospheres with Varying Spacing

We developed two mathematical models to reveal the physics behind the photo-tunable absorption by Au-microshells. Firstly, a modified Mie scattering theory was used to calculate the enhancement of electromagnetic (EM) field between two gold nanospheres. The modified Mie model is a decent tool to exactly calculate the field enhancement effect between close spheres. The simulation result showed that the density of EM-energy in the space between neighboring nano-spheres increases drastically as the inter-particle space decreases. Simulated absorption-spectra also showed a peak-shifting from the visible to the infrared region when decreasing the nanosphere spacing. We used our previous experiment to verify the analytical results.

By using a first-ordered approximation of the modified Mie's Scattering theory, we also built a multi-particles model to simulate the absorption by the entire microshell coated with concentrated Au nanospheres. 14,000 simulated particles were located on a large spherical surface using Monte Carlo method. The shrinking of the microshell was simulated by reducing the diameter of the large sphere. The change of relative positions among the nanospheres at the microshells was simulated using hook's law. The absorption curves at different stage of microshell shrinkage were calculated as our simulation result.

The rigorous Mie's model and also the 1^{st}-ordered approximating model revealed the existence of an important phenomenon in our previous testing of the Au-microshells, which is normally called plasmonic enhancement.

3.3.1 Two-Spheres Model based on Modified Mie Theory

Since the beginning of the 20th century, Mie scattering theory has become a standard model to analyze the enhancement of electromagnetic-wave by small spherical particles [1, 14]. Mie theory calculates exactly the distribution of electromagnetic field around one isolated, homogeneous, spherical object under the irradiation of a plane wave. Before the availability of spectroscope, its solution successfully suggested the existence of multiple electromagnetic resonances in an irradiated sphere, at which the scattering and absorption components of the incident light is maximized at specific wavelengths. In addition to conventional optics, the Mie scattering theory has also brought important insight to many fields. For example, the electromagnetic resonance also induces a resonance of surface-electrons, which may trigger chemical reactions. In the case of metallic spheres for photo-catalysis [15], the Mie theory was generally used to explain the formation of photo-electrons which are responsible for the photochemical effects. For engineering science, Mie scattering theory was also applied to study photonic crystals [16] and photovoltaic devices [17].

For problems involving multiple spheres, the original Mie model could lead to an approximated solution by linearly combine absorption and scattering of individual spheres. The accuracy of the approximation, however, depends on the importance of the multiple scattering among spheres, in which the light scattered by each sphere is transferred around the system and becomes an incident light for other spheres. The intensity of multiple-scattering depends strongly on inter-particle spacing. When the spacing is sufficiently large, the multiple-scattering effect becomes negligible compared to the original incident light, and the scattering and absorption components by the whole system are close to the linear combination of Mie's original solution for each individual sphere. In many real experiments, however, the particles are so concentrated that the multiple-scattering effect must be considered by using a different model, for the linear combination approach becomes invalid. A modified Mie model was proposed decades ago to cover the multiple scattering effects [18]. This modified theory differs from the original one by adding the scattering from each sphere $\vec{E}_s^i$ (which is unknown) to the incident wave. Like the original Mie theory, this model offers an exact solution for a multiple-sphere system, where the size and optical property of individual sphere can be different from one to another. The application of this model was once quite limited due to low computer capacity [18]. In recent years, however, it has become possible to apply this model to a system of thousands of closely packed spheres. Surprisingly, little attention was paid to applying the modified Mie theory to real experiments that involve concentrated spheres. Finite element models (FEM) were widely used to solve such type of problems but offer little scientific insight. In this section, we use the modified Mie scattering theory to simulate the electromagnetic-field enhancement by two gold nano-spheres of varying spacing. We also used the previous experiment to verify the simulation results.

3.3.1a Calculate the Multiple Scatterings by Multiple Spheres

In the modified Mie theory, the electric field in the system $\vec{E}_{Total}$ consists of the incident plane-wave $\vec{E}_0$ and scattering by all particles $\vec{E}_s$, where $\vec{E}_s = \sum_{i=1}^{Ns} \vec{E}_s^i$. For linearization, the incident field $\vec{E}_i$ (typically a plane wave), scattered field $\vec{E}_s$, and internal field $\vec{E}_1^i$ (the field inside a sphere) are expanded into polynomials of orthogonal vectors $\vec{M}_{mn}^{(j)}$ and $\vec{N}_{mn}^{(j)}$:

$$\vec{E}_0 = \sum_{n=1}^{\infty} \sum_{m=-n}^{n} \left[p_{mn} \vec{N}_{mn}^{(1)}(r,\theta,\phi) + q_{mn} \vec{M}_{mn}^{(1)}(r,\theta,\phi) \right] \tag{3.2}$$

$$\vec{E}_s = \sum_{i=1}^{N_s} \sum_{n=1}^{\infty} \sum_{m=-n}^{n} \left[a_{mn}^{i} \vec{N}_{mn}^{(3)}\left(r^i,\theta^i,\phi^i\right) + b_{mn}^{i} \vec{M}_{mn}^{(3)}\left(r^i,\theta^i,\phi^i\right) \right]\Bigg|_{R^i > a^i} \tag{3.3}$$

$$\vec{E}_1^i = \sum_{n=1}^{\infty} \sum_{m=-n}^{n} \left[d_{mn}^{i} \vec{N}_{mn}^{(1)}\left(m^i r^i,\theta^i,\phi^i\right) + c_{mn}^{i} \vec{M}_{mn}^{(1)}\left(m^i r^i,\theta^i,\phi^i\right) \right]\Bigg|_{R^i <= a^i} \tag{3.4}$$

The derivation of these orthogonal vectors was given in reference [18]. Figure 3.6 illustrates the coordinate system for the multiple-sphere problem. The spheres are numbered from 1 to N_s. The orthogonal vectors are calculated from: $\vec{M}_{mn}^{(j)} = \nabla \times \vec{R} u_{mn}^{(j)}$ and $\vec{N}_{mn}^{(j)} = (1/k)\nabla \times M_{mn}^{(j)}$. $\vec{R} = (R,\theta,\phi)$ is a position with respect to the origin of a spherical coordinate system. The r in the equations is a dimensionless radius derived from R, and $r = k \cdot R$, where k is the wave constant of the incident light in the surrounding media. $\left(r^i,\theta^i,\phi^i\right)$ is the relative position with respect to the center of sphere i. $u_{mn}^{(j)}$ is the spherical harmonic function, where $u_{mn}^{(1)} = j_n(r) P_n^m(\cos\theta) e^{im\phi}$ and $u_{mn}^{(3)} = h_n(r) P_n^m(\cos\theta) e^{im\phi}$. P_n^m is a term of associated Legendre polynomial, $j_n(r)$ is the n$^{\text{th}}$ order spherical Bessel function, and $h_n(r)$ is the n$^{\text{th}}$ order spherical Hankel functions. a^i in Equation (3.3) is the radius of sphere i. m^i in Equation (3.4) is the relative dielectric constant of sphere i, $m^i = \sqrt{\varepsilon_s^i / \varepsilon_m}$.

To calculate the distribution of the electromagnetic field, we need to find the expansion coefficients p_{mn}, q_{mn}, c_{mn}^{i}, d_{mn}^{i}, a_{mn}^{i}, and b_{mn}^{i}. First, we need to transfer the origin of Equation (3.2) to the center of each sphere i:

$$\vec{E}_0 = \sum_{n=1}^{\infty} \sum_{m=-n}^{n} \left[p_{mn}^{i} \vec{N}_{mn}^{(1)}\left(r^i,\theta^i,\phi^i\right) + q_{mn}^{i} \vec{M}_{mn}^{(1)}\left(r^i,\theta^i,\phi^i\right) \right] \tag{3.5}$$

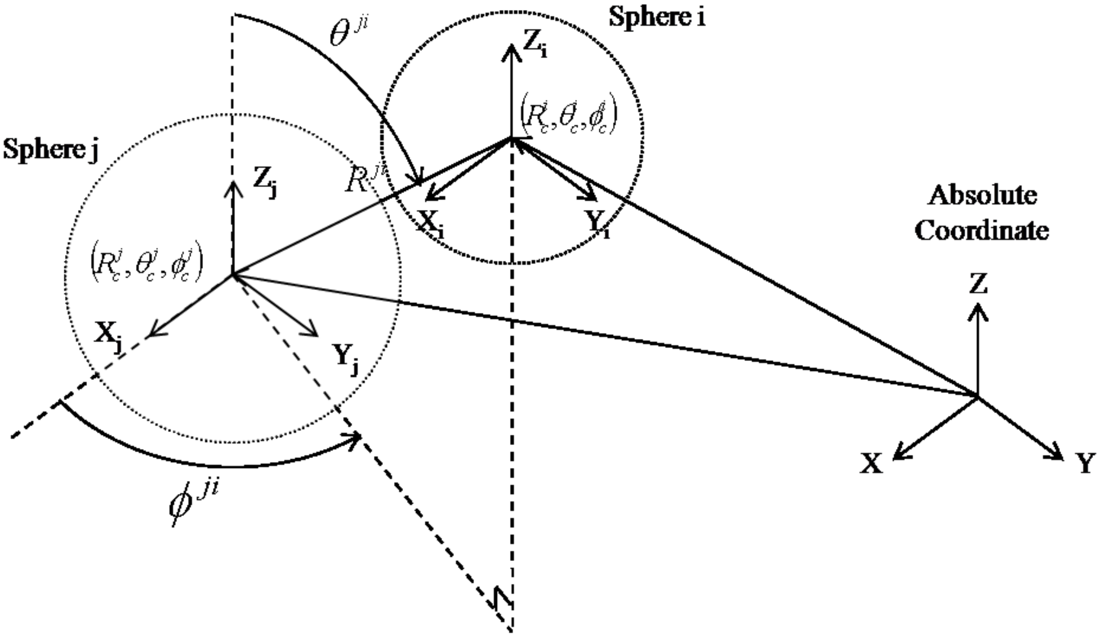

Figure 3.6 A coordinate-system for the multiple-spheres. $(R^{ji}, \theta^{ji}, \phi^{ji})$ denotes the central point of sphere i with respect to the center of sphere j.

For convenience, the direction of the electric field of the incident plane wave $\vec{E}_0$ is set to be parallel to the x-direction of the absolute coordinate system (see Figure 3.6) and the wave vector $\vec{k}$ is parallel to the z-direction. That is, $\vec{E}_0 = \hat{x}E_0 \exp(ikR^0 \cos\theta^0)$. Note that we denoted $\left(R^0, \theta^0, \phi^0\right)$ as the absolute position in the space. With respect to the center of sphere i, $\left(R_c^i, \theta_c^i, \phi_c^i\right)$, the theory gives: $p_{1n}^i = -\frac{1}{2} i^{n+1} E_0 \frac{2n+1}{n(n+1)} \exp(ikR_c^i \cos\theta_c^i)$, $p_{-1n}^i = \frac{1}{2} i^{n+1} E_0 (2n+1) \exp(ikR_c^i \cos\theta_c^i)$, $q_{1n}^i = p_{1n}^i$, $q_{-1n}^i = -p_{-1n}^i$, and $q_{mn}^i = p_{mn}^i = 0$ for $|m| \neq 1$.

To calculate coefficients a_{mn}^i and b_{mn}^i, we use the continuity boundary condition at the surface of each sphere [19]. The tangential components of electric and magnetic fields are continuous across the boundary of the surface of each sphere:

$$\left. \left(\vec{E}_0 + \sum_{i=1}^{N_s} \vec{E}_s^i - \vec{E}_1^i \right) \times \hat{e}_r \right|_{R^i = a^i} = 0 \tag{3.6}$$

$$\left. \left(\vec{H}_0 + \sum_{i=1}^{N_s} \vec{H}_s^i - \vec{H}_1^i \right) \times \hat{e}_r \right|_{R^i = a^i} = 0 \tag{3.7}$$

To solve a_{mn}^i and b_{mn}^i linearly, we need two more equations to relate the expansion vectors of sphere i, $\vec{N}_{mn}^{(1,3)}\left(r^i, \theta^i, \phi^i\right)$ and $\vec{M}_{mn}^{(1,3)}\left(r^i, \theta^i, \phi^i\right)$, to the expansion vectors of a different sphere j, $\vec{N}_{mn}^{(1,3)}\left(r^j, \theta^j, \phi^j\right)$ and $\vec{M}_{mn}^{(1,3)}\left(r^j, \theta^j, \phi^j\right)$:

$$\begin{gathered} \vec{M}_{mn}^{(3)}\left(r^j, \theta^j, \phi^j\right) = \\ \sum_{l=1}^{\infty} \sum_{k=-l}^{l} \left[A_{kl}^{mn}\left(r^{ji}, \theta^{ji}, \phi^{ji}\right) \vec{M}_{kl}^{(1)}\left(r^i, \theta^i, \phi^i\right) + B_{kl}^{mn}\left(r^{ji}, \theta^{ji}, \phi^{ji}\right) \vec{N}_{kl}^{(1)}\left(r^i, \theta^i, \phi^i\right) \right] \end{gathered} \tag{3.8}$$

$$\begin{gathered} \vec{N}_{mn}^{(3)}\left(r^j, \theta^j, \phi^j\right) = \\ \sum_{l=1}^{\infty} \sum_{k=-l}^{l} \left[A_{kl}^{mn}\left(r^{ji}, \theta^{ji}, \phi^{ji}\right) \vec{N}_{kl}^{(1)}\left(r^i, \theta^i, \phi^i\right) + B_{kl}^{mn}\left(r^{ji}, \theta^{ji}, \phi^{ji}\right) \vec{M}_{kl}^{(1)}\left(r^i, \theta^i, \phi^i\right) \right] \end{gathered} \tag{8}$$

$\left(r^{ji},\theta^{ji},\phi^{ji}\right)$ denotes the center of sphere i with respect to the center of sphere j. The calculation of $A_{kl}^{mn}\left(r^{ji},\theta^{ji},\phi^{ji}\right)$ and $B_{kl}^{mn}\left(r^{ji},\theta^{ji},\phi^{ji}\right)$ are given by reference[6]. Combining equations (3.2) to (3.9) we get the linear equations for all a_{mn}^{i} and b_{mn}^{i}:

$$\begin{pmatrix} a_{mn}^{i} \\ b_{mn}^{i} \end{pmatrix} = \begin{pmatrix} -\alpha_{n}^{i} p_{mn}^{i} \\ -\beta_{n}^{i} q_{mn}^{i} \end{pmatrix} + \begin{pmatrix} -\alpha_{n}^{i} A_{mn}^{kl}\left(r^{ji},\theta^{ji},\phi^{ji}\right) & -\alpha_{n}^{i} B_{mn}^{kl}\left(r^{ji},\theta^{ji},\phi^{ji}\right) \\ -\beta_{n}^{i} B_{mn}^{kl}\left(r^{ji},\theta^{ji},\phi^{ji}\right) & -\beta_{n}^{i} A_{mn}^{kl}\left(r^{ji},\theta^{ji},\phi^{ji}\right) \end{pmatrix} \begin{pmatrix} a_{kl}^{j} \\ b_{kl}^{j} \end{pmatrix} \tag{3.10}$$

The coefficients α_{n}^{i} and β_{n}^{i} are given as:

$$\alpha_{n}^{i} = \frac{m^{i}\psi_{n}'(x^{i})\psi_{n}(m^{i}x^{i}) - \psi_{n}(x^{i})\psi_{n}'(m^{i}x^{i})}{m^{i}\xi_{n}'(x^{i})\psi_{n}(m^{i}x^{i}) - \xi_{n}(x^{i})\psi_{n}'(m^{i}x^{i})} \tag{3.11}$$

$$\beta_{n}^{i} = \frac{\psi_{n}'(x^{i})\psi_{n}(m^{i}x^{i}) - m^{i}\psi_{n}(x^{i})\psi_{n}'(m^{i}x^{i})}{\xi_{n}'(x^{i})\psi_{n}(m^{i}x^{i}) - m^{i}\xi_{n}(x^{i})\psi_{n}'(m^{i}x^{i})} \tag{3.12}$$

where $x^{i} = ka^{i}$, $\psi_{n}(\rho) = \rho j_{n}(\rho)$, and $\xi_{n}(\rho) = \rho h_{n}(\rho)$. The primes in (3.11) and (3.12) denote the differentiations with respect to arguments.

The expansion coefficients for the internal field of sphere, c_{mn}^{i}, and d_{mn}^{i}, are calculated by using the boundary conditions (3.6) and (3.7). We get:

$$c_{mn}^{i} = \frac{\mathrm{i}m^{i}}{\psi_{n}'(x^{i})\psi_{n}(m^{i}x^{i}) - m^{i}\psi_{n}(x^{i})\psi_{n}'(m^{i}x^{i})} b_{mn}^{i} \tag{3.13}$$

$$d_{mn}^{i} = \frac{\mathrm{i}m^{i}}{m^{i}\psi_{n}'(x^{i})\psi_{n}(m^{i}x^{i}) - \psi_{n}(x^{i})\psi_{n}'(m^{i}x^{i})} a_{mn}^{i} \tag{3.14}$$

Important properties of the multiple-sphere system are calculated by using the expansion coefficients. For example, the energy absorption (unit: Watt) by sphere i is:

$$W_{abs}^{i} = \frac{1}{2}\mathrm{Re}\left\{ \oint_{A(r^i = x^i)} \left(\vec{E}_1^i \times \vec{H}_1^i\right)\cdot(-\hat{e}_r) \right\}$$

$$= \frac{2\pi E_0{}^2}{\left|m^i\right|^2 \omega} \sum_{n=1}^{\infty} \sum_{m=-n}^{n} \frac{n(n+1)(n+m)!}{(2n+1)(n-m)!} \mathrm{Re}\left\{ \frac{\mathrm{i}}{k\mu} \psi_n'(m^i x^i) \psi_n^*(m^i x^i) \left(m^{i*}\left|d_{mn}\right|^2 + m^i \left|c_{mn}\right|^2\right) \right\}$$

(3.15)

where * denotes a complex conjugate. Similarly, the energy extinction (the separated energy from the original, incident flow of light) by sphere i is:

$$W_{ext}^{i} = \frac{1}{2}\mathrm{Re}\left\{ \oint_{A(r^i = x^i)} \left(\vec{E}_0^i \times \vec{H}_s^i + \vec{E}_s^i \times \vec{H}_0^i\right)\cdot(-\hat{e}_r) \right\}$$

$$= \frac{2\pi E_0{}^2}{\omega} \sum_{n=1}^{\infty} \sum_{m=-n}^{n} \frac{n(n+1)(n+m)!}{(2n+1)(n-m)!} \mathrm{Re}\left\{ \frac{\mathrm{i}}{k\mu} \left(a_{mn}^i p_{mn}^{i*} + b_{mn}^i q_{mn}^{i*}\right)\left(\psi_n^*(x^i)\xi_n'(x^i) - \psi_n'^*(x^i)\xi_n(x^i)\right) \right\}$$

(3.16)

The energy scattered by sphere i is simply the difference between W_{abs}^i and W_{ext}^i:

$$W_{sca}^i = W_{ext}^i - W_{abs}^i \tag{3.17}$$

The energy flux I_i (unit: Watt/m^2) of the incident wave equals $(E_0^2 / 2\omega)\cdot \mathrm{Re}\{k/\mu\}$. Three constantly-used properties[7]: the absorption, extinction, and scattering cross-sections (unit: m^2), are given by: $C_{abs}^i = W_{abs}^i / I_i$, $C_{ext}^i = W_{ext}^i / I_i$, $C_{sca}^i = W_{sca}^i / I_i$.

The number n for a_{mn}^i and b_{mn}^i expands from 1 to infinity. Technically, the solution for (3.2) to (3.4) will be sufficiently precise at a certain order N ($n = 1,2,\ldots N$). In general, a larger N is needed to solve a problem of closer spheres [20].

3.3.1b Modeling the Interaction between Two Gold Nanospheres upon Irradiation

We study the multiple-scattering effect between two gold nanospheres by using the modified Mie theory. We used two kinds of medium dielectric constant ε_m to study the enhancement of electromagnetic field outside the spheres. Reference [21] was used for the dielectric constant ε_m of water, and $\varepsilon_m = 1$ was used for vacuum. The diameter of each gold sphere is 40 nm. The dielectric constant of the bulk-material of gold, $\varepsilon_{s,bulk}$, is from reference [22]. Because the size of 40 nm gold sphere is comparable to the mean-free-path of electrons in gold bulk-material [23], modification terms are needed to cover the damping effect from the confinement of electrons by the particle surface [24]:

$$\varepsilon_s = \varepsilon_{s,bulk} + \frac{\omega_p^2}{\omega^2 + i\gamma_{bulk}\omega} - \frac{\omega_p^2}{\omega^2 + i\gamma\omega} \tag{3.20}$$

where $\gamma = \gamma_{bulk} + Av_f / a$. a is the sphere radius. A is a constant normally assigned 1. For gold bulk-material, the damping constant γ_{bulk} is $1.1 \times 10^{14} Hz$, the plasma frequency ω_p is $1.37 \times 10^{16} Hz$ [25], and the Fermi velocity v_f equals $1.39 \times 10^6 \, m/s$ [26].

The order N of the linear equation was carefully selected to make sure that the error of the calculated absorption by the spheres is less than 1%.

The spheres are both positioned at the X-axis and are aligned parallel to the incident electric field. Different interparticle spaces were used in our simulation: 10 nm, 5 nm, 1 nm and 0.1 nm. Figure 3.7 shows the field enhancement at the X-Y plane of our bi-spherical system irradiated by 700 nm light in vacuum environment. The energy density I (W/m^3) was calculated according to: $I = \frac{1}{4}\left(\vec{E} \cdot \vec{D} + \vec{B} \cdot \vec{H}\right)$ [19]. The plot illustrates the intensity ratio of the enhanced field to the incident light. The result shows that the field-intensity at the mass-center of the two spheres grows sharply and non-linearly as the spheres become closer. In the case of 0.1 nm spacing, as shown by Figure 3.7(d), the intensity increases more than 10^5 fold compared to the incident plane wave.

Figure 3.8 shows the spectrum of absorption cross-section of the bi-spherical system (in vacuum) of different inter-particle spaces. For comparison, the same figure also shows the spectrum of an isolated sphere. When the inter-particle space is large (10 nm and beyond), the spectrum is very close to double that of the isolated-particle spectrum, because there is no significant coupling between the scatterings of the two spheres. As the spheres become closer to each other, the multiple-scattering effect raises the total absorption. Note that the absorption peak of the bi-spherical system undergoes a major red-shift as the spheres approach each other. This red-shifting shows the interaction between the two spheres through their scattering field. A simple model to explain the forming of this spectrum-shifting by a nanoparticle pair is given in ref. 15. In brief, when two particles are aligned parallel to the incident electric filed, the electric dipoles formed at each sphere interacts and delays the response to the incident field. The delay causes the red-shifting at the system's resonance frequency.

Figure 3.9 shows the simulation result from using the same bi-spherical system but in a water medium. The results show a strong enhancement of absorption by water in the gap between the two spheres. Figure 3.9(a) and (b) show the absorption spectrum of water (W/m^3) at the center of the gap. Figure 3.9(b) is the logarithmic plot of (a). The water absorption is increased over 1000 fold when the inter-particle spacing changes from 10 nm to 0.1 nm. The enhancement of the finger-print absorption-peak for water at 970 nm is clearly seen in the simulation result. The trapping of high-density photo-energy in the space between close spheres, as shown in figure 3.7(d), explains the enhanced water absorption. These simulation results were consistent with that of the experiment using Au nanoparticle-coated, photo-deformable microshells.

Note that effect of quantum confinement may become important when the inter-particle spacing is very small. For simplicity, we only focus on using the modified Mie's theory to show the trend of surface plasmon enhancement in a classical way. In a real case, however, the inter-particle spacing may become no smaller than 1 nm due to the space taken by surface ligands (citric acid) on the Au nanoparticles.

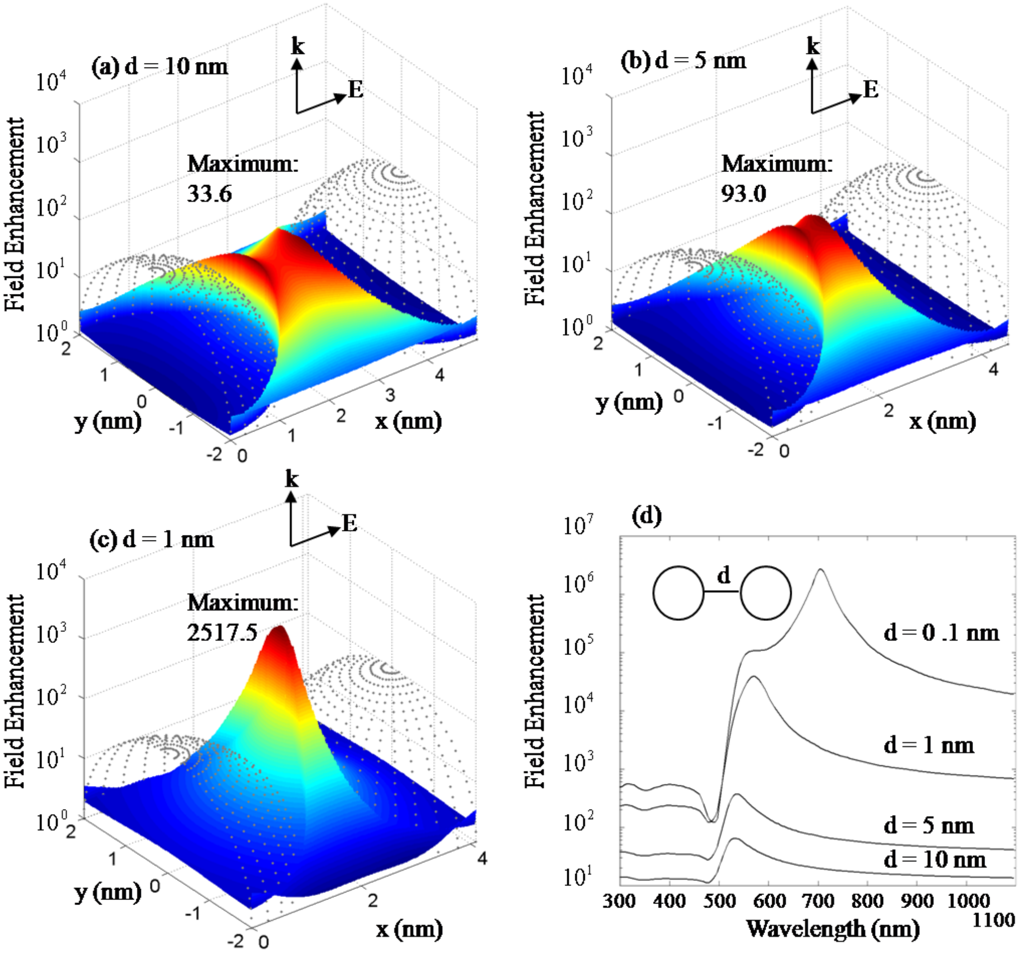

Figure 3.7 Simulated enhancement of energy density between two close spheres in vacuum. Figures (a) to (c) illustrate the intensity ratio of the enhanced field to the incident light; the wavelength is 700 nm in these plots and the inter-particle spaces in the plots are (a) 10nm, (b) 5nm, and (c) 1nm. Figures (d) shows the spectra of field enhancement at the center of different gaps, from 10 nm to 0.1 nm.

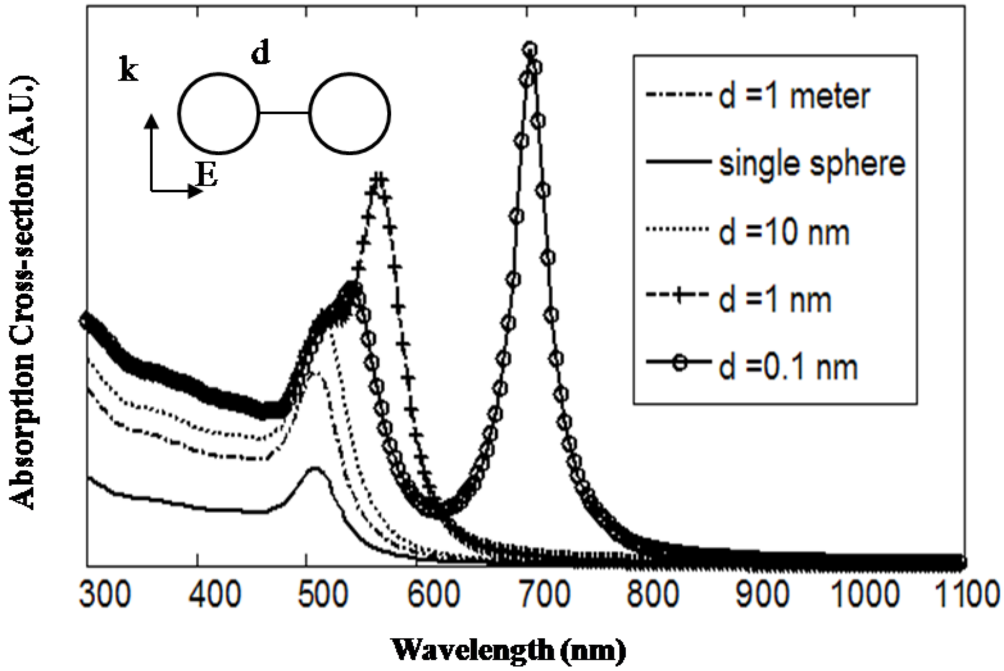

Figure 3.8 The simulated absorption spectra of the bi-spherical system of different gaps. The medium is vacuum. The absorption spectrum of single particle is included for comparison.

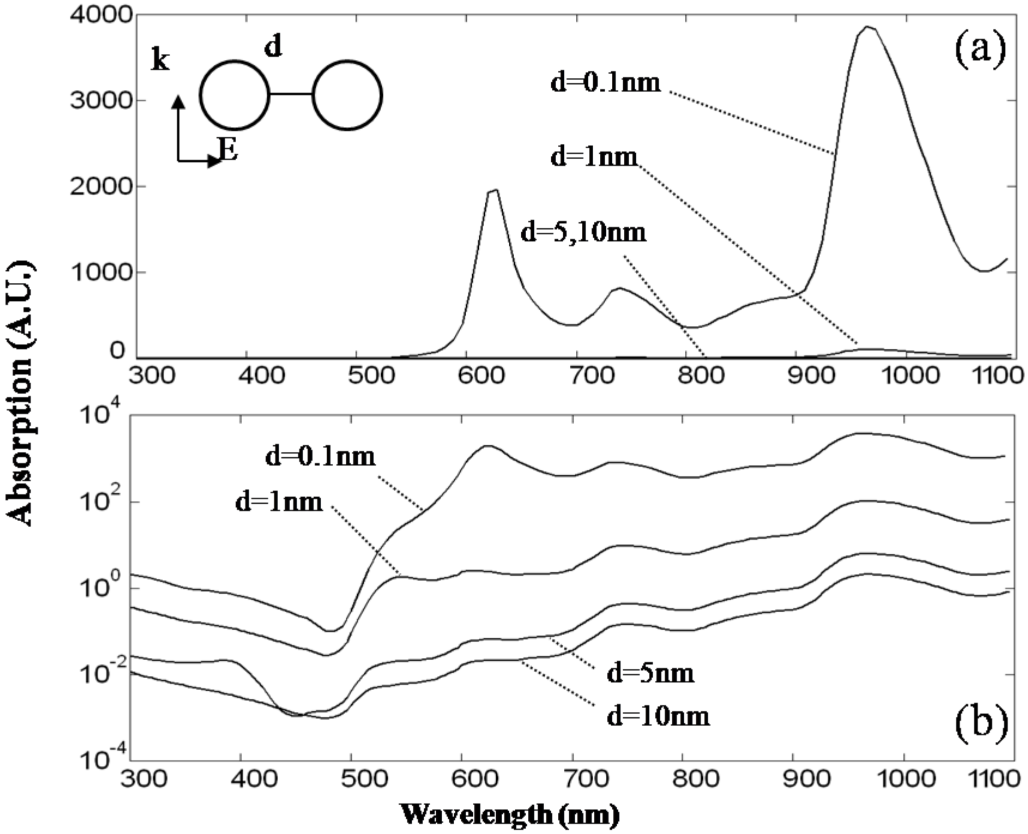

Figure 3.9 (a) The simulated spectra of water absorption at the center of different particle gaps. Note the rising peak at 970 nm, which indicates the enhancement of water absorption. This change was observed in our experiment. (b) A logarithmic plot of (a).

3.3.2 Modleing the entire Microshell Coated with Au Nanospheres

To study the mechanism behind the absorption change of the entire Au microshells, we developed a multi-sphere model to simulate the interaction among the surface nanospheres. Our model is based on a first approximation of the modified Mie's scattering theory in section 3.3.1, which is also called multi-pole approximation of dipole radiation [14, 27, 28].

3.3.2a Dipole Approximation to Solve a Multi-sphere System

Figure 3.10 illustrates our model that includes a monolayer of N nanospheres (of radius a and permittivity ε) on a large sphere of changing radius R. The initial positions of nanospheres $\vec{r}_{m0}$ ($m = 1,2,...N$) were randomly generated on the large sphere using Monte Carlo method. Each nanosphere generates a dipole moment $\vec{p}_m$ ($m = 1,2,...N$) under the influence of an oscillating electric field $\vec{E}_{inc}$ (If a sphere is sufficiently small compared to the wavelength λ of an incident light, its photo-reaction can be approximated with a dipole) [14]. The $\vec{E}_{inc}$ is polarized in the z-direction and vibrates with an angular frequency ω. The medium surrounding the dipoles has a permittivity of ε_m. We also simulated the re-distribution and aggregation of the nanospheres during the shrinkage of the microshell. As the radius of the large sphere changes to R from an initial value of R_0, the position of a nanosphere changes to $\vec{r}_m$ from the initial value of $\vec{r}_{m0}$. The value of $\vec{r}_m$ is numerically calculated based on Hook's Law. In the model, it is assumed that the medium holds the nanospheres with a spring constant k_m, the nanospheres in-touch repel each other with a spring constant k_s, and that $k_s >> k_m$. The dipoles in the model are given by [14]:

$$\vec{p} = 4\pi\varepsilon_m a^3 \frac{\varepsilon_s - \varepsilon_m}{\varepsilon_s + 2\varepsilon_m} \vec{E}_{inc} \tag{3.21}$$

This approximated dipole has resonant modes with respect to the incident wavelength [27]. Absorption peaks are normally observed at these resonant modes and become the typical differences between the absorption spectrum of a small sphere and the spectrum of its parent bulk-material. A comparison between the absorption of Au nanoparticles and an Au thin film has been studied [27b].

The approximated dipoles of different spheres also interact with each other. In the near zone ($|\vec{r}| << \lambda$), the electric field generated by a dipole at the origin point to a position $\vec{r}$ is given by [28]:

$$\vec{E}(\vec{r}) = \frac{3(\vec{p} \cdot \hat{r})\hat{r} - \vec{p}}{4\pi\varepsilon_m |\vec{r}|^3}, \quad \hat{r} = \vec{r}/|\vec{r}| \tag{3.22}$$

When two spheres are very close, $\vec{E}_{inc}$ in equation (3.21) is dominated by $\vec{E}(\vec{r})$ from the neighboring sphere; the approximate dipole of one sphere affects that of its neighbor and vice versa.

The photo-reaction of the nanospheres is calculated with different sets of $\vec{r}_m$ with respect to different values of R. According to equation (3.22), a dipole $\vec{p}_m$ affects the center of the sphere n by an electric field $\vec{E}_{mn}$:

$$\vec{E}_{mn} = \frac{3(\vec{p}_m \cdot \hat{r}_{mn})\hat{r}_{mn} - \vec{p}_m}{4\pi\varepsilon_m r_{mn}{}^3}, \quad r_{mn} = |\vec{r}_n - \vec{r}_m| \tag{3.23}$$

The nanospheres have finite sizes; to consider the average effect of $\vec{p}_m$ on the sphere n, we replace $r_{mn}{}^{-3}$ with an average value $\overline{r_{mn}}{}^{-3}$, where

$$\bar{r}_{mn}{}^{-3} = \frac{1}{2a}\int_{r_{mn}-a}^{r_{mn}+a} r^{-3} dr \tag{3.24}$$

The electric field of dipole $\vec{p}_n$ is:

$$\vec{E}_{total,n} = \vec{E}_{inc} + \sum_{k=1(k\neq n)}^{N} \vec{E}_{kn} \tag{3.25}$$

combining equation (3.21), (3.23), and (3.25) gives:

$$\vec{p}_n = \varepsilon_m \alpha \vec{E}_{inc} + \frac{\alpha}{4\pi} \sum_{k=1(k\neq n)}^{N} \left(3(\vec{p}_k \cdot \hat{r}_{kn})\hat{r}_{kn} - \vec{p}_k\right) \cdot \left|\bar{r}_{kn}\right|^{-3} \tag{3.26}$$

where $\alpha = 4\pi a^3(\varepsilon - \varepsilon_m)/(\varepsilon + 2\varepsilon_m)$. Using the Lorentz model [29], we calculated the total absorption W_{abs} by all nanospheres in the system:

$$W_{abs} = \sum_{m=1}^{N} \frac{\omega}{2} \operatorname{Im}\left(\vec{p}_m \cdot \vec{E}^{*}_{total,m}\right) \tag{3.27}$$

To simulate the field-enhancement by the nanospheres, the electric-field-energy storage W_{store} inside the microshell was numerically calculated through an integration of the electric energy-density over an interparticle-space volume υ, which covers the space from $r = R + a$ to $r = R - a$ excluding the nanosphere volume.

$$W_{store} = \int_{\upsilon} \frac{1}{4}\varepsilon_m \left(\vec{E}_{inc} + \vec{E}_s(\vec{r})\right) \cdot \left(\vec{E}_{inc} + \vec{E}_s(\vec{r})\right)^{*} d\upsilon \tag{3.28}$$

where $\vec{E}_s(\vec{r})$ is the electric field from all the nanospheres following equation (3.22). The values of ε, which are wavelength-dependent, were taken from the literature [30].

The dimension constants in our model (R_0 , N , and a) are from our measured data. The value of ε_m was assigned with 2.5, referring to literature [3a].

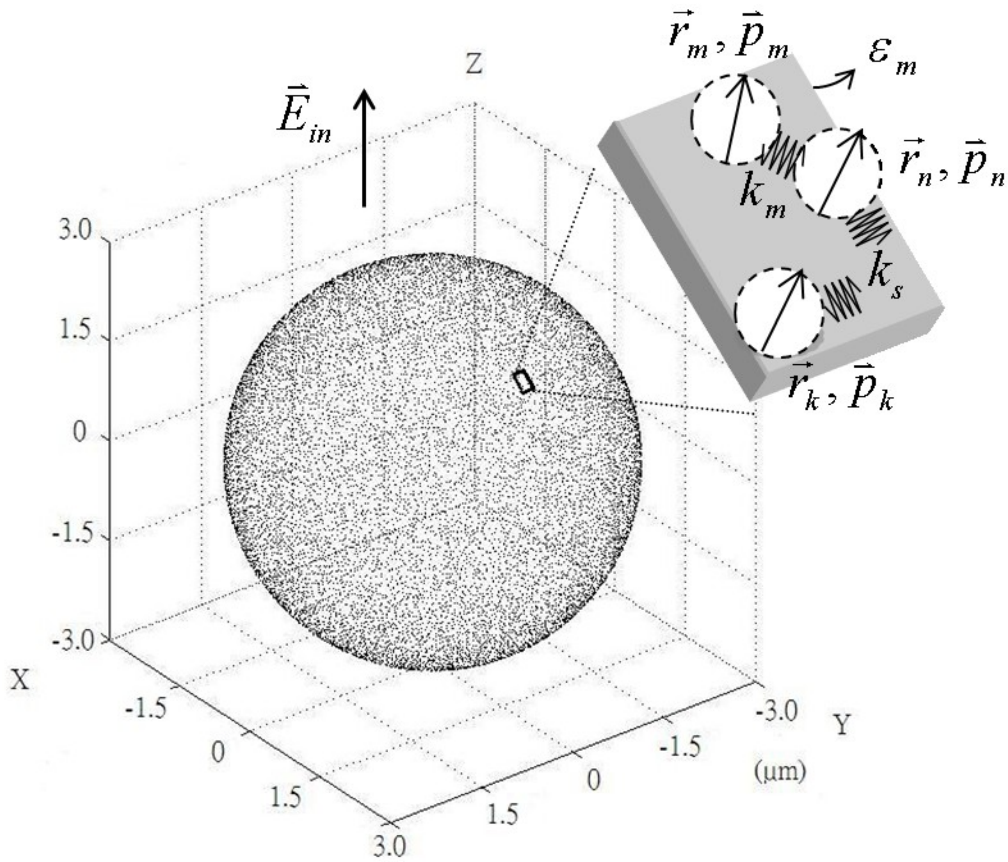

Figure 3.10 The theoretical model of a microshell: the positions $\vec{r}_m$ of the nanospheres on the microshell are randomly assigned; the values of polarization $\vec{p}_m$ (induced by $\vec{E}_{in}$) are calculated based on the theory of particle interactions; spring constants k_s and k_m are used to model the redistribution of nanospheres during the shrinkage of the microshell.

3.3.2b Comparison with the Experimental Results

We used the results of our theoretical model to explain the changes of the modified microshell spectra in our previous experiment. Figure 3.11(a) shows the simulated absorption spectra of the gold-nanospheres in different deformation stages. The simulated spectra show drops of the absorption peak around 530 nm and a drastic increase in NIR absorption; similar changes were observed in the experimental spectra as depicted in figure 3.5(c). Figure 3.11(b) shows the distribution of interparticle distances among neighboring nanospheres; the number of particle in contact (at which $|r_{mn}|$ = 40 nm) gradually increases as the shell radius shrinks. Note that, the particle interaction increases when the interparticle distance decreases. Therefore, the simulated spectra show that an overall decrease of the interparticle distance enhances the particle interaction and changes the nanosphere absorptions, including the drop around 530 nm and the rise in the NIR region. Our previous calculations using dual particle model show that the change at 530 nm and NIR absorption stems from the shift of particle absorption to higher wavelength, when plasmonic interaction among close particles is enhanced.

The simulation results in figure 3.11(a) only include the absorption change of the Au nanospheres; the polymeric material was assumed to be non-absorptive (by using a real dielectric constant ε_m) in our model; therefore, the absorption of azobenzene was absent in our simulation result. The absorption of water was also not included, and the result in Figure5a does not show the observed changes (figure 3.5(c)) at 970 nm. The spectrum changes at NIR and the UV region are explained by using the calculation of the energy storage W_{store}.

The absorption of electromagnetic energy by an optical system is proportional to the amount of energy stored in the system [29]. Accordingly, we may calculate the absorption changes at NIR and the UV region by using the calculated value of W_{store}, which shows the energy-storage in the polymeric material of the microshell. We approximated the value of W_{store} by first calculating the energy density at representative positions on the large sphere; these positions includes the center spots between neighboring nanospheres, the central point among every three neighboring nanospheres, and the position at the surface of each nanosphere that is closest to a neighboring spheres. The distribution of energy over the surface of the large sphere was approached by integrating an overall energy using these representative energy densities, giving W_{store}. Figure 3.11(c) shows that W_{store} increases in the NIR region and decreases in the UV region as the shell diameter changes from 6.2 μm to 4.0 μm. In the NIR region, as the shell shrinks, the value of W_{store} increases by more than ten folds of its initial value. Similar to our previous Mie model, this change indicates a significant field enhancement in the NIR region; the decrease of particle spacings aids the resonance of NIR electromagnetic wave. In the UV region, our calculation shows that the drop of W_{store} is due to the shell-volume decrease and also due to the lack of field enhancement in the UV region; this drop was also observed in our experimental spectra at figure 3.3(c). The simulation results of W_{store} support that the increased absorption at the 970 nm peak and the absorption drop of the UV region in the experiment spectrum are due to the different degrees of field enhancement in the NIR and UV regions by the microshell and also due to the volume contraction during the UV irradiation.

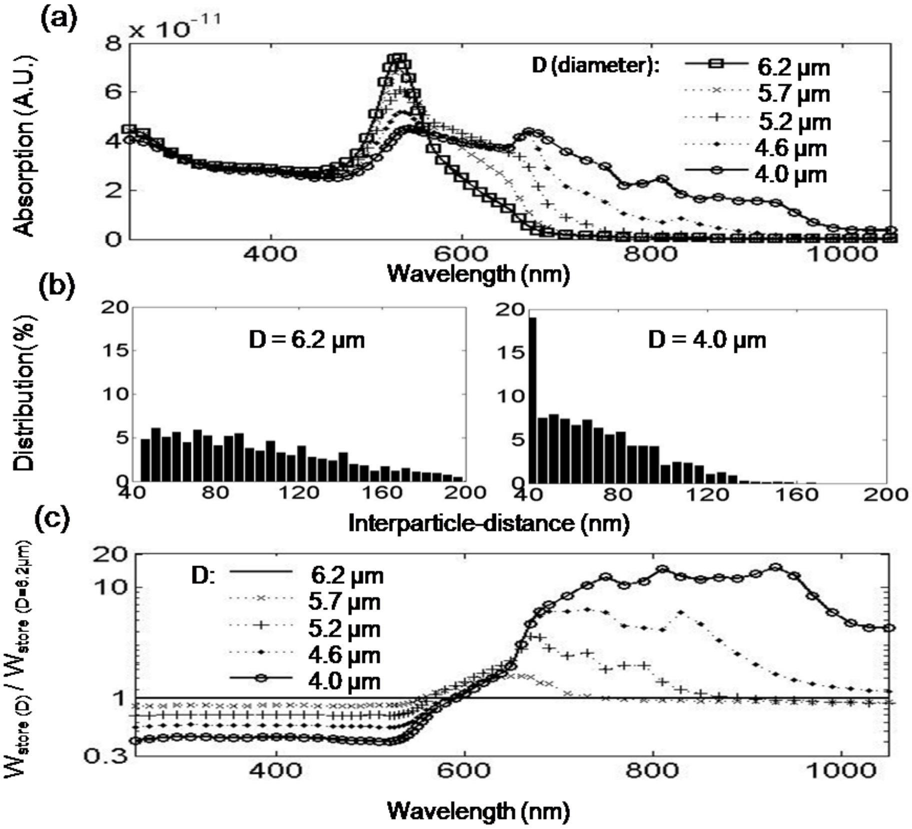

Figure 3.11 Simulation results of the microshell model (in which the microshell deforms from 6.2 μm to 4.0 μm): (a) the change in the absorption spectrum of the Au-coated microshells at different moments of deformation; (b) the change in the length distribution of the interparticle distances among neighboring nanospheres; (c) the change of energy storage during the shrinkage; the effect of sphere shrinkage (D decrease) on the field enhancement is shown by the ratio $W_{store(D)}/W_{store(6.2\mu m)}$. 6.2 μm is the initial shell diameter.

3.4 Conclusion

We successfully developed a photo-tunable particulate-medium, of which the NIR absorption is tunable by UV light. By using the LBL method with azobenzene-based polyelectrolytes, we fabricated gold-nanosphere coated microshells that shrink upon UV irradiation. The shrinkage of the microshells reduces the inter-particle spacing among nanospheres and causes drastic changes in the absorption spectrum and significantly enhanced absorption in the NIR region was observed.

To reveal the physics behind the observed tunable absorption by Au microshells, we simulate the multi-sphere system using the modified Mie scattering and also a dipole approximating model. The calculation results were used to explained different parts of the observed changes at the absorption spectra of the shrinking Au microshells.

A comparison between our experiment and simulated results shows: (a) the main cause of the spectrum changes was the enhancement of particle interactions among nanospheres, and (b) the UV light induced shrinkage significantly increases the nanosphere absorption and the field enhancement in the NIR region, which is the red-shift of particle absorption due to enhanced plasmonic couplings..

3.5 Reference

1. Mie G 1908 “Beiträge zur Optik trüber Medien speziell kolloidaler Metallösungen” *Ann. Phys.* **25** 376-445.
2. (a) Tolga Atay T, Song J and Nurmikko A V 2004 *Nano. Lett.* **4** 1627-31; (b) Tamaru H, Kuwata H, Miyazaki H T and Miyano K 2002 *Appl. Phys. Lett.* **80** 1826.
3. (a) Schmitt J, Mächtle P, Eck D, Möhwald H and Helm C A 1999 *Langmuir* ***15*** 3256-3266; (b) Rechberger W, Hohenau A, Leitner A, Krenn JR, Lamprecht B and Aussenegg FR 2003 *Opt. Commun* .**220** 137–141.
4. Tian Y and Tatsuma T 2005 *J. Am. Chem. Soc.* **127** 7632 – 7637.
5. Nomura W, Ohtsu M and Yatsui T 2005 *App. Phys. Lett.* **86** 181108.
6. Joannnopoulos J D, Meade R D and Winn J N 1995 *Photonic Crystal: Molding the Flow of Light* Princeton University Press Princeton NJ.
7. Feringa B L 2001 *Molecular Switches* WILEY-VCH GmbH Weinheim Germany 399.
8. (a) Yu Y, Nakano M and Ikeda T 2003 *Nature* **425** 145; (b) Ikeda T, Nakano M, Yu Y, Tsutsumi O and Kanazawa A 2003 *Adv. Mater.* **15** 201; (c) Li M, Keller P, Li B, Wang X and Brunet M 2003 *Adv. Mater.* **15** 569.(d) Y. Li, Y. He, X. Tong, X. Wang, *J. Am. Chem. Soc.* **2005**, 127, 2402.
9. (a) Chung D, Fukuda T, Takanishi Y, Ishikawa K, Matsuda H, Takezoe H and Osipov M A 2002 *J. Appl. Phys.* **92** 1841 (b) Bachelot R, H’Dhili F, Barchiesi D, Lerondel G, Fikri R, Royer P, Landraud N, Peretti J, Chaput F, Lampel G, Boilot J and Lahlil K 2003 *J. Appl. Phys.* **94** 2060.

10. Li Y, He Y, Tong X and Wang X 2005 *J. Am. Chem. Soc.* **127** 2402.

11. Han L, Tang T, Chen S and Webber S E 2005 *International Conference on Bio-Nano-Information Fusion*, *LA,* USA.

12. (a) Decher G, Hong J D and Schmitt J 1992 *Thin Solid Films* **210** 831; (b) Decher G 1997 *Science* **277** 1232; (c) Caruso F 2000 *Chem. Eur. J* **6** 413; (d) Sukhorukov G B, Shchukin D G, Dong W, Möhwald H, Lulevich V V and Vinogradova O I 2004 *Macromol. Chem. Phys.* **205** 530; (e) Schneider G and Decher G 2004 *Nano. Lett.* **4** 1833; (f) Mayya K S, Gittins D I, Dibaj A M and Caruso F 2001 *Nano. Lett.* **1** 727.

13. Palmer K F and Williams D 1974 *J. Opt. Soc. Am.* **64** 1107-1110.

14. Craig F B and Donld R H 1983 *Absorption and Scattering of Light by Small Particles,* John Wiley & Sons, Canada, 136-39.

15. Shvalagin, V. V., Stroyuk, A. L., and Kuchmii, S. Y., 2007, "Photochemical synthesis *of ZnO/Ag nanocomposites," J. Nanoparticle Research*, **9**(3), pp. 427-440.

16. Vandenbem, C. and Vigneron, J. P., 2005, "Mie resonances of dielectric spheres in face-centered cubic photonic crystals," J. Opt. Soc. Am. A, **22** (6), pp. 1042-47.

17. Banerjee, M., Datta, S. K., Saha, H., 2005, "Enhanced optical absorption in a thin silicon layer with nanovoids," Nanotechnology, **16**(9), pp. 1542-1548.

18. Mackowski, D. W. 1991 "Analysis of Radiative Scattering for Multiple Sphere Configurations," *Proceedings: Mathematical and Physical Sciences*, **433** (1889), pp. 599-614.

19. Jackson, J. D. 1999, *Classical Electrodynamics* 3rd ed John Wiley & Sons, USA, pp. 352-56.

20. Chern, R., Liu, X., and Chang, C. 2007" Particle plasmons of metal nanospheres: Application of multiple scattering approach," *Phys. Review E* **76**, pp. 016609.

21. Segelstein, D., 1981, "The Complex Refractive Index of Water," M.S. Thesis, University of Missouri, Kansas City, Missouri, USA.

22. Weaver, J. H. and Frederikse, H. P. R. 2001, Optical Properties of Selected Elements (82 Ed), CRC Press, Boca Raton, FL, USA.

23. Kreibig, U. and Vollmer, M., 1995 Optical Properties of Metal Clusters, Springer, New York.

24. Kawata, S., 2001, Near-Field Optics and Surface Plasmon Polaritons, Springer, New York.

25. Johnson, P. B. and Christy, R. W., 1972, "Optical Constants of the Noble Metals," *Phys. Rev. B.*, 6, pp. 4370-79.

26. Kittel, C., 1971, Introduction to Solid State Physics 4th ed. Wiley Canada, pp. 248.

27. (a) Craig F B and Donld R H 1983 Absorption and Scattering of Light by Small Particles, John Wiley & Sons, Canada, 325-29; (b) Maier S A and Atwater H A 2005 Appl. Phys. Rev. 98 011101-1-10.

28. Jackson J D 1999 Classical Electrodynamics 3rd ed John Wiley & Sons, USA, 407-411.

29. Jackson J D 1999 *Classical Electrodynamics* 3rd ed John Wiley & Sons, USA, 309-313.

30. Johnson P B and Christy R W 1972 *Phys. Rev. B* **6** 4370-9.

Chapter 4 : Light-Driven Micro-turbines

4.1 Introduction

Invented in the late 19th century by Sir William Crookes, The Crookes radiometer (Figure 4.1) was probably the first light-powered machine created by man. Sealed in a glass container at rough vacuum (10~1000 mTorr), the moving part of the radiometer is a turbine with asymmetrically colored blades; each blade has one side dark and the other side bright. Upon irradiation, the turbine turns with the dark sides retreat from the source of light; the generally accepted cause of this motion is the convection from the asymmetric heating by light. Believing that the same mechanism can be used to build micro-actuators, we started a project to build a light-powered micro-turbine which is a miniature Crookes radiometer. The light-driven microturbine was aimed to be a spinning micromirror for cardio-spectroscopic applications, in which the use of electricity is undesirable.

To understand the physics behind a Crookes radiometer and to optimize the design of a light-powered micro-turbine, we also simulate the air dynamics of the micro-turbine system. The simulation model could be based on either a continuous, Navier-Stokes approach [1] or a discrete, molecular dynamics calculation [2]. Although a Navier-Stokes approach is more computationally economic compared to molecular dynamics calculation, we must first evaluate the validity of both method based on the physics of our simulated system.

4.1.1 Validity of Navier-Stokes Approach to the Analysis of Crookes Radiometer

To analyze Crookes radiometer, the validity of using the Navier-Stokes continuous equation depends on a characteristic dimension L of the gas flow and also on the mean free path (MFP) λ of the gas molecules (3). L is defined as the length of a macroscale gradient, which shows a distribution of dynamics variables, such as velocity or temperature. λ is the average distance that a molecule travels between two sequential collisions, which change the velocity of the molecule. A continuum approach assumes that the fluctuations of the dynamics variables among individual molecules can be averaged to build a smooth gradient over the dimension, L. To guarantee the accuracy of this assumption, a rule of thumb is given by [4]:

$$\lambda/L < 0.1 \tag{4.1}$$

When $\lambda/L > 0.1$, the fluctuations in the gradient are considered important, and it becomes necessary to consider the microscopic gas dynamics within the gradient space. Another guideline to check the validity of continuum approach is a ratio between L and the average molecule spacing δ:

$$L/\delta > 100 \tag{4.2}$$

Outside this limit, the Navier-Stokes approach is considered invalid and a complete microscopic approach should be used instead. Figure 4.2 shows a chart that illustrates the validity of Navier-Stokes approach using both guideline equations [4].

In the case of Crookes radiometer, a turbine blade with distinct temperatures on each side generates a temperature gradient. We conclude that the sharpest gradient is thus created near the edges of each blade, where the two surface temperatures meet; therefore, we use the blade thickness as our characteristic dimension and L = h. The next step is to evaluate the λ and δ of air in the radiometer system. From our preliminary experiment using a commercial radiometer, the turbine spins at a range of air pressure from 10 to 1000 mTorr. In this range and at a temperature of 25 ˚C, the mean free path and the average molecular spacing of air are [4]:

$$5.187 \times 10^{-5} m < \lambda_{radiometer} < 5.187 \times 10^{-3} m \tag{4.3}$$

$$3.137 \times 10^{-8} m < \delta_{radiometer} < 1.456 \times 10^{-7} m \tag{4.4}$$

The blade thickness of a micro-turbine we built was approximately 50 μm, or 5×10^{-5} m. Thus $L = 5 \times 10^{-5}\ m$. Using the guideline equations to check the validity of Navier-Stokes approach, we get:

$$1.0375 < \lambda_{radiometer}/L < 10.375 \tag{4.5}$$

$$343.4 < L/\delta_{radiometer} < 1594 \tag{4.6}$$

The result shows that, in this pressure range, the first guideline equation is failed by more than one order and the second is met only marginally. The Navier-Stokes approach is thus not appropriate for our turbine system; a microscopic approach is necessary.

4.1.2 Direct Simulation Monte Carlo Method

We used Direct Simulation Monte Carlo (DSMC) method [4] as our microscopic approach to analyze Crookes radiometer. Developed by Graeme A. Bird, DSMC Method is based on molecular dynamics and also on the statistical mechanics [2] of gas molecules. In DSMC, realistic gas molecules in a physics space are simulated by a smaller number of representative molecules. The molecule positions and velocities in the physics space are calculated at a sequence of time steps. At each time step, representative collisions among the simulated molecules, and between the molecules and system boundaries, are simulated by computer program. The location of collision events, the select of collision pairs, and the post-collision velocities of the collided molecules are calculated based the law of energy conservation, momentum conservation, and also on the theoretical distribution of probable values for the dynamics system. Physics properties, such as pressure and temperature, are sampled by multiple subspaces in the whole simulation domain. Figure 4.3 shows a flow chart of a typical DSMC program. Compared to the simulations of complete molecular dynamics, DSMC method is computationally economic and suitable for a system of much larger scale. Our DSMC program was modified from a 1D example given by the reference [5]. We designed the solid boundaries in the system according to the geometry of our micro-turbine. To minimize the size of simulation space, we also use periodic boundaries to take account the axial symmetry of the simulated flow. The details about our simulated space, the boundaries, and the computational functions of our DSMC program will be discussed in section 4.5 of this chapter.

4.1.3 Digital Micro-mirror Device for Polymeric Micro-fabrication

Reported in section 4.2 is a Digital Micro-mirror Device (DMD) system to build complex 3-dimentional (3D) micro-structures; we also use this system to build the micro-turbine.

In the recent years, organic-based materials for micro-fabrications have gained more and more attention in many fields, such as biomedical engineering and micro/nano-optics, for their chemical properties and also the flexibility and simplicity in fabrication. Fabrication processes using digital micro-mirror-array devices (DMD) are among the most efficient methods to build polymeric micro-structures. DMD-fabrications build micro-structures by 1-dimentional (1D) scanning. Before a DMD process takes place, a digital 3D-model is split into sequential, cross-sectional pictures. These pictures are digitally sent to the DMD mother-board, where multiple micro-mirrors are selectively turned on or off to resemble the cross-sectional pictures. The mirror-mirror-array is then illuminated by a uniform, ultraviolet (UV) light source, and the images of the illuminated mirror-array are projected, using an optical lens, onto the surface of photo-curable liquids positioned at the focal plane of the lens. UV light turns the surfaces of the curable-liquids into thin, solid slides that resemble the model cross-sections. The just-formed slide is then moved downward with a stage dipped in the liquid for the formation of a new layer. As this process repeats, the 3D model is gradually reconstructed from the photo-curable liquid. Because DMD fabrications build 3D structures layer-by-layer using only one actuator for the linear-motion of stages, they become superior tools of higher fabrication speed, reduced mechanical complexity, and also minimized system-controls. Limited only by the quality of the projection lenses, the smallest feature a DMD system can possibly build is sized by the diffraction limit of the curing light, which is below 1 μm. In our previous projects to build tissue engineering scaffolds [6], we developed a DMD system which is capable to build 3D micro-structures of complex geometries. It is convenient to use this system for our micro-turbine. The setup of our DMD system, the use of materials, and the details about the building of a micro-turbine will be reported in section 4.3.

4.1.4 Localized Formation of Gold Nanoparticles as Photo-absorption Coating

To create a temperature gradient across the blade upon illumination, the blades of the micro-turbine need to be coated with a photo-absorber on one side. The coating could not be performed manually due to the small size of the turbine. Based on our study in chapter 3, concentrated metallic nanoparticles have exponentially enhanced plasmonic absorption and thus may serve as an effective light absorbing agent at one side of the blade. In our preliminary study [7], growth of gold nanoparticles was localized on a woodpile microstructure built by the DMD system. We used a heterogeneous scheme to build different parts of the structure with distinct polymers; only one of the polymers can be chemically modified to recover gold from a precursor solution. The result showed a conclusive selectivity of nanoparticles growth at the woodpile structure. In section 4.3, we will report the application of this self-assembly technique to create a heterogeneous coating for our micro-turbine.

Figure 4.1 A Crookes Radiometer is an asymmetrically colored turbine in a low vacuum glass bulb. The blades have one side dark and the other side bright. Upon irradiation, the turbine turns with the dark sides retreat from the source of light; the causes widely accepted are an asymmetric heating by photo energy across the blades and an asymmetric heat transfer to the surrounding air molecules. This photograph was copied from an internet website, Wikipedia [22].

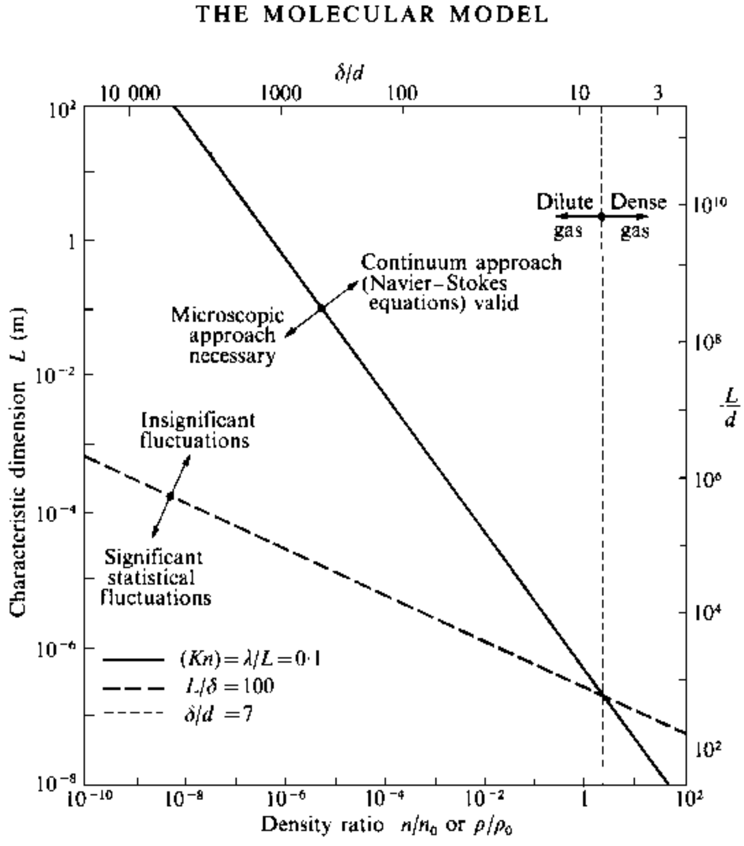

Effective Limits of major approximations (air, d=3.7 × 10^{-10})

Figure 4.2 The guideline equations to check the validity of Navier-Stokes approach for air are plotted in a chart of density ratio (n_0 is the number density at 1 atm and 0˚C) vs. L. The system of our micro-turbine falls in the area "microscopic approach necessary", where Navier-Stokes approach alone is insufficient; our system is also close to the area "significant statistical fluctuation", where the Navier-Stokes approach becomes invalid. This chart is copied from page 19 of reference [4].

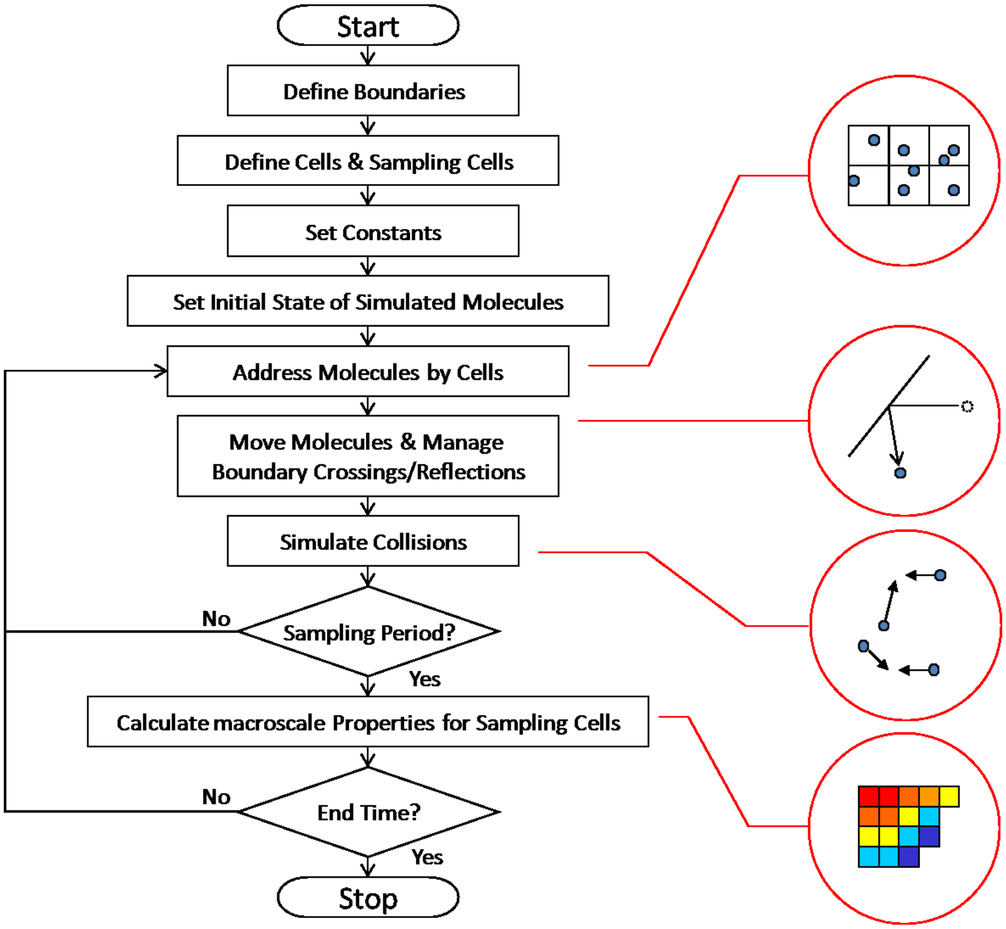

Figure 4.3 In DSMC programming, gas molecules in a system are simulated by a smaller number of simulated molecules, each represents tens of thousands of real molecules. In the simulation, these simulated molecules move, collide into each other, and interact with system boundaries according to the statistical mechanics of gas. Macroscale properties in the system, such as pressure and temperature, are calculated only from the positions and velocities of the simulated particles.

4.2 DMD-Based Fabrication Equipment, Process, and Materials

4.2.1 Setup a DMD-based Fabrication System

Our fabrication system (Figure 4.4) includes a servo-stage (CMA-25-CCCL & ESP300, Newport), three syringe pumps, a glass window, a DMD system (Discovery 1100, Texas Instruments), a UV lamp (200W, S2000, EXFO), and a UV-grade projection lens (NT57-541 Megapixel, Edmond Optics). The syringe pumps inject two types of photo-curable monomers and one solvent to an outlet on the servo-stage. The DMD chip is composed of an array (1024 by 768) of micro-mirrors that form reflective patterns. These micro-mirrors are illuminated by the UV light from the lamp using an 8 mm light guide. Upon illumination, the UV images of the reflective patterns are projected onto the photo-curable monomer by the projection lens. The monomers, loaded above the servo-stage, are selectively cured by the UV images and form microstructure layers.

The glass window is fixed right above the microstructure and is also at the focal point of the projection lens. Before UV-exposure, the monomers are pumped to fill the space between the window and the microstructure, which controls the thickness of the microstructure layers. Upon UV illumination, the monomer layers below the window are cured selectively, resembling the pattern of the micro-mirror array. The window is coated with a fluorinated agent, (tridecafluoro-1,1,2,2-tetrahydrooctyl) trichlorosilane, to help release the microstructure from the window surface after UV-curing. The coating process for the glass-window is reported elsewhere [8]. The servo-stage, syringe-pumps, DMD system, and the UV lamp are connected to a personal computer (PC); with the DMD system being controlled by the PC through programming.

4.2.2 Procedures for Homogeneous Fabrication

Typical DMD fabrication processes build 3D micro-structures from a homogeneous material. The sub-figures A-B-C2-D2 in Figure 4.5 shows the process for homogenous fabrication. The servo-stage was positioned a distance below the glass window to start; this distance determines the thickness of the first layer of a 3D structure to be built. A monomer was pumped from the stage-outlet into the gap between the window and the servo-stage. The monomer is exposed to UV pattern to build a structural layer. After the first layer was built (Figure 4.5(B)), the stage was repositioned downward, normally 0.5 mm, pulling the structure away from the glass-window. The release was aided by the low surface energy of the fluoride coating. A mild solvent (isopropanol alcohol) was pumped into the gap to purge any partially polymerized monomer; these unwanted oligomers may solidify and block the microstructure-pores in later exposures. The used solvent was drained from the stage and dried by applying a gentle air flow through the micro-structure. In order to build a new layer above the just-formed structure (C2 to D2,) the stage was repositioned upward until the top of the structure was situated one layer-thick below the glass-slide. Fresh monomer was pumped again into the gap, and the above steps were repeated to create the next layer.

4.2.3 Procedures for Heterogeneous Fabrication

Heterogeneous fabrication, i.e., building micro-structures with localized materials of distinct mechanical, optical, and chemical properties, is important to the development of micro-actuators. Localization of these distinct properties may allow us to create asymmetric interaction between a microstructure and its surroundings to cause motions. Using our DMD system, a fabrication process was developed for manufacture heterogeneous structures by switching monomers for the same structure layer. To build a structure with two materials in the same layer (C1 to D1), for example, monomers were switched after purging, and the stage was moved back to the position it held before the UV exposure step. The UV-exposure, purging, and monomer switching routines were repeated until the entire microstructure was built.

4.2.4 Examples of DMD-based Fabrication

Figure 6 shows several devices built by using our DMD system. Figure 4.6(A) shows a micro-turbine which is 2mm in diameter and 50 μm in blade thickness. The turbine was built homogeneous by using 1,6-hexanediol diacrylate (HDDA) as a photo-curable monomer. We used the similar pattern to build our light-driven micro-turbine. The DMD System is also capable to build free-standing micro-structures as shown in figure 4.6(B) by stacking intercrossing “woodpile” layers. Figure 4.6(C) is one example of heterogeneous fabrication; a woodpile structure similar to (B) was localized with two types of fluorescent particles, which emit visible light of different wavelength under a fluorescent microscope. We already used this technique to build biological scaffolds for tissue engineering [9], where different biological growth factor can be localized to build a desired extra-cellular environment and to control cell growth [10]. Figure 4.6(D) shows a 3D micro-structure built by patterning a sequence of different cross-section images on poly (ethylene glycol) diacrylate (PEGDA).

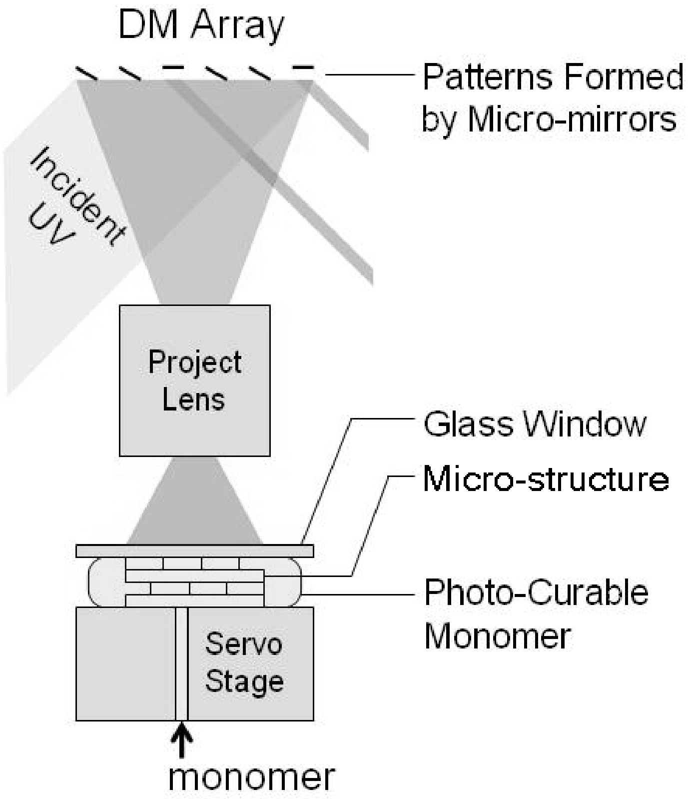

Figure 4.4 A 3D micro-structure is built layer-by layer. A structural layer is formed when the photo-curable monomer is selectively solidified by a DMD pattern, projected by UV light through an optical lens. The glass window guarantees the flatness of each layer. A fluorinated coating agent on the glass aids to release the microstructures from the glass window.

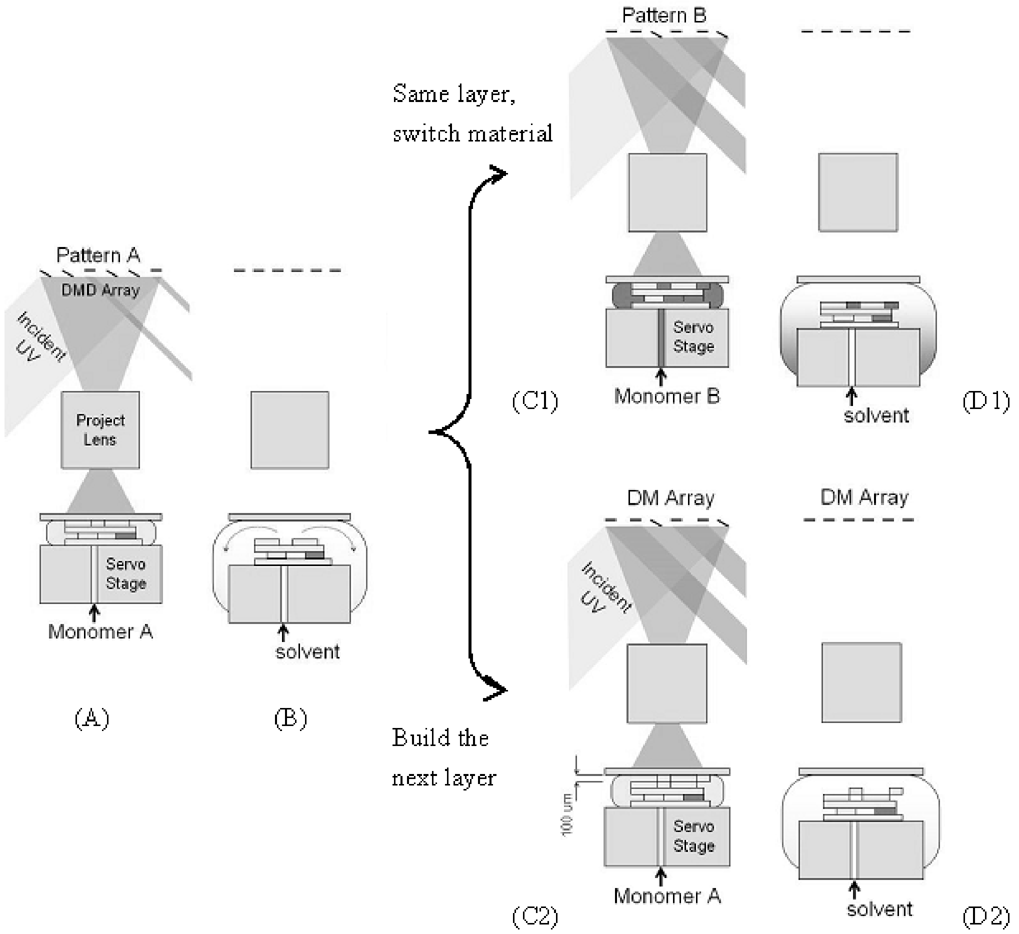

Figure 4.5 The DMD fabrication process includes two features: homogeneous and heterogeneous fabrication. The homogeneous process (A-B-C2-D2) builds a micro-structure with a single monomer. By switching monomers to build each layer (A-B-C1-D1), a micro-structure may have localized, distinct material properties and becomes heterogeneous.

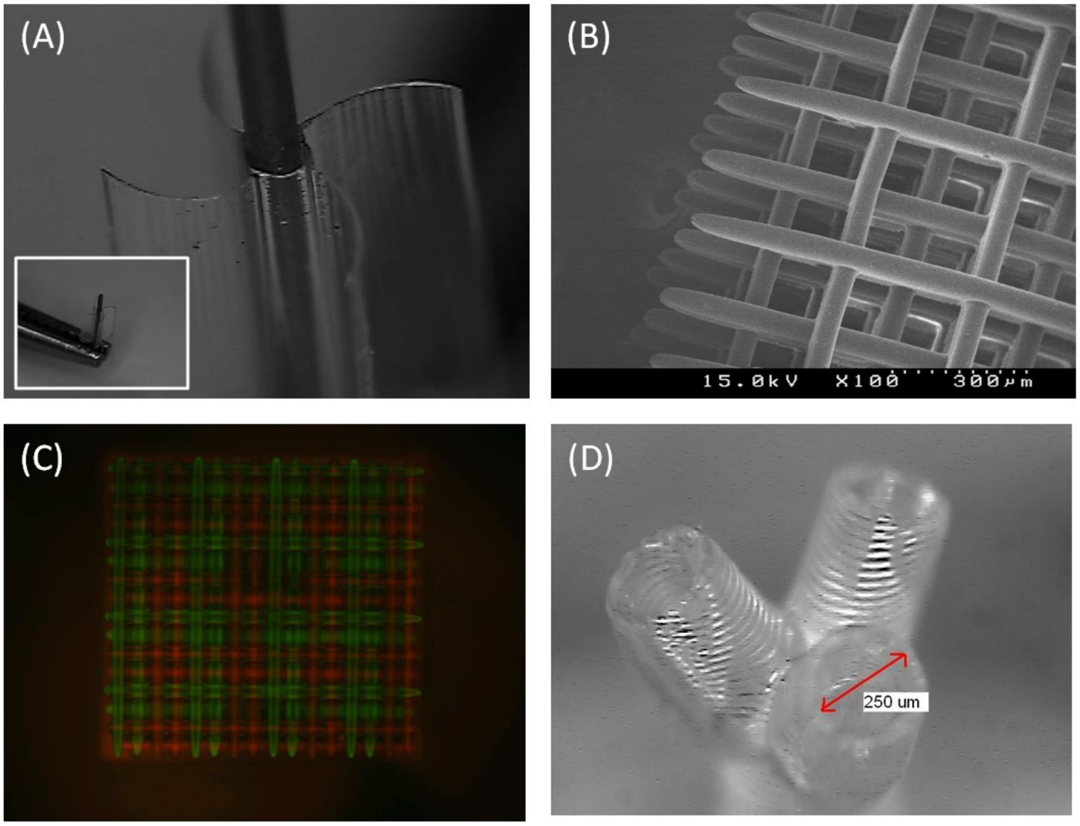

Figure 4.6 Different micro-structures built by using the DMD system: (A) a micro-turbine built from 1,6-hexanidiol diacrylate (HDDA), the inset shows its size compared to the tip of a tweezer; (B) a poly (ethylene glycol) diacrylate (PEGDA) woodpile structure under scanning electronic microscopy (SEM); (C) a heterogeneously fabricated PEGDA structure; geometrically similar to the previous one, but loaded with two types of localized fluorescent particles; and (D) a three-branched micro-tube formed by patterning different cross-section images on PEGDA.

4.2.5 Materials for DMD-based Fabrication: I. Structural Materials

The materials for our DMD fabrication are photo-polymerizable monomers or pre-polymers. To build a rigid micro-structure, we use the materials that have multiple acrylate groups in each molecule. Based on our experience, the following multi-acrylates are effective materials for the DMD fabrication:

Poly (ethylene glycol) diacrylate (PEGDA)

This monomer forms structures with certain degrees of elasticity. The elasticity is roughly proportional to its molecular weight. PEGDA of different molecular weights, from about 250 to 4,000 g/mole, are commercially available. A structure made from PEGDA of molecular weight higher than 700 g/mole can swell in water and become a hydro-gel. Acrylates with active chemical groups, such as methacrylic acid (MAA) or acrylamide, are sometimes mixed into a PEGDA to build a chemically reactive microstructure. PEGDA is also a bio-compatible monomer and is commonly used to build cell-culture scaffolds for tissue engineering studies.

Trimethylolpropane triacrylate (TMPTA)

TMPTA forms rigid but brittle micro-structures. The major advantages of using TMPTA dwell in its fast curing speed and that it can be used to build micro-structures of high-resolution. TMPTA has a low viscosity compared to other multi-acrylates.

Dipentaerythritol pentaacrylate (DPETPA)

With five acrylate groups in each molecule, this material builds micro-structures harder than TMPTA. DEPTPA molecules also have one hydroxyl group (-OH) each, which form hydrogen bonds in the polymer-networks and raises the toughness of the micro-structure; DEPTPA micro-structures are tougher than TMPTA micro-structures. In strong solvents, such as acetone, cross-linked DEPTPA has a much lower swell rate than other acrylates we used. Thus, DEPTPA is an excellent material for heterogeneous DMD fabrication, where a micro-structure is repeatedly rinsed with organic solvents to switch materials. However, probably due to the hydrogen-bond interactions among molecules, DEPTPA has a high viscosity and it is difficult to build a micro-structure with only DEPTPA. We normally use DEPTPA by mixing it with another monomer of lower viscosity, such as TMPTA or PEGDA.

4.2.6 Materials for DMD-based Fabrication: II. Reactive Materials

Some acrylate materials can be chemically changed in certain environment. Permanent chemical changes are used to modify the material properties in a micro-structure. The most interesting materials are the ones that undergo reversible chemical reactions, which are potentially applicable to build micro-actuators. The following reactive materials were synthesized in our lab:

Dimethyldi (methacryloyloxy-1-ethoxy) silane (DMDMAES)

This monomer has two methacrylate groups in each molecule and is cross-linkable; micro-structures can be built directly from this material. A DMDMAES structure is hydrolysable, i.e., water-degradable. The silane in the center of the DMDMAES molecule can be removed at mildly low PH value:

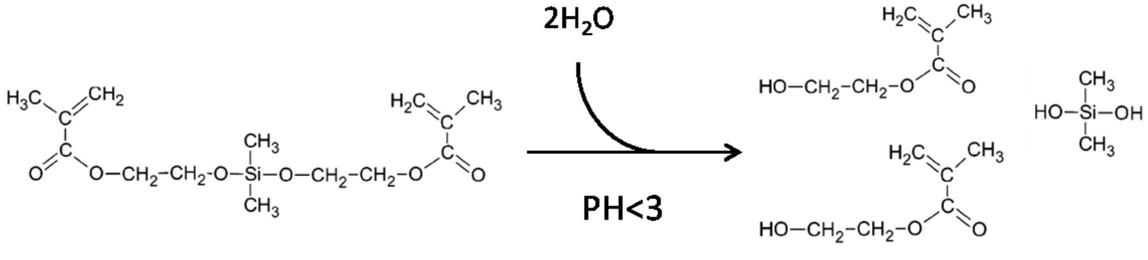

In the micro-structure, each hydrolysis leaves behind a molecular vacancy and two hydroxyl groups, which are affinitive to water. The micro-structure thus swells and becomes a hydro-gel. DMDMAES is normally used as an additive to another kind of monomer; the degree of structure swelling is tuned by the amount of DMDMAES.

4-Nitrophenyl acrylate (NPA)

Similar to DMDMAES but hydrolyze at high PH, NPA can discharge a phenol group and leave behind a wide molecular vacancy and two ionized carboxylic groups. A hydro-gel micro-structure made by using this molecule may have a very high swelling rate. For NPA is not cross-linkable, it is always used as an additive to a multi-acrylate.

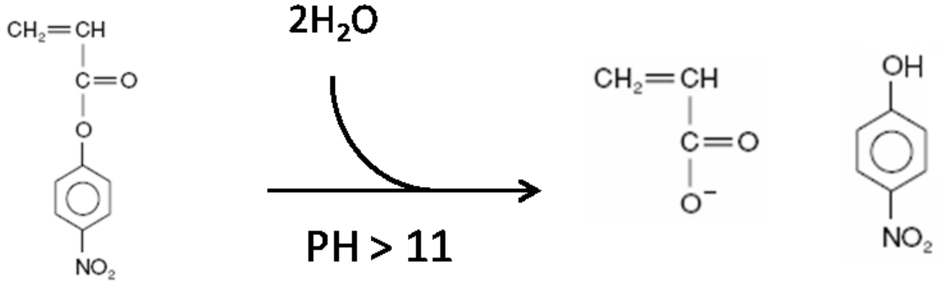

4,4'-diacryloyloxyazobenzene (DAOAB)

The property of azobenzene was introduced in Chapter 3. A monomer with acrylate groups on two sides of an azobenzene may generate structural deformation at a micro-structure. DAOAB absorbs UV light and reduce its molecular length through photoisomerization. The photoisomerization reverses if the molecule is heated or exposed with visible light (VIS). The reversible deformation, once realized in a micro-structure, is applicable to build micro-machines. However, we have not successfully built an actuator with this material.

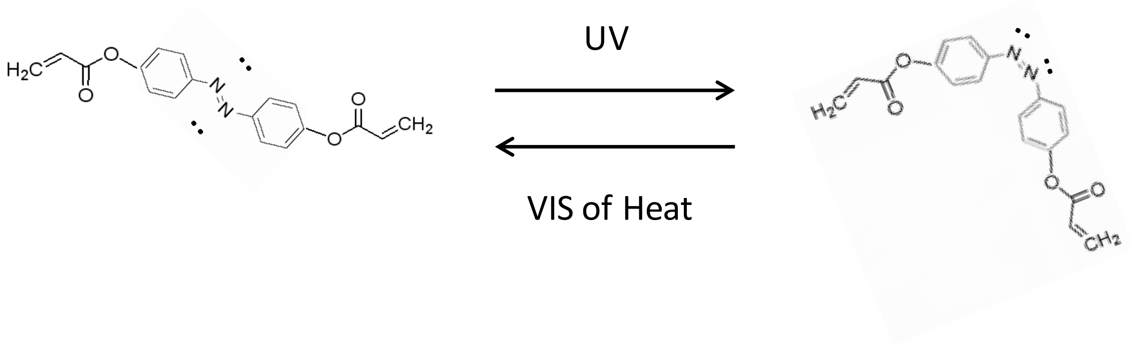

Materials with Carboxylic Groups

Carboxylic groups (-COOH) in a microstructures is one modifiable function group. The oxidizing property of carboxylic moiety allows it to form covalent bond with another molecule. In our studies for tissue engineering, micro-scaffolds built by using DMD were modified to enable the attachment of cells. Figure 4.7 shows a typical process of scaffold modification. The sources of carboxylic groups in a micro-structure are normally MAA or acrylic acid (AA). The source of carboxylic groups can be from the derivatives of natural materials. Recently, glycidyl methacrylated hyaluronic acid (GMHA) gained a lot of attention as a natural material for tissue engineering:

Hyaluronic Acid:

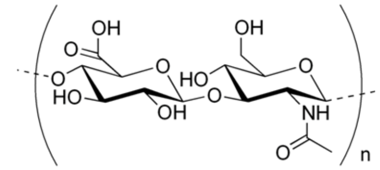

Hyaluronic acid is abundant in the soft tissues of animal bodies and thus is considered one of the most potential biocompatible-materials to build artificial tissues or scaffolds for tissue regrowth [11].

Although promising, the acrylated HA is more difficult to use than other acrylate materials. As a hydrogel, a HA micro-structure can easily deform under gravity during fabrication. The available structural resolution of HA micro-structured built by DMD system is also lower than by other regular multi-acrylates, due to a lower curing rate among the HA molecules. We already started a project to enhance the micro-fabrication technique using HA-based material. In one of our previous experiments, we successfully used DMD fabrication to build several 3D tissue engineering scaffolds from HA. Two of these scaffolds are shown in Figure 4.8.

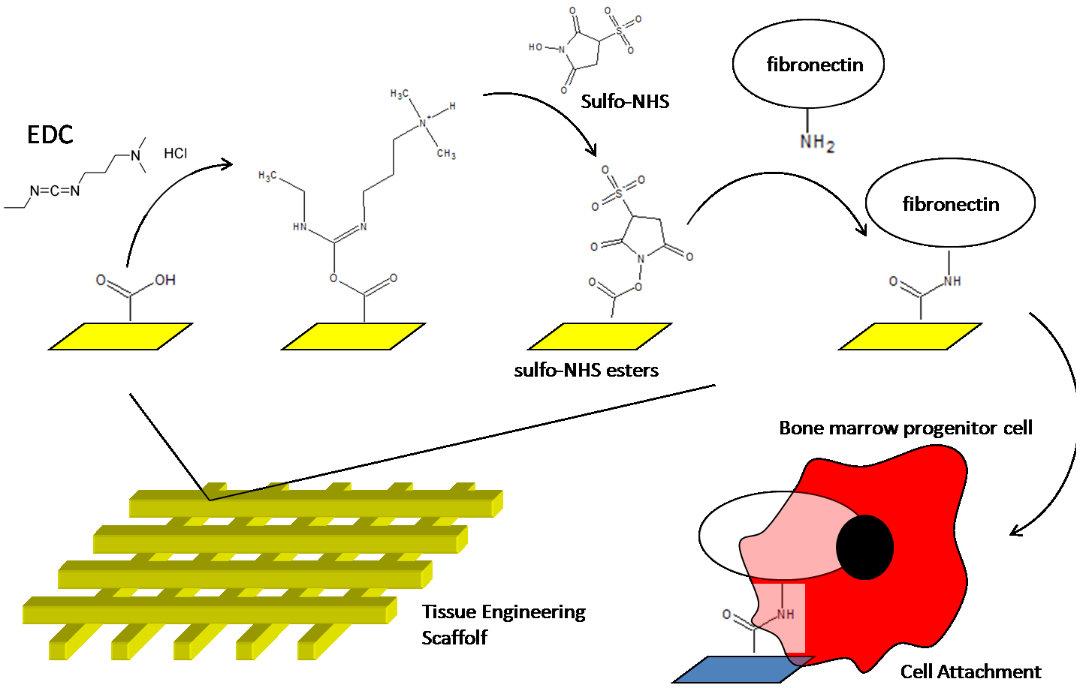

Figure 4.7 The carboxylic groups in a micro-structure may covalently bind to other molecules through their oxidizing property. Carboxylic groups are also bio-compatible; therefore, they are widely used as a target of biological modification for the study of cellular behaviors in a given scaffold.

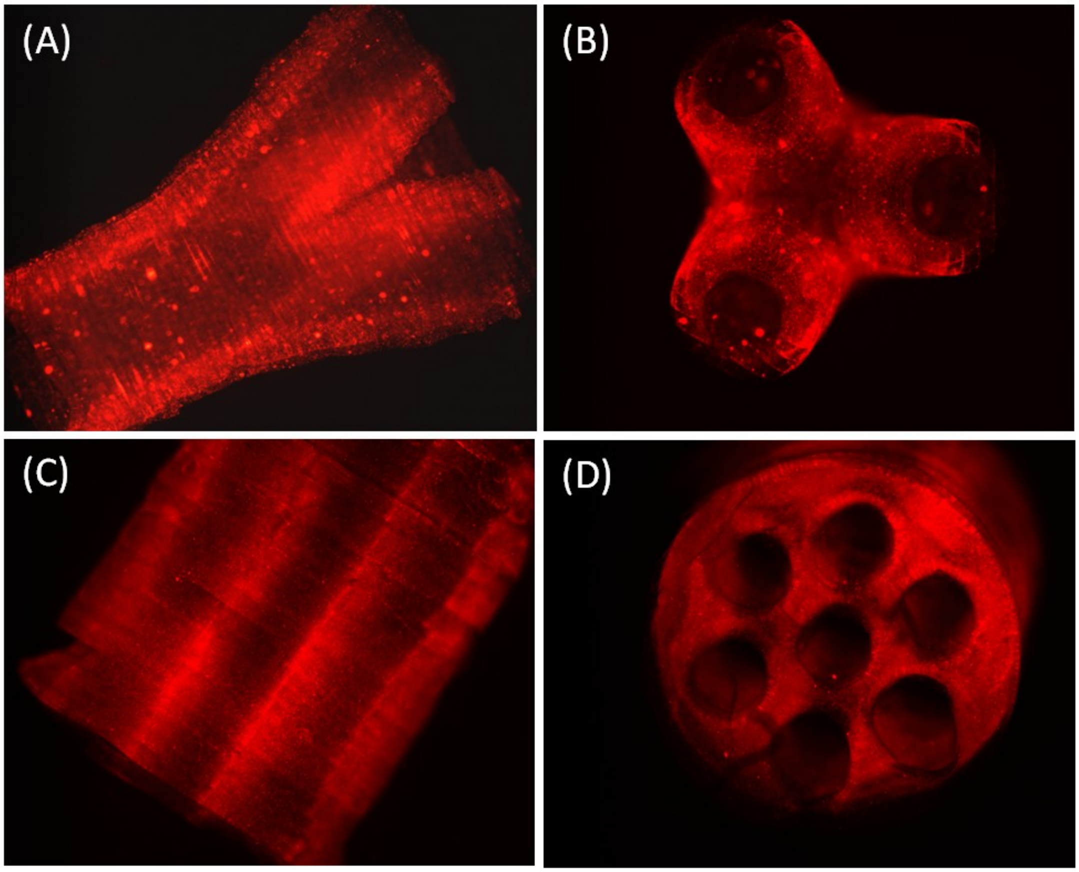

Figure 4.8 Fluorescent images of two HA micro-structures. Tubular micro-structures were built from hyaluronic acid (HA) using DMD fabrication. Acrylated HA can be cross-linked and form biological scaffolds of complex 3D geometry, such as the three-branched structure at (A) and (B). The size of the through-holes of the multi-channels structure at (C) and (D) was about 500 μm.

4.2.7 Materials for DMD-based Fabrication: III. Sacrificial Material

A sacrificial material is a removable matter for temporary molding which supports the fabrication of micro-structures [12]. Developed decades ago, sacrificial materials were standardized for molding semiconductor materials based on metals and metal-oxides. But there is no effective sacrificial material for building micro-structures from organic materials. In the recent years, organic-based materials for micro-fabrications have gained much attention in several evolving areas, such as biomedical engineering and micro/nano-optics, for the abundance of chemical properties and also the flexibility for fabrication of organics polymers. To bring the advantage of organics-based micro-fabrication into full play, however, an effective sacrificial material is necessary. Without sacrificial materials, organic-based micro-fabrication is limited by the resolution along Z-axis (figure 4.9). In DMD fabrication, for example, even though a micro-geometry can be built with a resolution of several micrometers at the X-Y plane, the minimum feature along the Z-axis, which depends on the depth of curing by light, is in the order of a hundred micrometers (figure 4.9(a)). The lack of sacrificial material also limits the geometries that organic materials can be built for. The “hanging” geometry in figure 4.9(b), for example, is hard to make without using a sacrificial material.

An effective sacrificial material for organic-based micro-fabrication needs to have the following important qualities: (1) it is a liquid; (2) it solidifies and is removable at a normal ambient condition; (3) it is chemically and physically inert to the materials in the micro-structures; and (4) it is removable by a solvent which do not affect the geometry of micro-structures.

Standard sacrificial materials for the industry are unfit to organics-based micro-fabrication. These sacrificial materials are grown or removed under harsh environment (high temperatures, low or high PH values), in which an organic microstructure can be damaged. SiO_2, for example, is deposited at high temperature and removed in hydrofluoric acid [13]. Crosslinking materials, such as acrylate or epoxy, can be applied under milder condition but are removed under plasma-oxidation or high-temperature-calcination. Crosslinking monomers may also react with the materials for organic-based micro-fabrication. Traditional sacrificial materials fail to match the aforementioned qualities (2, 4) for building organic micro-structures.

Some have tried finding sacrificial materials for organic-based micro-fabrications. Paraffin wax was used to protect certain areas in a poly (methyl-methacrylate) micro-structure against chemical modification [14]. The wax was applied above melting point, settled at room temperature, and was later dissolved in heated alkanes. For similarly purpose, gelatin was applied and removed above gelation temperatures [15]. These materials are used based on thermal phase-change. For fabrication, heaters and also thermal sensors must be used to effectively control phase-changes; complexity will increase. Furthermore, most organic materials have fairly high yet diverse thermal-expansion-coefficients (TEC). The strain and stress from temperature variation can easily damage the integrity or reduce the resolution of a micro-structure being built. To minimize the problem that thermal-expansion causes, a sacrificial material should be chosen based on having a TEC close to that of the micro-structure. Chemical stability of materials under elevated temperature is another issue. The requirement of Cyto-viability, a major concern of building cell-trapping tissue-engineering-scaffolds, also rules out using heaters. Complicating and difficult to use, a sacrificial material based on thermal phase-change is far from an ideal choice.

To overcome the difficulty of controlling the Z-axis resolution for polymer-based micro-fabrication, we created a new type of sacrificial material.

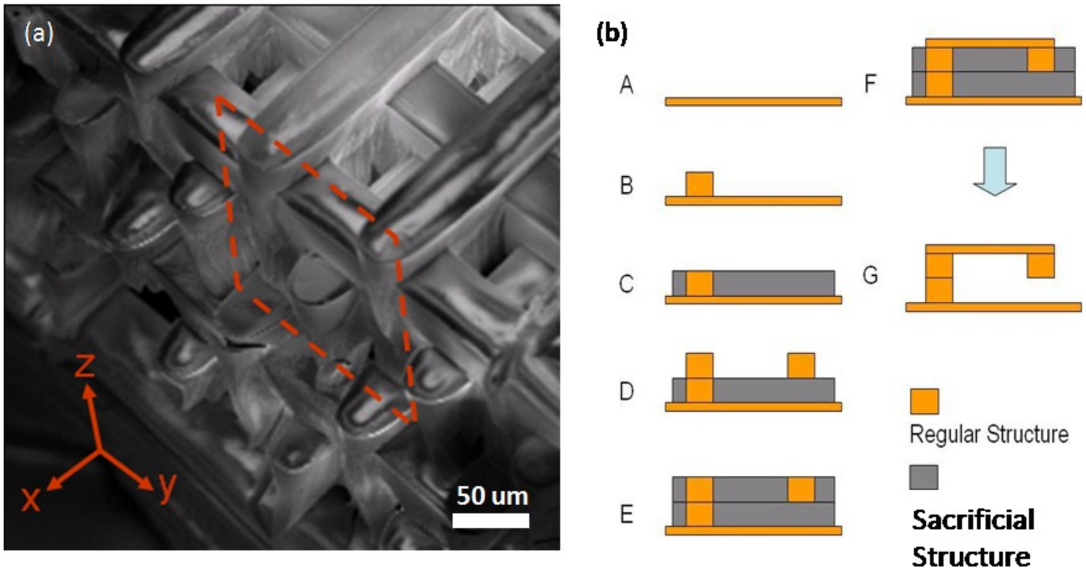

Figure 4.9 A lack of effective sacrificial material limits the micro-geometry that can be built from polymeric materials: (a) A wood-pile structure formed by PEGDA has a resolution of several micrometers at the X-Y plane, but the thickness and resolution along the Z-axis is uncontrollable. (b) Certain geometries, such as the hanging structure, are impossible to build with polymers without using sacrificial materials.

4.2.7a Emulsion-Based Sacrificial Material

As shown in Figure 4.10, the sacrificial material built in our lab is a curable and solvent-removable emulsion. The droplets in the emulsion can be polymerized under certain stimulation, such as light exposure. The application of this sacrificial material can be processed under a normal ambient condition (1 atm, room temperature, for example.) A surfactant keeps the droplets separated before and after curing. The solidified emulsion can be removed by attacking the emulsion with a solvent, which selectively leaves the microstructure intact.

For most organic-based materials for 3D micro-fabrication, the best supportive liquids for the emulsion are perfluorinated liquids, since they are chemically inert and are also extremely immiscible with water and most organic materials without fluorine atoms. In our sacrificial material, Fluorinert FC-70 (3M Corporation), a perfluorinated agent, was used for the supportive liquid. To prepare the surfactant, we synthesized an amphiphilic di-block-copolymer by crosslinking KRYTOX 157 FSH, a fluorinated poly-propylene glycol (Mn = 6500, DuPont), with poly (propylene glycol) acrylate (PPGA, Mn = 400, Sigma-Aldrich). The resulting molecule has a wide fluoro-philic site and a relatively narrow lipo-philic site, preferring to form hydrocarbon droplets in a perfluorinated fluid (FC-70). We prepared the droplet material as following: poly (propylene glycol) diacrylate (PPGDA, Mn = 900, Sigma-Aldrich) plus 2% of photo-initiator Irgacure 819 (Ciba Chemistry) formed a photo-curable liquid. Irgacure 819 induces photo-polymerization at wavelength of a wide range, from UV to blue light. 10 wt% UV absorber 2-(2H-Benzotriazol-2-yl)-6-dodecyl-4-methylphenol (Sigma-Aldrich) was also added to prevent scattering of UV light by the sacrificial material.

The emulsion was made by blending the photo-curable liquid (PCL) in FC-70 with 10wt% of the fluorinated surfactant. The volume ratio of the PCL to the FC-70 /surfactant was (85/15). The surfactant stabilizes closely-packing droplets in FC-70. The same surfactant also keeps the droplets from crosslinking with the micro-structures. The emulsion became rigid upon exposure to ultraviolet (UV) light. Once cured, the acrylate groups at the lipo-philic end of the surfactant is permanently cross-linked with the monomer in the droplet and form a fluorinated shell around the droplet, guaranteeing the droplets stay fluoro-philic and removable by perfluorinated solvents. A cured emulsion was rapidly dissolved by perfluorohexane, a strong perfluorinated solvent to FC-70 but immiscible to most organic materials with no fluorine atom.

The key issue of building a fluorinated emulsion is the synthesis of an effective surfactant. The procedure to synthesize our fluorinated surfactant is briefed below:

4.2.7b Synthesis of the Fluorinated Surfactant

Crude Product Synthesis:

65 g K157H (10 mmoles) was dissolved in 100 ml methoxynonafluorobutane (MPFB). The solution was let reflux at 60 C in a 250 ml three-neck, round-bottom flask under vigorous agitation. The solution was dehydrated over sodium sulfate. Under nitrogen pressure, 8.6 ml oxalyl chloride (100 mmoles) was added slowly to the solution. The solution was let reacting for 12 hrs. The solvent and excess oxalyl chloride was then evaporated for 3 hours under reduced pressure at 70 C. The remained material (chlorinated K157H) was cooled to room temperature before re-dissolved in 100 ml of a mixture of α, α, α-trifluorotoluene and MPFB (50:50 v/v). PPGA (11 mmoles) was then added into the solution under nitrogen pressure. 2.80 ml of triethylamine (20 mmoles) was also added to

absorb hydrochloride and catalyze the reaction. The now cloudy reactants were let reacting for another 12 hrs under vigorous agitation. The triethylamine-hydrochloride salt was removed by simple filtration. The solvent was then removed by evaporation under reduced pressure, and the crude product was left behind.

Purification:

The crude product was dissolved in 100ml of perfluorohexane. The impurities in the solvent (much polar than the goal product) were then removed by mixing the solution with 100 ml of α, α, α-trifluorotoluene in a separation funnel. Upon separated, the bottom phase was the product dissolved in perfluorohexane. Perfluorohexane was removed by evaporation at 60 ˚C under reduced pressure and the final product was obtained.

4.2.7c Effect of Using the Fluorinated, Sacrificial Emulsion

Our experiment showed that the fluorinated, photo-curable emulsion was very effective as a sacrificial material to build polymeric microstructure. Figure 4.11 shows a woodpile structure built by using our sacrificial emulsion. During the DMD-fabrication to build the woodpile, the emulsion was pasted and cured to form a flat surface that covers each structural layer. Notice that the clean-cut underneath the log structures. A control of geometry along the Z-direction was achieved by using our sacrificial material. Under SEM, we found about 0.5% of the surface of the microstructure was attached by the cured micro-droplets. The cause of the incomplete removal of droplets might stem from defects in the emulsion or impurities in the surfactant. We believed that the removability of the cured emulsion can be improved by a slight modification to our recipe of emulsion synthesis. Also shown in Figure 4.11 are the cured droplets under SEM. The pictures show that the surfactant effectively kept the droplets separate upon photo-curing. We also check the distribution of post-cure droplets with dynamic light-scattering (DLS); the results showed negligible change in particle size compared to the droplets in the emulsion before curing (Figure 4.12).

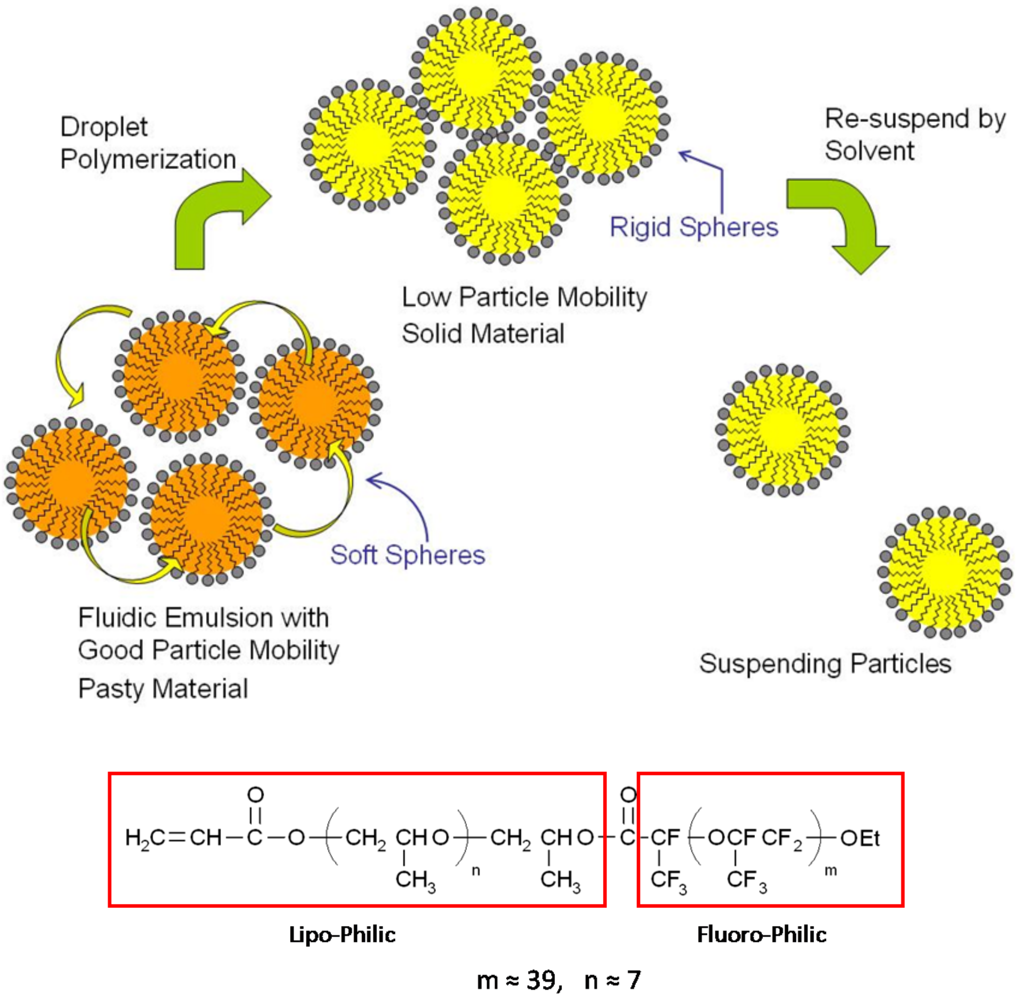

$$H_2C{=}CH-\overset{O}{\overset{\|}{C}}-O-\left(CH_2\underset{CH_3}{\underset{|}{CH}}O\right)_n-CH_2\underset{CH_3}{\underset{|}{CH}}O-\overset{O}{\overset{\|}{C}}-\underset{CF_3}{\underset{|}{CF}}\left(O\underset{CF_3}{\underset{|}{CF}}CF_2\right)_m-OEt$$

Figure 4.10 An emulsion formed by close-packed micro-droplets becomes solid after the photo-curable monomer in the droplets is polymerized. A solvent strong to the suspending liquid can re-suspend the droplets and dissolve the cured emulsion. The droplets are stabilized by a surfactant (marked in red). The surfactant molecule has a small lipo-philic end and a large fluoro-philic end, which prefer forming hydrocarbon droplets in a fluorinated oil, even at very high (lipo/fluoro) volume ratio.

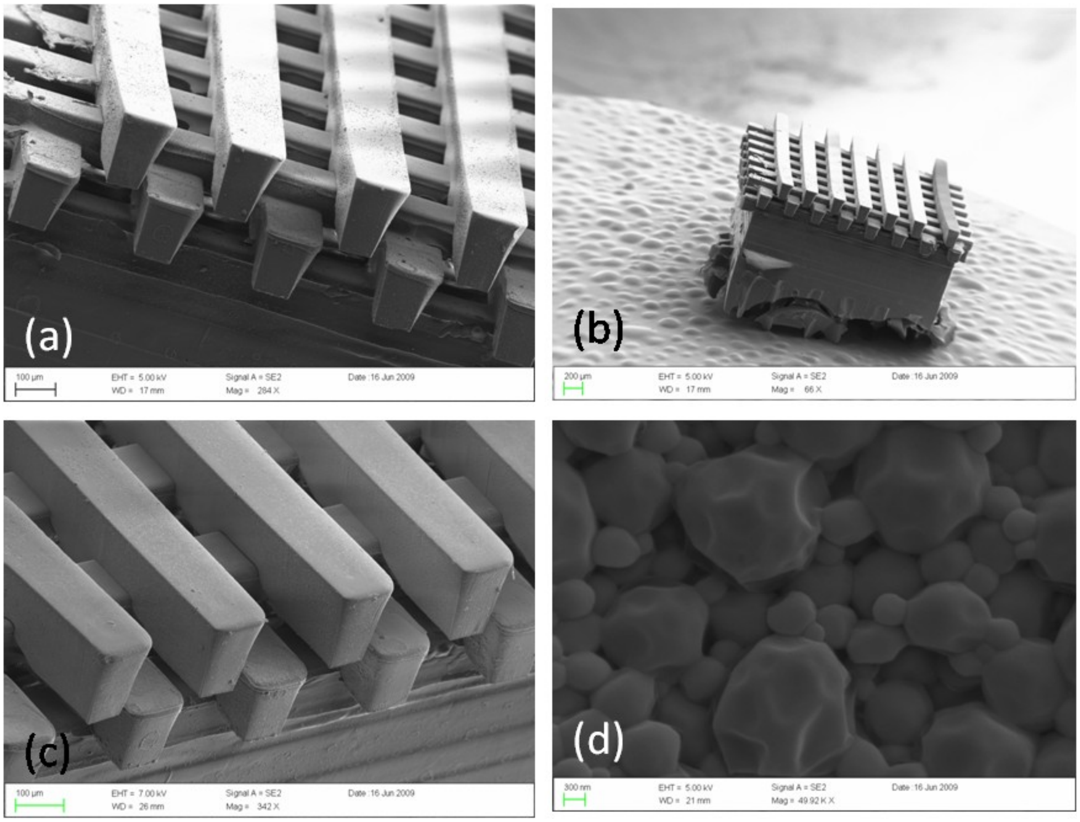

Figure 4.11 By using our fluorinated emulsion, a woodpile structure with controlled resolution along the Z-axis was built (a - c). The logs of the woodpile are about 100 µm wide and 150 µm thick. A piece of cured emulsion was dissolved in perfluorohexane to re-suspend the micro-droplets. SEM images show that the re-suspended droplets were effectively separated. The fluorinated shell formed by the fluorinated surfactant was effective to stabilize the droplets. Picture (d) shows the polyhedral geometries of the cured and re-suspended droplets, which was deformed by the packing force in the high-volume-ratio emulsion.

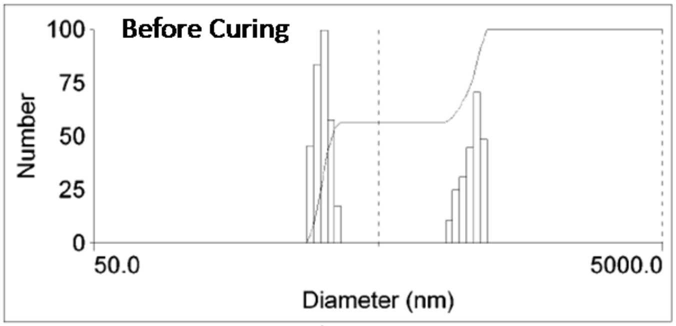

Multimodal Size Distribution

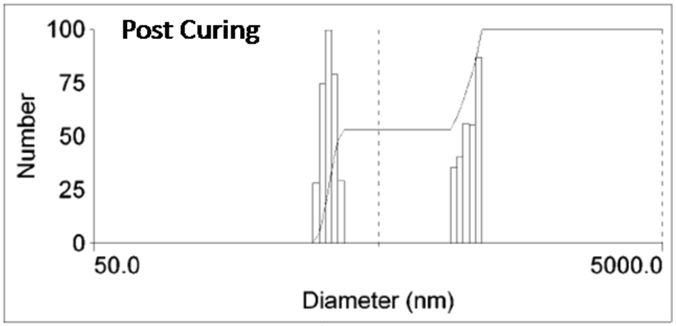

Multimodal Size Distribution

Figure 4.12 Distribution of particle size before (up) and after (down) photo-curing: the sample was an emulsion of closed-packed droplets (85% volume ratio). After curing, the particles were re-suspended in a fluorinated solvent. The size distribution is very similar to the original distribution. The negligible enlargement of particles shows that there was very small cross-linking or clustering among the droplets when photo-curing took place. The surfactant is highly stabilizing, and the cured emulsion can be effectively dissolved in the solvent and thus becomes an effective sacrificial material.

4.3 Fabrication of a Micro-Turbine Heterogeneously Coated by Nanoparticles

4.3.1 Materials to Build a Micro-turbine

We used the following materials to build the micro-turbine. Trimethylolpropane triacrylate (TMPTA), methylmethacrylate (MMA), 2,2,6,6-Tetramethylpiperidine-1-oxyl (TEMPO), hydrogen tetrachloroaurate (HAuCl4), poly(acrylic acid) (PAA, Mw=10,0000), methoxyperfluorobutane (MOPFB), and pentaerythritol tetraacrylate (PETA) were purchased from Sigma-Aldrich. Dipentaerythritol pentaacrylate (DPEPA) was purchased from Sartomer. Irgacure 651 and Tinuvin 234 are given by and purchased from Ciba Chemistry. Polyethyleneimine (PEI, Mw=50,000) was purchased from Polyscience. All the materials were used as received.

We prepared two kinds of material to build the micro-turbine, monomer A and monomer B. The two materials were localized to build the blades of the turbine heterogeneously; one side of the turbine is hydrophilic, the other side of the blade is hydrophobic. The hydrophilic side of the blade has concentrated function groups of carboxylic acid, which allows the attachment of PEI, a chemical to reduce gold from HAuCl4 and from Au nanospheres.

The monomer A is the hydrophilic material; it contains 2wt% of Irgacure 651, 0.02% of TEMPO, 0.1% of Tinuvin 234, in a mixture of MMA and PETA at a 2:3 volume ratio. Irgacure 651 is a photo-initiator which causes cross-linking among the acrylate groups of MMA and PETA; the polymerization process in the monomer takes place when Irgacure 651 is exposed to ultraviolet (UV) light. Once cured, the carboxylic groups from MAA may deprotonate in water, leaving a surface formed by monomer A charged negatively (by the COO- groups). These surface charges are important for the later fabrication process.

Monomer B is a hydrophobic material. It contains 2 wt% of Irgacure 651, 0.02% of TEMPO, 0.1% of Tinuvin 234, in a mixture of TMPTA and DPEPA at a 1:1 volume ratio. Due to the abundance of acrylate groups (TMPTA: 3 groups, DPEPA: 5 groups), the mixture of TMPTA and DPEPA forms a rigid and tough polymer to stabilize the geometry of the micro-turbine. There is no chargeable function group in TMPTA and DPEPA; therefore, a surface formed by monomer B remains neutral in the later post-fabrication process and does not grow Au nanospheres.

The roles of TEMPO and Tinuvin 234 are to modify the geometry resolution. TEMPO is a polymerization quencher, which creates a threshold against the light intensity from a UV image; with a small amount, it may dramatically enhance the contrast of a UV pattern in a monomer. Tinuvin 234, On the other hand, is a UV light absorber. It reduces the curing depth of UV light into the monomer. Adjusting the amount of Tinuvin 234 can tune the depth of 3D structures built by using the DMD system. The absorption by Tinuvin 234 also prevents the UV image for a new layer of structure from "contaminating" the old structures which are below the new one. The amount of TEMPO and Tinuvin 234 were tested to guarantee that the micro-turbine has a resolution below 10 μm.

4.3.2 Fabrication Procedures

The fabrication process is shown in Figure 4.13. The servo-stage was positioned 100 μm below the glass window to start. Monomer A was pumped from the stage-outlet into the gap between the window and the servo-stage.

The power of the UV image was determined to be approximately 10mW/cm^2. The exposure time of the UV pattern for each layer was 25 seconds in order to achieve uniform exposure for the desired thickness of 100 μm. After the first layer was built (B), the stage was repositioned downward 0.5 mm, pulling the structure away from the glass-window. The release was aided by the low surface energy of the fluorinated coating. A mild solvent (isopropanol alcohol, IPA) was pumped into the gap to purge any partially polymerized monomer. IPA was then replaced by a small amount of MOPFB. This volatile fluorinated solvent removes the residual of IPA thus prevents the swelling and deformation of the built structure by IPA. In a different test, we also found that MOPFB is effective in recovering a deformed micro-structure by absorbing the solvent in the structure. Residual of MOPFB was removed by gently purging the structure with weak air flow for 10 seconds. Used solvent was drained from the stage.

To build a secondary structure with hydrophobic character, after purging the material was switched to monomer B, and the stage was moved back to the position it held before the UV exposure step. Another UV exposure was then processed.

In order to build a new layer above the just-formed structure, the stage was repositioned such that the top of the structure was situated 100 μm below the glass-slide. Fresh monomer was pumped again into the 100 μm gap, and the above steps were repeated to create the next layer. The UV-exposure, purging, and monomer switching routines were repeated until the entire micro-turbine was built.

As shown in Figure 4.14, two slightly-different cross-sectional patterns (A and B) were used to construct the micro-turbine with two distinct monomers. As shown in the combination of the two images (colored), pattern A was used to cure monomer A and form a hydrophilic side of the turbine blade (red), which can be later coated with Au nanospheres; pattern B, on the other hand, forms a inert side (blue) of the blades, which does not grow gold nanoparticles. We also created a center hole along the micro-turbine to fit a shaft from a jewel bearing after the fabrication was finished.

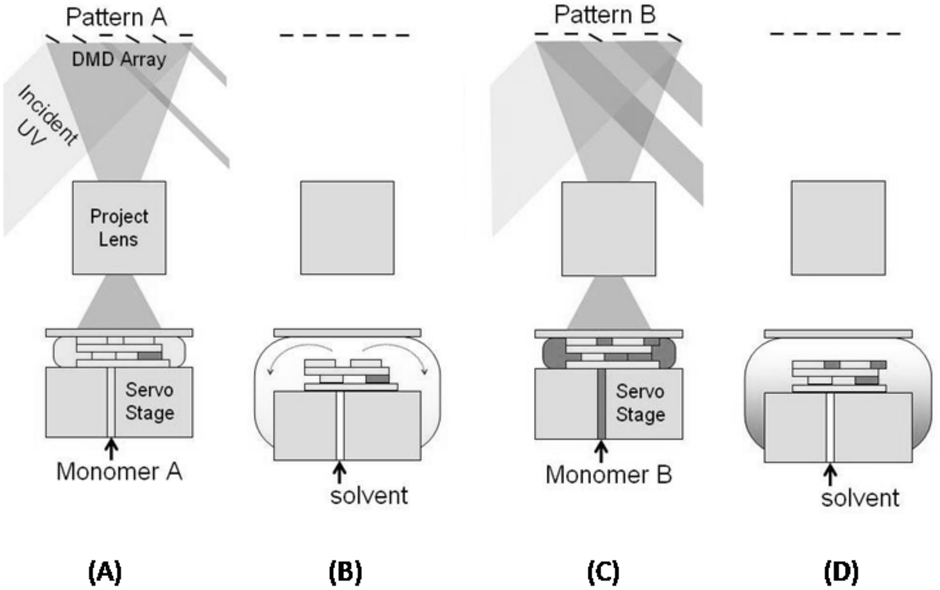

Figure 4.13 The procedure to build a heterogeneous micro-turbine is a double–material feature of DMD fabrication. Two different patterns (A and B) for each side of the blades (hydrophilic or hydrophobic) are switched to cure monomer A and monomer B, which are also switched after each curing process. After one cycle is finished, the servo-stage was moved to a new fabrication position, 100 μm below the previous position. The next layer of micro-turbine was then built through the same procedures.

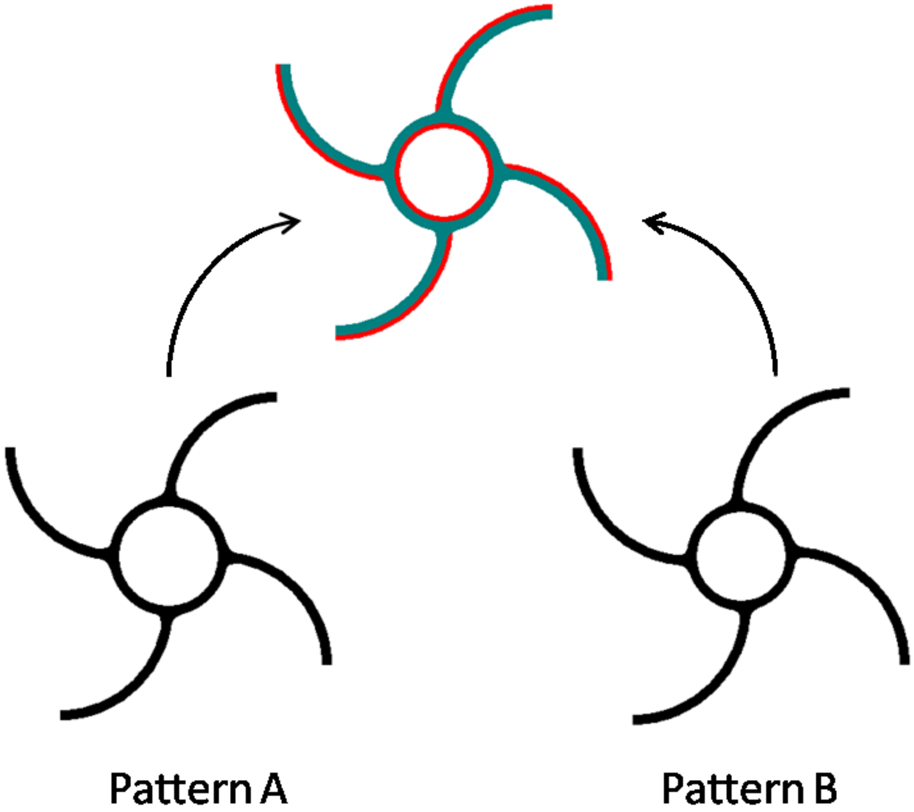

Figure 4.14 The micro-turbine is built by combining two slightly different patterns: pattern A is for the hydrophilic part of the turbine and pattern B is for the hydrophobic part of the turbine. As shown in the combination of the two images, pattern A was used to form a hydrophilic side of the turbine blade (red), which can be later coated with Au nanospheres; pattern B, on the other hand, forms a inert side of the blades (blue), which does not grow gold nanoparticles. The center hole was left to insert the shaft of a jewel bearing.

4.3.3 Post-Fabrication: Coating the Blades with Nanoparticles

Modify the Surface with PEI

To modify the hydrophilic surface of the micro-turbine with nanoparticles, we first coated the surface with a reducing agent for gold: PEI. As shown in Figure 4.15, PEI is a poly-electrolyte which contains concentrated amino function groups (-NH_3). In water, amino groups are protonated and become positively charged (become $-NH_4^+$). The positively charged PEI forms strong electro-static binding with negatively charged chemicals, such as MMA was selectively loaded on one side of the turbine blades.

We load the as-formed micro-turbine into a flask with 20 ml of 1wt% PEI solution in water. The flask was gently shaken for about 30 minutes, then the solution was decanted and the turbine was rinsed with de-ionic (DI) water for 5 minutes.

At this stage, the blades of the micro-turbine were ready to coat nanospheres. However, in our previous study, we found that the coating of nanoparticles was significantly enhanced at particle density if we coat multiple layers of PEI on the surfaces before coating gold. To coat another layer of PEI, we switched the surface charge back to negative charge by coating a layer of PAA on the PEI layer. As shown in the figure, PAA is a poly-electrolyte of concentrated carboxylic acid groups ($-COOH$), which become negatively charged moieties ($-COO^-$) in water. The micro-turbine was loaded into a flask of 20ml, 1% PAA to switch the surface charge. The coating of PAA is the same as PEI in procedure. The coating was switched back to PEI after the PAA coating was finished. Totally, we coated five double layers of the poly-electrolytes (PAA-PEI, with PEI the last layer) before the Au-coating process.

Coat the Surface with Au Nanospheres by Reducing $HAuCl_4$

Also shown in Figure 4.15 is the coating of Au nanospheres on the surfaces with PEI layers. After the coating of PEI, we load the micro-turbine into a flask of 30 ml of 0.1% $\mathrm{HAuCl_4}$ water solution. The flask was gently shaken for 10 minutes under room temperature to allow preliminary reduction of gold on the surface with PEI. The color of the turbine blades turn light-brownish after 5 minutes in the $\mathrm{HAuCl_4}$ solution. After 10 minutes, the flask was transferred to an oil-bath to raise the solution temperature to 85°C. The flask was kept in the oil-bath for another 10 minutes. We observed that the color of the blades turned black after heating for 5 minutes. The appearance of dark color shows that the blade surface was concentrated with nano-scaled particles; the effect of surface plasmonic resonance broadened the wavelength absorption range of Au nanospheres.

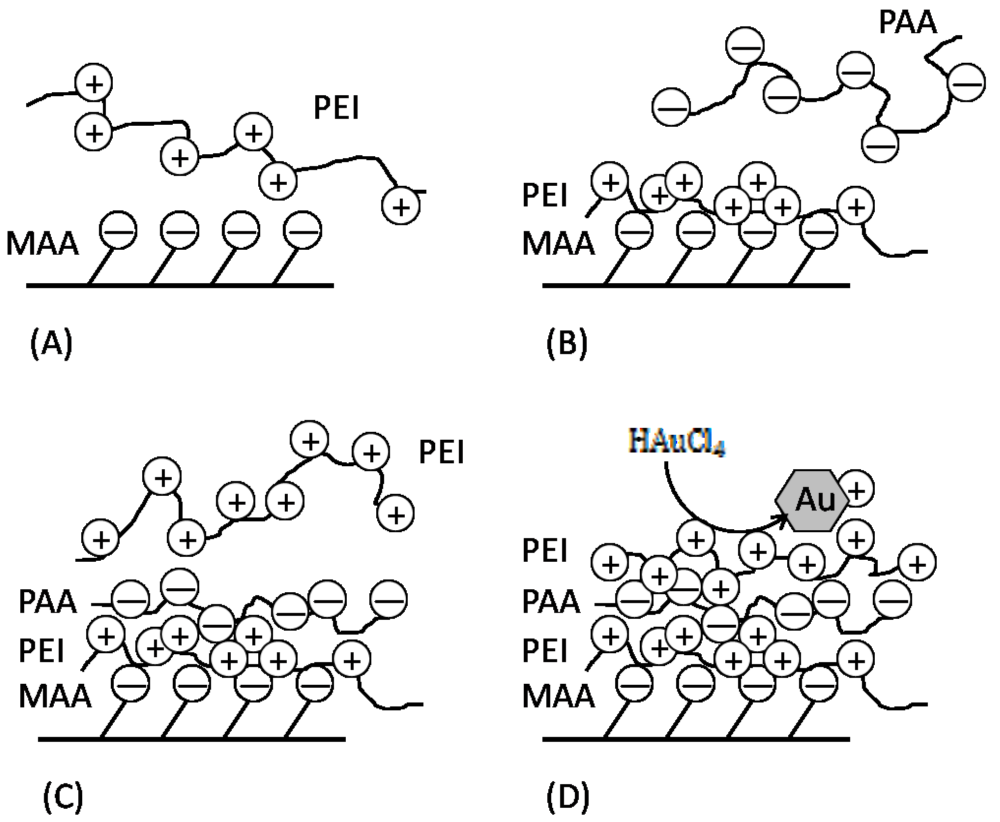

Figure 4.15 (A) The surface of the hydrophilic side of the turbine blades was loaded with MAA, which forms negative surface charges. A PEI molecule bound strongly to MAA through electro-static attachment. (B) The surface charge was switched by coating PAA onto the PEI layer. (C) The surface was switched back to PEI coating and became again positively charged. (D) PEI is a strong reducing agent to reduce gold from HAuCl$_4$ and form Au nanospheres. Coating multiple layers of PEI enhanced the gold reducing effect.

4.4 Experiment: Turning a Micro-turbine by Light

4.4.1 Experiment Setup

Figure 4.16 shows the setup for our experiment. After the fabrication, the micro-turbine was mounted onto a jewel bearing. The jewel bearing include a pin-shaft and two pivot sockets. We inserted the pin-shaft through the center hole of the micro-turbine. The shaft was 400 μm in diameter and has pin-heads at both ends. The turbine with the pin-shaft was mounted between two pivot-sockets, which held point contacts with the pin-heads of the shaft to minimize friction. The insets of Figure 4.4.1 show the dimensions of the fabricated micro-turbine. Notice that the surface of the turbine blade became dark due to the coating of gold nanoparticles. The curvature at the turbine blade was designed for larger area to absorb light.

A turbine holder was used to fix the assembly of jewel bearing in a glass vacuum chamber. We used a vacuum pump (capacity: 30 mTorr) to create an environment of rarified gas for the micro-turbine in the chamber. The pressure of air in the chamber was adjustable by using a needle valve, which was also connected to the chamber. A white light source was installed to send heat to the blade surfaces of the micro-turbine. The movements of the blades were detected by using an optical position sensor, which has a frequency bandwidth of 20 kHz and movement sensitivity below 1 micrometer. The signal from the position sensor was sent to an oscilloscope to record the rotation of the blades.

By using this setup, we recorded the rotation speeds of the micro-turbine under a constant intensity of illumination but different degrees of vacuum. The rotation speed of the turbine was calculated based on the recorded waveform from the oscilloscope:

$$\omega(rpm) = \frac{N_{cycle}}{t} \times 60 \div N_{blade} \tag{4.7}$$

where N_{cycle} is the number of cycles of the signal, t is the time-span of the signal in seconds, and N_{blade}, which equals 4 for this micro-turbine, stands for the number of the turbine blades. The calculated results had the unit of rounds-per-minute (rpm).

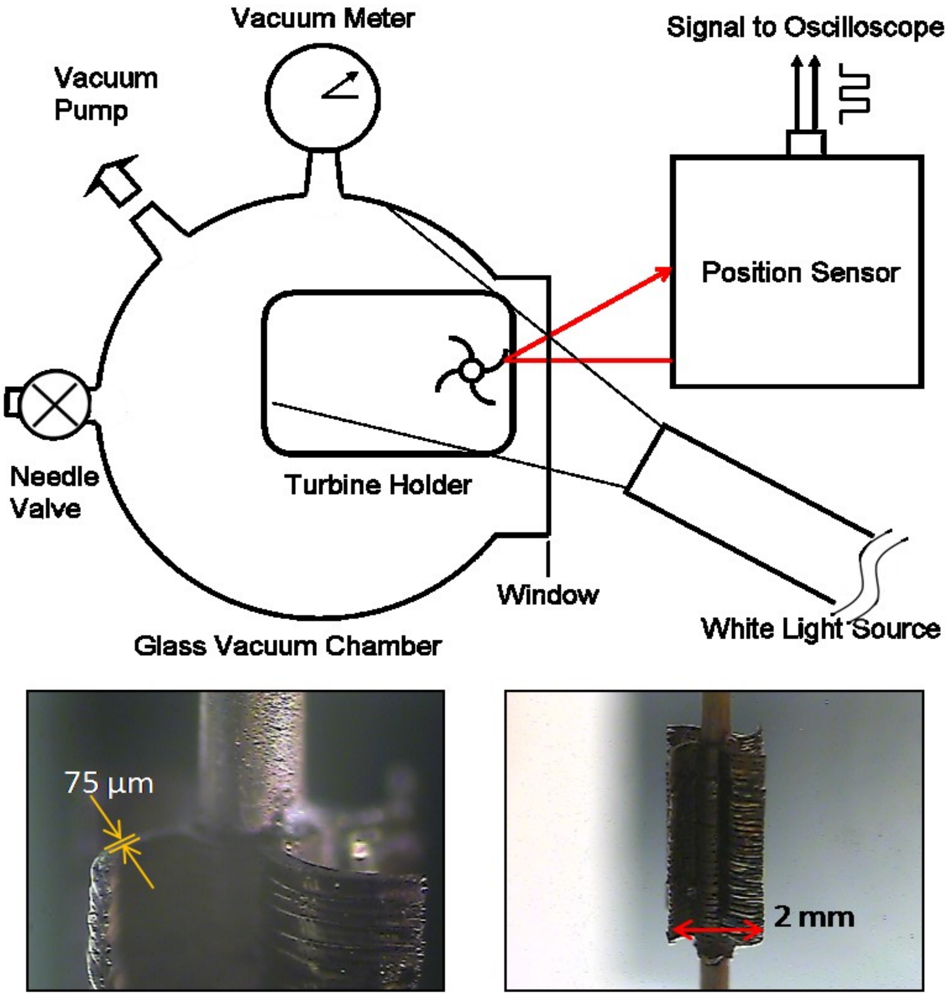

Figure 4.16 The micro-turbine was loaded onto a jewel bearing in a vacuum chamber. The pressure in the chamber was adjusted with a needle valve. A white light source was installed to heat the dark surfaces of the blades of micro-turbine. The movements of the blades were detected by using an optical position sensor, which has frequency bandwidth of 20 kHz. The data of the blade motions under different pressure were recorded.

4.4.2 Experiment Result

Figure 4.17 shows the rotation speed of the micro-turbine under different air pressures. At each pressure we tested the speed of turbine for five times. The illumination by the white light source was shut before each test. After the light source was on, the turbine was let rotating for five seconds before we recorded the waveform in the oscilloscope. We found that five seconds was enough for the turbine to reach a steady speed. Under light exposure at certain degree of vacuum, the micro-turbine rotated with the Au-coated surface (the convex side of the blade) retreating from the source of light. Our record shows that the micro-turbine reached its maximum speed under about 400 mTorr. The maximum turbine speed from our data was about 5800 rpm; the turbine speed dropped when the degree of vacuum was either higher or lower. We also found that the micro-turbine ceased to rotate when air pressure was outside our testing range, from 100 to 700 mTorr, and that the rotation of micro-turbine became on-and–off when the pressure was close to the marginal values. The torque that drove the micro-turbine was too low to overcome the friction at the jewel bearing when the pressure was outside our testing range.

The only changing variable in our tests was air pressure, or the number of gas molecules per unit volume, in the vacuum chamber. Our data shows that gas molecules can either raise the driving torque or reduce it, depends on the density of molecules.

Figure 4.18 shows a different aspect to our experiment data. The figure shows the turbine speed versus the mean free path (MFP) of air molecule. We calculated the mean by using a statistical equation for MFP at room temperature, assuming that the localized heating by incident light was insignificant to the total molecules in the vacuum chamber [16]:

$$MFP\_Air(\mu m) \cong \frac{5\times10^{4}}{pressure\,(mTorr)},\ 20^{\circ}\mathrm{C} \tag{4.8}$$

It was suggested by Albert Einstein [17] that the net force from gas exerted at a plate of double temperatures (one side cold and one side hot) is maximized when the MFP of a surrounding gas becomes comparable to the thickness of the plate. The blade thickness of our micro-turbine was 75 µm. Our calculation showed that the torque at the turbine was maximized when the MFP of air was between 110 and 170µm, roughly twice the thickness of the blades. The above theory matches our data well. However, to gain deeper insights about the optimization of gas pressure for the driving torque, we built a DSMC model to simulate the dynamics of our light-driven micro-turbine.

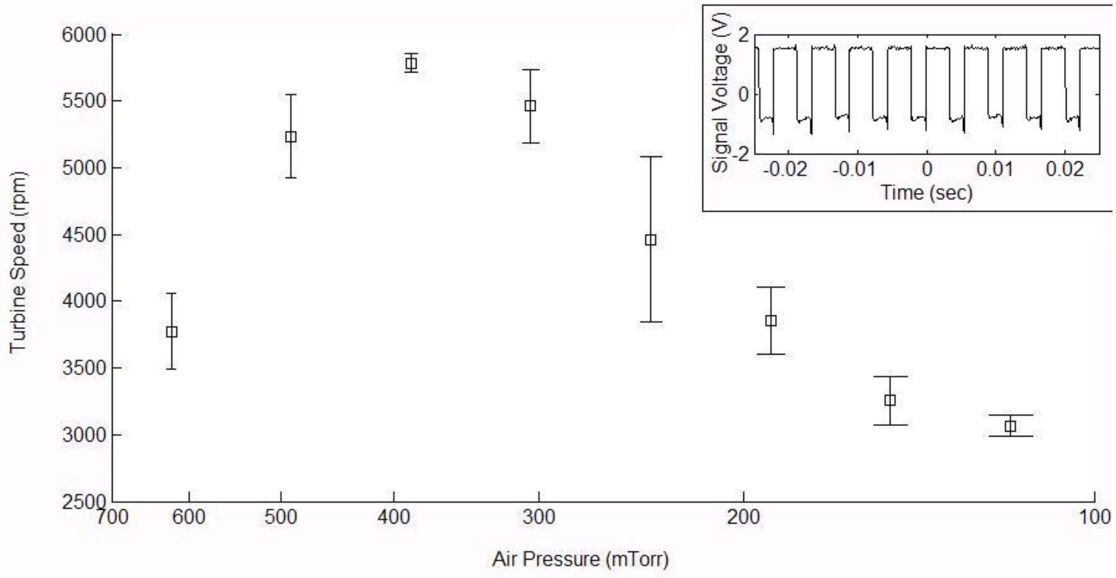

Figure 4.17 The figure shows the turbine speed (rpm) versus air pressure (mTorr) under a constant illumination. The turbine speed was calculated based on the voltage signal from the optical position sensor (inset). The data includes 8 groups of tests; each group includes 5 tests under the same air pressure. The squares and bars in the figure show the mean values and standard deviations of the data from each group. The result shows that the driving torque at the micro-turbine was maximized when the air pressure was around 400 mTorr. The rotation of turbine became unsustainable when the air pressure was outside the data range, 100 to 700 mTorr, at which the driving torque became too low to overcome the friction at the jewel bearing.

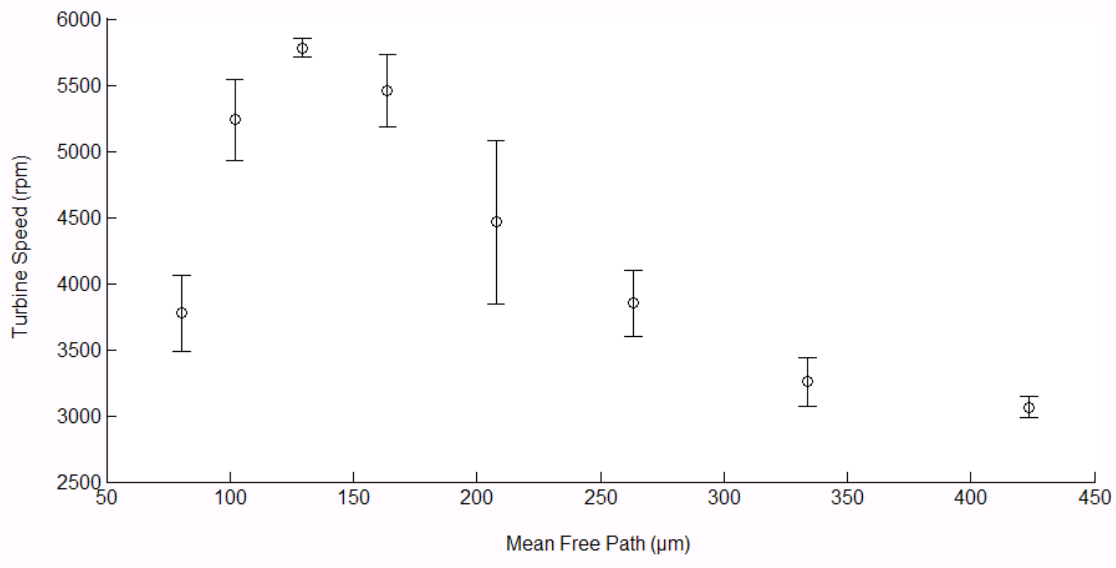

Figure 4.18 As a different aspect to the experiment data, this figure shows the turbine speed (rpm) versus the mean free path (MFP) of air. The values of MFP were calculated based on a statistical equation. The calculation shows that the driving torque was maximized when the MFP of air became roughly twice the thickness of the turbine blades, which was 75 μm.

4.5 DSMC Model to Simulate the Light-Driven Turbine

4.5.1 Gas Dynamics behind the Modeling Program

4.5.1a Newtonian and Statistical Dynamics about Collisions between Hard-Spheres

In this study, the collisions between gas molecules in the simulation space were modeled as the collisions between identical hard spheres; at which the collisions are elastic and frictionless [18]; delay in velocity change of the colliding particles is absent. By using this approximation, the dynamics of collision is simplified and involves exclusively Newtonian mechanics, which demands only the conservation of kinetic-energy and particle momentum. The hard-sphere model is most accurate for the problems of single-atom gas, non-polar molecules, and chemically inert species. One of the good examples is Argon gas. For fluids of other kinds, the approximation by using hard-sphere model also becomes recommendable when the simulated molecule is a rarified gas. A rule of thumb to judge whether the hard-sphere approximation is suitable for the problem is the mean free path (MFP) of a group of simulated molecules [4]. The mean free path (λ) is an expected distance a molecule travels between two collision events:

$$\lambda = \frac{V}{\sqrt{2} N \pi D^2} \tag{4.9}$$

where V is the average particle speed, N is the number density of the particles, and D is the effective diameter of the particle. The value of the mean free path also relates to the gas temperature, which affects the distribution of molecule velocity and thus the average velocity V. Having a long MFP means that two colliding molecules have sufficient time to separate before other molecules could possibly join the collision. A collision only takes place when the distance between two particles equals their effective diameter molecules, therefore a criterion for using hard-sphere model for gas dynamics simulation is:

$$\lambda \gg D \tag{4.10}$$

If the majority of the energy remains kinetic in a collision, a rarified gas can be simulated by using a hard sphere model. For the dynamics of chemically reactive gas, however, hard-sphere simulation should be avoided, for these reactive particles in a real system may either merge each other permanently or split into smaller particles when a collision takes place, transferring kinetic energy into heat or internal energy.

4.5.1b Newtonian Dynamics of a Pair of Colliding Hard-Spheres

A collision problem can be simplified to aid calculation speed. Figure 4.19 shows two identical spheres in an elastic collision. $\overrightarrow{V_1}$ and $\overrightarrow{V_2}$ are the initial sphere velocities. The velocities after the collision, $\overrightarrow{V_1'}$ and $\overrightarrow{V_2'}$ are related to $\overrightarrow{V_1}$ and $\overrightarrow{V_2}$ using energy and momentum conservations:

$$\left|\overrightarrow{V_1}\right|^2 + \left|\overrightarrow{V_2}\right|^2 = \left|\overrightarrow{V_1'}\right|^2 + \left|\overrightarrow{V_2'}\right|^2 \tag{4.11}$$

$$\overrightarrow{V_1} + \overrightarrow{V_2} = \overrightarrow{V_1'} + \overrightarrow{V_2'} \tag{4.12}$$

By introducing the velocity of the center of mass of the two spheres $\overrightarrow{V_{cm}}$ and the relative velocity between the spheres$\overrightarrow{V_r}$, $\overrightarrow{V_1}$ and $\overrightarrow{V_2}$ becomes:

$$\overrightarrow{V_1} = \overrightarrow{V_{cm}} + \overrightarrow{V_r} \tag{4.13}$$

$$\overrightarrow{V_2} = \overrightarrow{V_{cm}} - \overrightarrow{V_r} \tag{4.14}$$

where $\overrightarrow{V_{cm}} = \frac{\overrightarrow{V_1}+\overrightarrow{V_2}}{2}$ and $\overrightarrow{V_r} = \frac{\overrightarrow{V_1}-\overrightarrow{V_2}}{2}$.

By the law of momentum conservation, $\overrightarrow{V_{cm}}$ remains unchanged after collision, so $\overrightarrow{V_1'}$ and $\overrightarrow{V_2'}$ become:

$$\overrightarrow{V_1'} = \overrightarrow{V_{cm}} + \overrightarrow{V_r'} \tag{4.15}$$

$$\overrightarrow{V_2'} = \overrightarrow{V_{cm}} - \overrightarrow{V_r'} \tag{4.16}$$

Note that the law of energy conservation demands $\left|\overrightarrow{V_r'}\right| = \left|\overrightarrow{V_r}\right|$. In a hard sphere model, as shown by Figure 4.19, the spheres are assumed frictionless and the direction of the new velocity is normal to the collision plane, at which the pair have point-contact at the moment of colliding. Given $\overrightarrow{V_1}$ and $\overrightarrow{V_2}$, to solve $\overrightarrow{V_1'}$ and $\overrightarrow{V_2'}$, the unknown variables are reduced to the collision angles $(\theta, \emptyset)$ relative to $\left|\overrightarrow{V_r}\right|$.

One needs to know the relative position of the colliding spheres to calculate the exact $(\theta, \emptyset)$ for each colliding pair. In a simulation that contains many particles, however, calculation of movements for individual particles should be replaced by the use of statistical mechanics to earn simulation speed. A program based on statistical mechanics randomly selects the colliding angles $(\theta, \emptyset)$ based on a theoretical distribution. The theory about selecting $(\theta, \emptyset)$ will be discussed shortly.

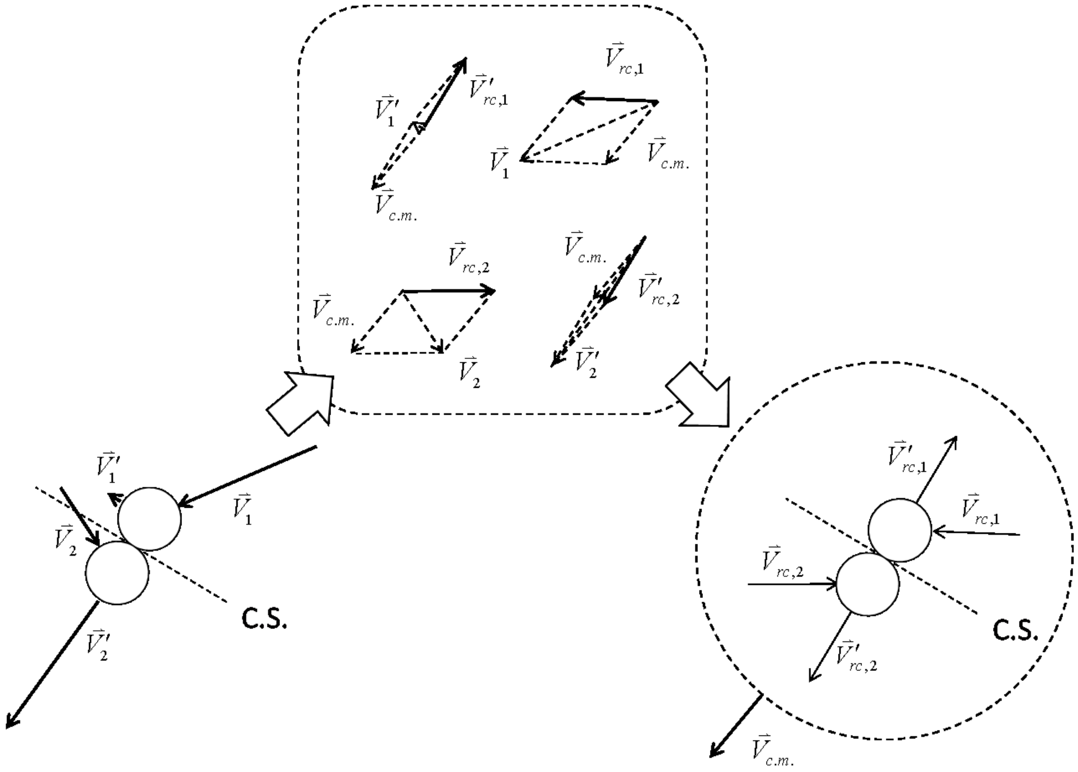

Figure 4.19 The dynamics of collision between two spheres can be simplified using the velocity of the center of mass and relative velocities. The law of energy and momentum conservation demand that $|\vec{V}_{rc,1}| = |\vec{V}_{rc,2}| = |\vec{V}'_{rc,1}| = |\vec{V}'_{rc,2}| = V_{rc}$, $\vec{V}_{rc,1} = -\vec{V}_{rc,2}$, and $\vec{V}'_{rc,1} = -\vec{V}'_{rc,2}$. The post-collision relative velocities, $\vec{V}'_{rc,1}$ and $\vec{V}'_{rc,2}$, are perpendicular to the surface of collision. Given the initial sphere velocities, the remained unknown variables are the collision angles $(\theta, \emptyset)$.

4.5.1c Probability Distribution of Collision Angles

A collision takes place when the centers of two spheres are one diameter apart. Therefore, as illustrated in Figure 4.20, a pair of colliding spheres of diameter D must have their centers both located in a collision cylinder, which is parallel to the relative velocities and has a diameter 2D. The axis of the cylinder also passes one of the spheres center. The distribution of the collision angles $P(\theta, \emptyset)$ is a function of probability density, which means that the probability for the collision angles to fall at an infinitely small range $d\theta \cdot d\varphi$ is $P(\theta, \emptyset)d\theta d\emptyset$. $P(\theta, \emptyset)$ is normalized such that an integral of $P(\theta, \emptyset)$ over the whole possible values for $(\theta, \emptyset)$ equals one:

$$\int_0^{\pi/2}\int_0^{2\pi} d\theta d\varphi\, P(\theta, \emptyset) = 1 \tag{4.17}$$

To calculate $P(\theta, \emptyset)$, we start by using a fact that the possible incident route of sphere 2 to sphere 1 is uniformly distributed through the cylinder. Therefore, the central positions for all the possible sphere 2 is uniformly distributes over the cross-section of the cylinder. Thus:

$$P(r, \emptyset)drd\emptyset = \frac{rdrd\emptyset}{\pi D^2} \tag{4.18}$$

The notation dr and $d\emptyset$ at both sides of the equations reminds that the function P is a probability density. Because $\emptyset$ is uniformly distributed across $[0, 2\pi]$, we know:

$$P(\emptyset)d\emptyset = \frac{1}{2\pi} \cdot d\emptyset \tag{4.19}$$

By integrating $P(r, \emptyset)$ across $\emptyset = 0\ to\ 2\pi$, we get:

$$P(r)dr = \frac{2rdr}{D^2} \tag{4.20}$$

The probability densities $P(r)$ and $P(\theta)$ are related by $P(r)dr = P(\theta)d\theta$. By using $r = D\sin(\theta)$ and $dr = D\cos(\theta)d\theta$, the probability distribution for the collision angle θ becomes:

$$P(\theta)d\theta = \sin(2\theta)\, d\theta \tag{4.21}$$

Once the probability density of $(\theta, \emptyset)$ is known, the post-collision velocities can be selected using a random generator that simulate the theoretical distribution. The design of this random generator will be discussed shortly.

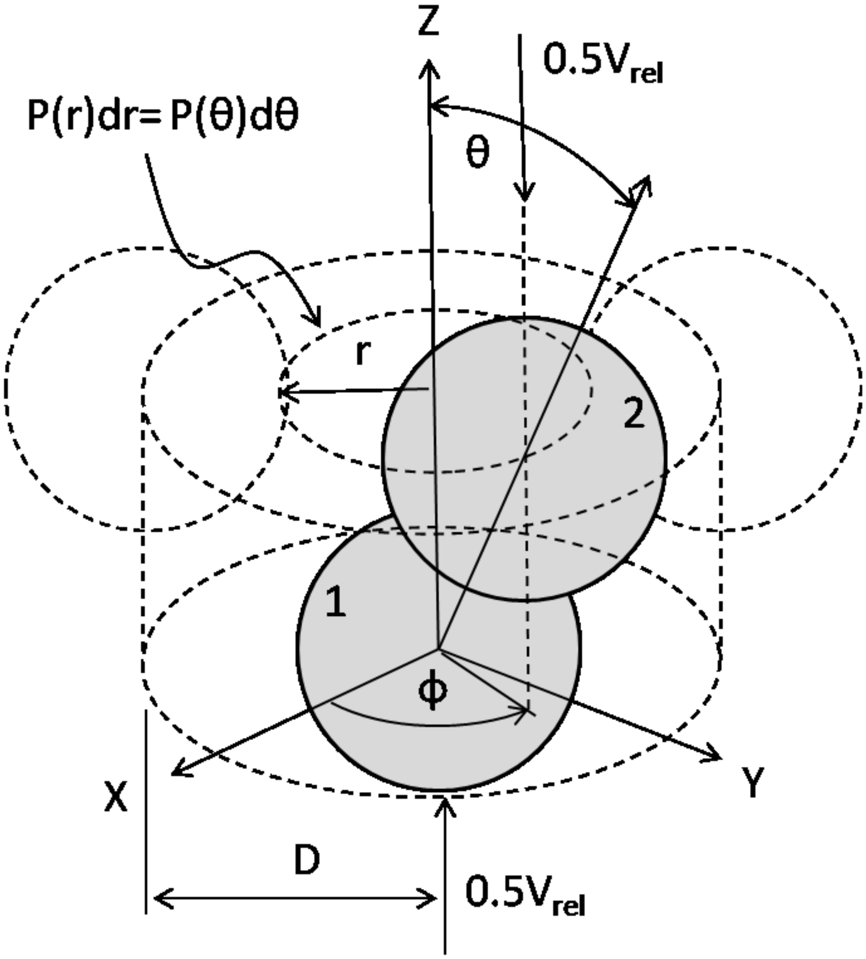

Figure 4.20 A collision happens when the centers of a random pair of spheres, numbered 1 and 2, are both in a cylinder of diameter 2D. The cylinder axis passes the center of sphere 1 and is parallel to the relative velocity of the spheres. D is the diameter of the spheres. The distribution of collision angles $(\theta, \emptyset)$ is related to that of $(r, \emptyset)$, which is uniformly distributed over the cross-section of the cylinder.

4.5.1d Interaction of Particle with Boundaries in a Simulation Space

This study includes three kinds of boundaries conditions for the simulated particles. One is specular boundary, the other is thermal-wall, and the last one is periodic boundary condition.

Specular Boundary

A specular boundary reflects an incident particle specularly and renews the particle velocity $\vec{V}_{inc}$ as follow:

$$\vec{V}_{inc}' = \vec{V}_{inc} - 2\left(\hat{n} \cdot \vec{V}_{inc}\right) \hat{n} \tag{4.22}$$

where $\hat{n}$ is the unitary normal vector of the boundary surface. This equation gives a mirror reflection to the incident particle. The speed and thus the kinetic energy of the incident particle are unchanged after the reflection; there is no heat-transfer or friction between a simulated particle and a specular boundary.

Thermal-Wall Boundary

A thermal-wall is an isothermal boundary condition. In the DSMC method, the temperature of a particle is calculated by its velocity, so the thermal wall boundary reset the velocity of particles based on the speed distribution at certain temperature. Upon the arrival of a particle, the thermal wall randomly assigns a new velocity to the particle according to the biased Maxwell-Boltzmann distribution [19]:

$$duP(u) = du\sqrt{\frac{m}{2\pi kT}}e^{-\frac{mu^2}{2kT}} \tag{4.23}$$

$$dvP(v) = dv\frac{m}{kT}ve^{-\frac{mv^2}{2kT}} \quad (4.24)$$

$$dwP(w) = dw\sqrt{\frac{m}{2\pi kT}}e^{-\frac{mw^2}{2kT}} \quad (4.25)$$

The particle velocity $(u,\ v,\ w)$ is relative to the surface, v is parallel to the surface normal, k is the Boltzmann constant, T is the temperature of the thermal-wall boundary, and m is the real mass of the gas molecule. Figure 4.21 shows the possible positions of a particle reflected from a thermal wall. The wall is placed at $y = 0$. The particle came from $y > 0$ at a speed of arbitrary unit. The new velocity for the particle is biased and $v_y > 0$. On the other hand, v_x and v_z, follows Gaussian's normal distribution across $x = \pm\infty$.

A thermal-wall is also equivalent to a reservoir of particles. As shown by Figure 4.22, a particle hits the thermal-wall can be considered leaving the boundary, and its reflection can be considered a new particle entering the simulation space.

In this study, thermal walls were used to simulate the heating and cooling surfaces for the particles; a large thermal wall was also used to simulate an isothermal reservoir, which is assumed far enough from the micro-turbine.

Periodic Boundary

The system periodicity can be used to reduce calculation efforts. To simulate a 4-bladed turbine, the simulation space only needs to cover one quarter of the turbine cross-section if periodic boundaries are used. Each periodic boundary is paired with one counterpart boundary, which defines the opposite side of the simulation space. Each of the periodic boundaries has a unique coordinate system based on its surface normal vector. As illustrated in Figure 4.23, a particle hitting a periodic boundary is switched to the counterpart boundary, and its new position and velocity relative to the counterpart boundary are the same as their original values relative to the previous boundary.

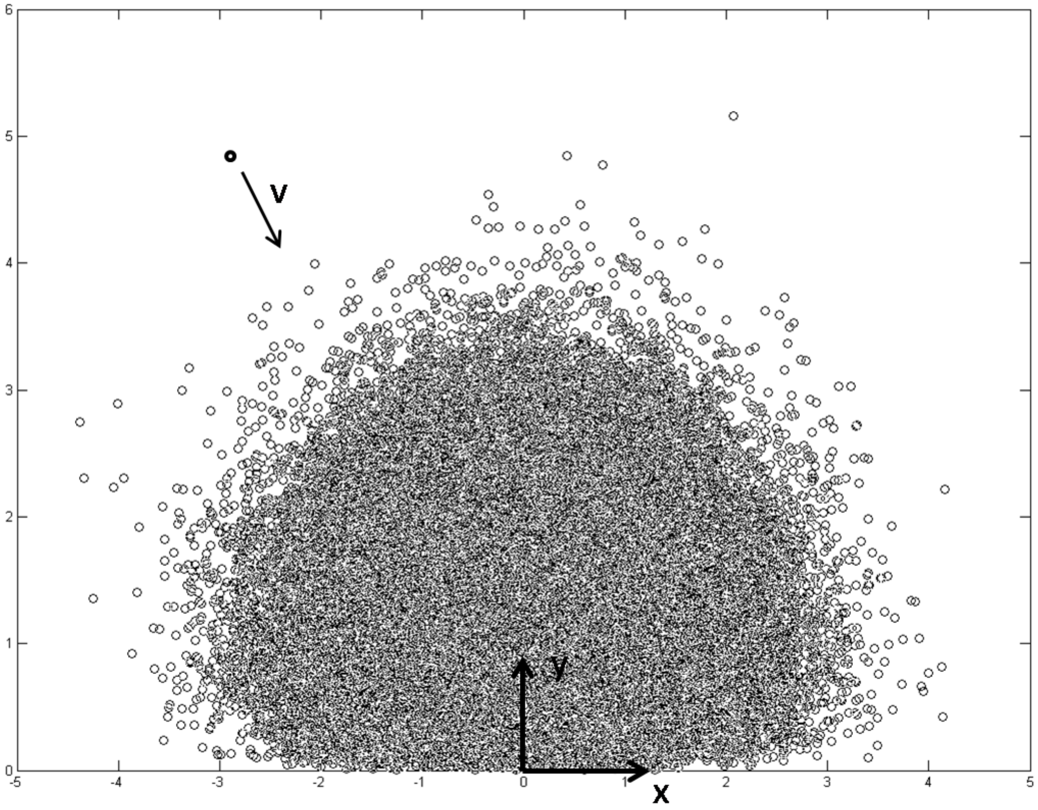

Figure 4.21 An incident particle has its velocity reset at a thermal wall at y=0. The new velocity for the particle follows the biased Maxwellian distribution; v_y is positive, while v_x and v_z follows Gaussian's normal distribution over ±∞. The multiple plots show the possible positions of the incident particle an arbitrary moment after the collision.

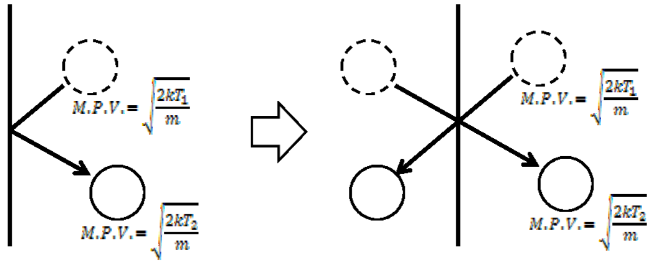

Figure 4.22 A thermal-wall boundary is also equivalent to an isothermal reservoir. A molecule hitting the thermal wall can be considered leaving it, and its reflection can be considered as a new molecule entering the simulation space.

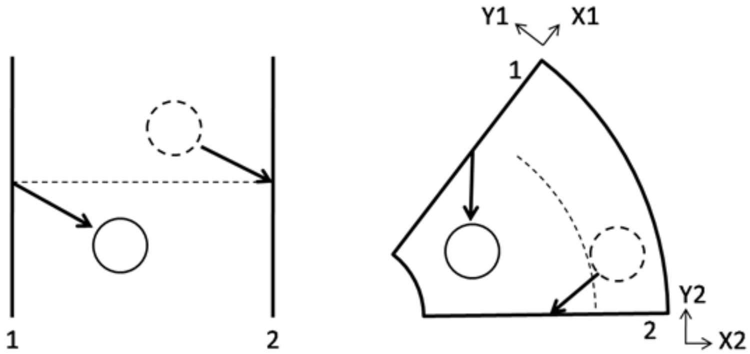

Figure 4.23 A periodic boundary (2) transfers an incident particle to its counterpart (1). The particle is assigned a new velocity and position which have the same relative values to the boundaries.

4.5.2 Random Generator to Create Theoretical Distributions of Variables

4.5.2a Uniform Random Generator

The DSMC program uses random numbers to create system variables, and the distributions of these variables have to match theoretical distributions. Most of the programming languages, such as MATLAB, VISUAL BASIC++, or VISUAL C++, have the functions to give a series of random number $\Re$, uniformly distributed between 0 and 1:

$$P(\Re)d\Re = 1 \cdot d\Re \tag{4.26}$$

Our goal is to use this uniform random generator to match a non-uniform distribution, $P(\alpha)d\alpha$, where the value of α is limited in the range $[\alpha 1,\ \alpha 2\,]$. One of the good methods is to firstly let $d\Re/d\alpha = C' + C \cdot P(\alpha)$, relating $\Re$ to α. C' and C are constants. The probability equation of $\Re$ thus becomes:

$$\left(\frac{d\Re}{d\alpha}\right) \cdot d\alpha = \left(C' + C \cdot P(\alpha)\right) d\alpha \tag{4.27}$$

By integrating at both sides of the equation, we get:

$$\Re = C'\alpha + C \int d\alpha P(\alpha) \tag{4.28}$$

Let $\wp(\alpha) = \int d\alpha P(\alpha)$, C' and C are calculated to match the value range of $\Re$:

$$C'\alpha 1 + C \cdot \wp(\alpha 1) = 0 \tag{4.29}$$

$$C'\alpha 2 + C \cdot \wp(\alpha 2) = 1 \tag{4.30}$$

Therefore, to create a group of α that match the theoretical distribution $P(\alpha)$, we first use the random generator to create a group of uniformly distributed $\mathfrak{R}$ between 0 and 1, then convert these random number to α by using an reverse equation:

$$\alpha = \alpha(\mathfrak{R}) \tag{4.31}$$

For example, the collision angle θ has the theoretical distribution$P(\theta)d\theta = \sin(2\theta)\, d\theta$, so the $\theta\ is$ related to $\mathfrak{R}$ by:

$$\mathfrak{R} = 0 \cdot \alpha + 1 \cdot sin^2(\theta) = sin^2(\theta) \tag{4.32}$$

By calculating the inverse function $\theta(\mathfrak{R})$, we get:

$$\theta = arcsin\left(\sqrt{1 - \mathfrak{R}}\right) = \arcsin\left(\sqrt{\mathfrak{R}}\right) \tag{4.33}$$

As another example, match a biased Maxwell-Boltzmann distribution:

$$P(u)du = \frac{m}{kT} u e^{-\frac{mu^2}{2kT}} du \tag{4.34}$$

Using $\mathfrak{R} = C'\alpha + C \int d\alpha P(\alpha)$ and $u \in [0, \infty)$, we get:

$$\mathfrak{R} = e^{-mu^2/2kT} \tag{4.35}$$

and the theoretically distributed u is calculated by:

$$u = \sqrt{-\frac{2kT}{m} ln(\Re)} \tag{4.36}$$

4.5.2b Gaussian Random Generator

Gaussian random generators are also commonly provided by programming languages. The Gaussian random number $\Re_G$ has the probability density as follow:

$$P(\Re_G)d\Re_G = \frac{1}{\sigma\sqrt{2\pi}} e^{-\frac{(\Re-\mu)^2}{2\sigma^2}} d\Re_G \tag{4.37}$$

To match a probability function that is a Gaussian distribution, it is more efficient to use a Gaussian random generator instead of the uniform random generator. For example, to match the distribution of the tangential particle velocity reflected by a thermal wall boundary:

$$P(u)du = \sqrt{\frac{m}{2\pi kT}} e^{-\frac{mu^2}{2kT}} du \tag{4.38}$$

The program generates u simply by using:

$$u = \sqrt{\frac{kT}{m}} \Re_G \tag{4.39}$$

4.5.2c Examples of Random Generators

The distribution of post-thermal wall velocity in Figure 4.21 was generated using both uniform and Gaussian random generators. As another example, Figure 4.24 shows the distribution of relative, post-collision velocities of a pair of colliding spheres. The distributions of post-collision velocities are slightly biased toward the opposite of the incident direction of each particle. Note that the distributions are similar to a uniform distribution over a hemisphere. A couple decades ago, instead of using the rigorous calculation, it was acceptable to use a hemispherical, uniform distribution to save computational efforts [5], i.e., $P(\theta)d\theta = \sin(\theta)\, d\theta$ and $P(\emptyset)d\emptyset = \frac{1}{2\pi} \cdot d\emptyset$; without doing so, one has to transfer the relative, post-collision velocities to the absolute velocities relative to the simulation space. This approximation has become unnecessary due to the advance of computer technologies. For modeling accuracy, we used the rigorous approach based on $P(\theta)d\theta = \sin(2\theta)\, d\theta$ and $P(\emptyset)d\emptyset = \frac{1}{2\pi} \cdot d\emptyset$.

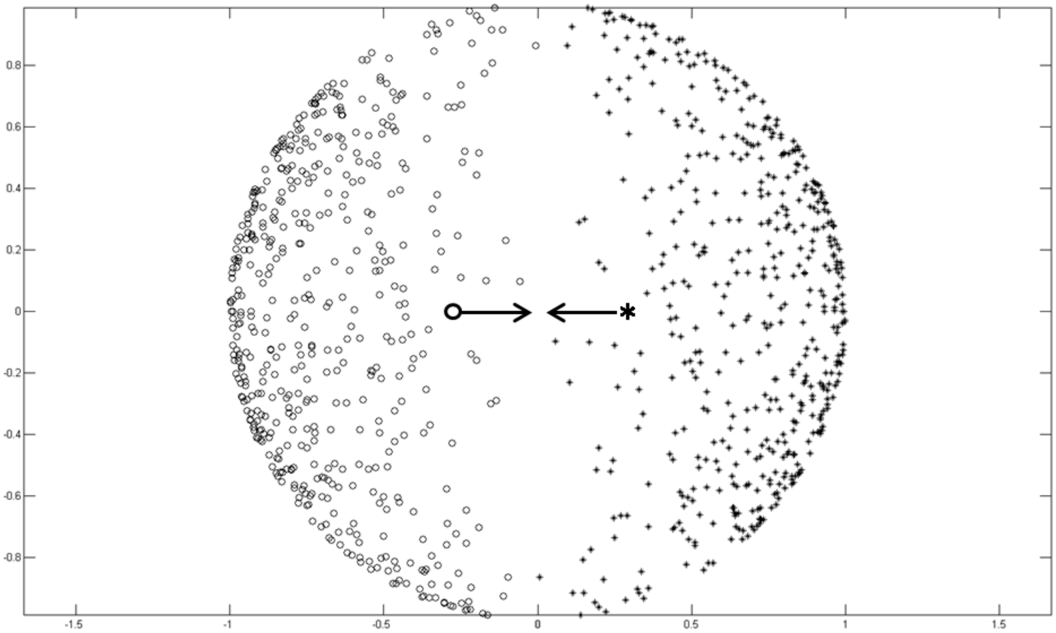

Figure 4.24 500 post-collision positions of a pair of colliding particles are randomly generated according to the theoretical distributions: $P(\theta)d\theta = \sin(2\theta)\,d\theta$ and $P(\emptyset)d\emptyset = \frac{1}{2\pi} \cdot d\emptyset$. The arrows show the direction of initial velocities of the collision pair. The velocity of the center of mass is 0. The units for the initial velocities and the time after collision are arbitrary. The plots show that the distribution of the post-collision movement of particles is angularly biased, toward $\theta = 0 \; and \; \pi$.

4.5.3 Generation of Subspaces: Cells and Sampling Cells

4.5.3a DSMC Cells

To gain computing efficiency, we want to avoid the direct calculations of relative positions for pairs of the N simulated particles, which will be totally $N(N-1)/2$ pairs. One way to bypass the direct distance calculation is to generate particle collisions using Monte Carlo programming, which randomly selected particles as collision pairs to collide with one another. The problem is that the particle pairs of smaller distances must have the higher chance to collide. But how do we know which pairs are close particles without calculating their relative positions? A solution used by the author of DSMC is to group the particles into a number of different subspaces or "cells" [19]; each of the cells occupies a small space in the whole simulation domain. Figure 4.25 shows an example of the cells in DSMC simulation. The particles that fall into the same cell are considered close particles, and a number of colliding pairs are chosen from each cell to perform collisions. The theory and program for the selection of collision pairs will be discussed shortly.

The shape of DSMC cells is not limited to the squares in Figure 4.25, and their volumes can be different from one another [20]. The proper geometry of a cell depends on the gradient of simulated properties, such as temperature or pressure, around the region where the cell is located. A region of sharper gradient should be divided into smaller cells, for the chance of particles collisions is more sensitive to positions in this area. Another guideline to the size of cells is the mean free path (MFP) of the particles. For statistically a particle will collide with another particle in a traveled distance of MFP, the cell size should be larger than the MFP in the region where the cell locates, else the particle collisions between neighboring cells, which is neglected in the DSMC method, may affect the accuracy of the simulation results. A rule of thumb provided by authors elsewhere is that the cell dimension should be smaller than 1/5 of the MFP in a local region.

4.5.3b DSMC Sampling Cells

The cells in a DSMC model are an analogy to the meshing of the finite element method (FEM), which is widely used to simulate solids or continuous fluids [21]. The cells in a DSMC simulation are used to calculate the local, average properties, such as temperature, velocity, or pressure. To organize cells in different regions, sampling cells are generated. In our simulation, most of the sampling cells, except the ones at the simulation boundaries, contain 9 cells. The values calculated in the sampling cells are the final results from DSMC simulation. Figure 4.26 shows the simulation results calculated using sampling cells, which collected values from the cells in Figure 4.25. The result shows the average temperatures and also particle-velocities in different areas.

4.5.3c Calculation of Temperature

The calculations for most of the cell properties are simple, except for the temperature. Our DSMC simulation is a hard-spheres model, where the temperature is a function to only the speeds of particles:

$$T = T(v) \tag{4.40}$$

To calculate the temperature among a group of particles, we reverse the process of estimating particle speed from the temperature:

$$T = \frac{2}{3k}\langle K \rangle \tag{4.41}$$

where k is the Boltzmann constant and $\langle K \rangle$ is the average thermal-kinetic energy in the group of particles. Thermal-kinetic energy is different from kinetic energy. Thermal kinetic energy is calculated from the particle velocities relative to the mass center of the particles:

$$K = \frac{1}{2}m\left\langle |v-\mu|^2 \right\rangle \tag{4.42}$$

where μ is the velocity of the mass center, and μ equals the average velocity of the particle group. The previous equation thus becomes:

$$\langle K \rangle = \frac{1}{2}m\left\langle (v_x - \langle v_x \rangle)^2 + (v_y - \langle v_y \rangle)^2 + (v_z - \langle v_z \rangle)^2 \right\rangle \tag{4.43}$$

To enhance the computing speed, the above equation can be rearranged based on a statistics formula [5]:

$$\left\langle (\alpha - \langle \alpha \rangle)^2 \right\rangle = \langle \alpha^2 \rangle - \langle \alpha \rangle^2 \tag{4.44}$$

Accordingly, the equation of thermal kinetic energy becomes:

$$\langle K \rangle = \frac{1}{2} m \left(\langle v_x^2 \rangle + \langle v_y^2 \rangle + \langle v_z^2 \rangle - \langle v_x \rangle^2 - \langle v_y \rangle^2 - \langle v_z \rangle^2 \right) \tag{4.45}$$

Therefore, in a sampling cell of N simulated particles, the temperature is:

$$T = \frac{2}{3k} \langle K \rangle = \frac{m}{3k} \left[\frac{\sum_{i=1}^{N} \left(v_x^2 + v_y^2 + v_z^2 \right)}{N} - \left(\frac{\sum_{i=1}^{N} v_x}{N} \right)^2 - \left(\frac{\sum_{i=1}^{N} v_y}{N} \right)^2 - \left(\frac{\sum_{i=1}^{N} v_z}{N} \right)^2 \right] \tag{4.46}$$

The calculation of the temperature followed the above equation.

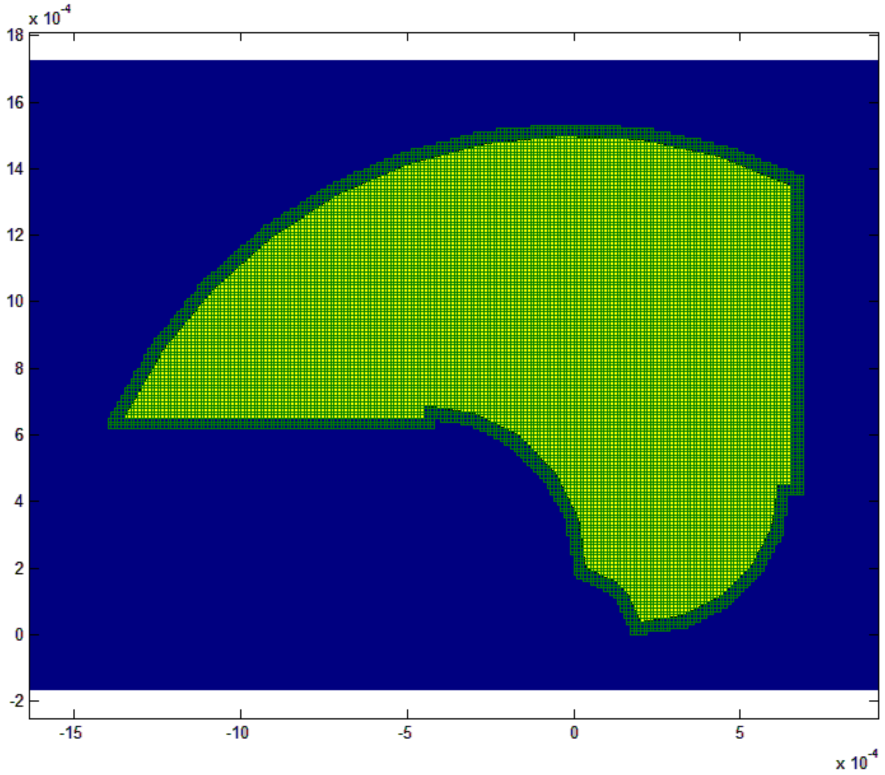

Figure 4.25 The simulation space is divided by multiple cells, which define close particles. Collisions are selected among each cell based on a selection rule. The cells are also used to calculate spatial properties of the model, such as the temperature or velocity fields. Sampling cells are used to collect values from a number of cells for average properties. The size of a sampling cell should be smaller than its local mean free path to guarantee the accuracy of the DSMC model.

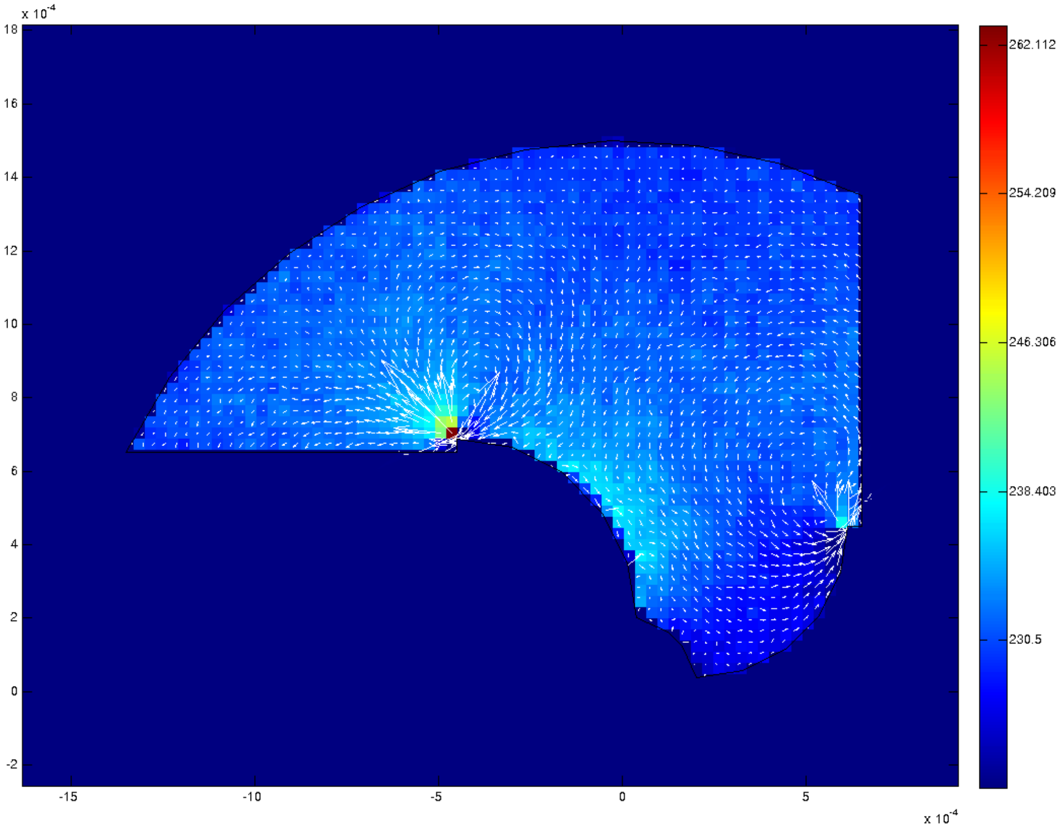

Figure 4.26 The distributions of temperature and velocity are calculated by using sampling cells, which collect values from the cells of figure 4.25.

4.5.4 Selection of Colliding Pairs

4.5.4a Select a Colliding Pair

In a DSMC model, if one collision will take place in a cell, every pair of particles becomes candidates for the collision, regardless of their positions in the cell. However, the probability for a pair of particles (i, j) to collide is proportional to their relative speed:

$$P_{coll}(i,j) = \frac{|\vec{v}_i - \vec{v}_j|}{\sum_{m=1}^{N}\sum_{n=1}^{m-1}|\vec{v}_m - \vec{v}_n|} \tag{4.47}$$

where N is the number of particles in the cell. The double summation term in this equation is computationally expensive; it is preferable to bypass the direct calculation of relative speeds but meanwhile satisfy the above equation. Following the method given by [5], we used a five-step procedure to select colliding pairs:

Prepare a maximum speed v_{max} for each cell. v_{max} is assumed higher than any relative speed in the cell.

(1) A pair of particles is randomly selected from the cell.
(2) Calculate the particles' relative speed $|\vec{v}_i - \vec{v}_j|$.
(3) Generate a uniform random number R between 0 and 1. The selected particles will collide if $|\vec{v}_i - \vec{v}_j| / v_{\max} > R$.
(4) If $|\vec{v}_i - \vec{v}_j| > v_{\max}$, let $v_{\max} = |\vec{v}_i - \vec{v}_j|$

This method matches the previous function exactly, because:

$$P_{coll}(i,j) = \frac{|\vec{v}_i - \vec{v}_j| / v_{\max} \times 2/N(N-1)}{\sum_{m=1}^{N}\sum_{n=1}^{m-1}\left[|\vec{v}_m - \vec{v}_n| / v_{\max} \times 2/N(N-1)\right]} = \frac{|\vec{v}_i - \vec{v}_j|}{\sum_{m=1}^{N}\sum_{n=1}^{m-1}|\vec{v}_m - \vec{v}_n|} \tag{4.48}$$

Note that an overly estimated v_{max} can still satisfy the probability equation.

4.5.4b Number of Colliding Pairs in a Cell

The theoretical number of collision during a period of time is calculated by using a simple model. Given that a particle of diameter D is moving at a speed of v in a space of N particles and volume V. The volume that this particle sweeps across forms a "collision cylinder" of a diameter of 2D; other particles which have their centers located in this cylinder collide with this particle. The trajectory of the moving particle bends after each collision, and the volume the particle passed by is actually a zigzag cylinder; however, we consider the volume equals a straight cylinder for simplicity. The number of collisions take place along the particle's moving during a time equals the particle number in the collision cylinder over time t:

$$Collision\# = \frac{N}{V}\pi D^2 vt \tag{4.49}$$

This equation is based on an assumption that the other particles are stationary. In a cell where every particle is moving, this model seems unfit. However, if we replace v with average relative speed $\langle v_r \rangle$ among the particles, the equation can be replaced by the average number of collisions for each of the particles during the period t:

$$\langle Collision\# \rangle = \frac{N}{V}\pi D^2 \langle v_r \rangle t \tag{4.50}$$

The average number of collisions in the cells during time t is:

$$N_{coll} = \langle Collision\# \rangle \times \frac{N}{2} = \frac{N^2}{2V}\pi D^2 \langle v_r \rangle t \tag{4.51}$$

The "2" in the denominator takes care of the double count of collisions among N particles. This is the number of colliding pairs to be selected in a cell at each simulation time step, which has a length of t. The $\langle v_r \rangle$ term, however, is computationally expensive. To bypass this term but generate the similar number of collisions during t, we use program to select $N_{candidate}$ pairs of candidate particles for collisions. The ratio of N_{coll} to $N_{candidate}$ is approximately:

$$\frac{N_{coll}}{N_{candidate}} \approx \frac{\langle v_r \rangle}{v_{\max}} \tag{4.52}$$

The number of collision candidate to be selected from the particles in the cell becomes:

$$N_{candidate} \approx \frac{N^2}{2V}\pi D^2 v_{\max} t \tag{4.53}$$

At each time step, according to the above equation, the program randomly selects $N_{candidate}$ particles from a cell, and these particles are screened based on the 5-steps procedures mentioned above. The average number of particle pairs selected to collide will eventually approach the theoretical value N_{coll}. An overly estimated ν_{max} does not affect the average number of collisions in a cell.

4.5.5 Simulation Results

4.5.5a Programming Setup

Figure 4.27 shows the layout of the simulation space for our model. Because the micro-turbine was axially symmetric, we reduced the simulation space to a quarter of the turbine cross-section by using two axial periodic boundaries. The simulation space was also limited by an isothermal reservoir, which is an arc of radius D. We let D equals four times of the radius of the turbine (1mm). The reservoir temperature was 25°C. The hot and cool surfaces at the blade were setup as thermal wall boundaries of constant temperatures 100°C and 25°C, respectively. The hot temperature was selected to be sufficiently lower than the melting points of most polymers (>150°C).

Figure 4.28 shows our testing of the simulation program. Figure 4.28(a) shows 500 simulated particles out of a total number 500,000. In front of the computer monitor, we were able to watch the movement of these simulated particles, the collisions among particles, the passing of periodic boundaries, and also the reflection of particles by thermal walls. Figure 4.29(b) to (d) show our study of single particle motion under different air pressures. The routes recorded the positions of the particles. Notice that Figure 4.29(b) shows a periodic-boundary-crossing by the particle. Each bending at the particle route indicates one collision. We found that the simulation results matched well with the theoretical values of mean free path (MFP) under different pressures. We found that while the particle under 10 mTorr could travel across the simulation space without collision, the particles under higher air pressures had more frequent collisions and were confined to local regions.

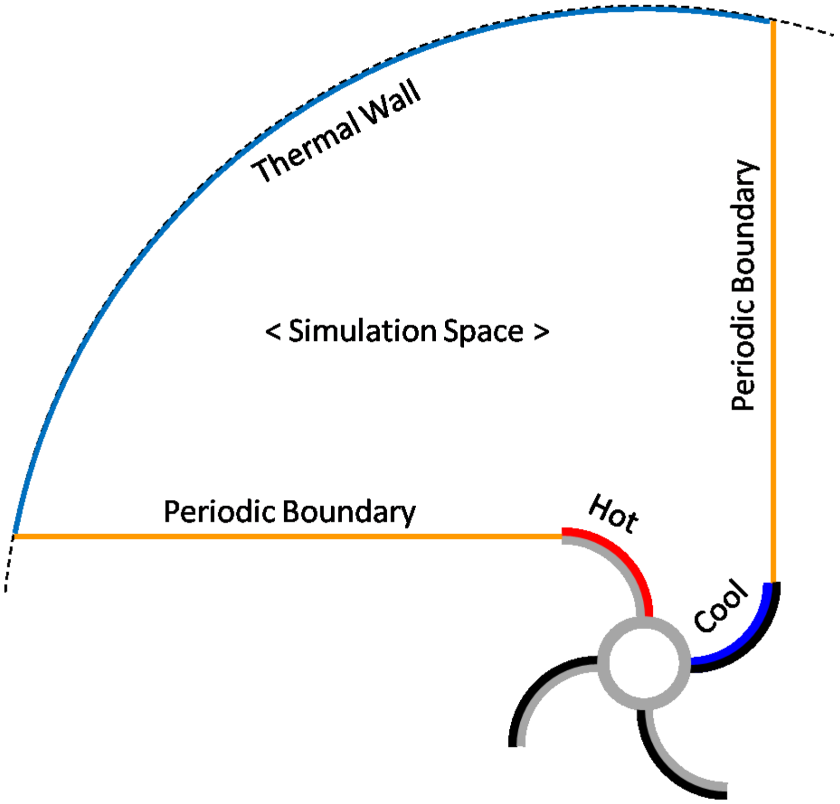

Figure 4.27 The simulation space covers only one quarter of the turbine cross-section by using periodic boundaries. A simulated particle crossing one of the periodic boundaries will be transferred to its counterpart. The thermal wall was located four radius (of turbine) away from the central of the turbine. We assumed that this distance is far enough to build an isothermal boundary condition. The hot and cool surfaces on the turbine blades were also modeled with thermal walls.

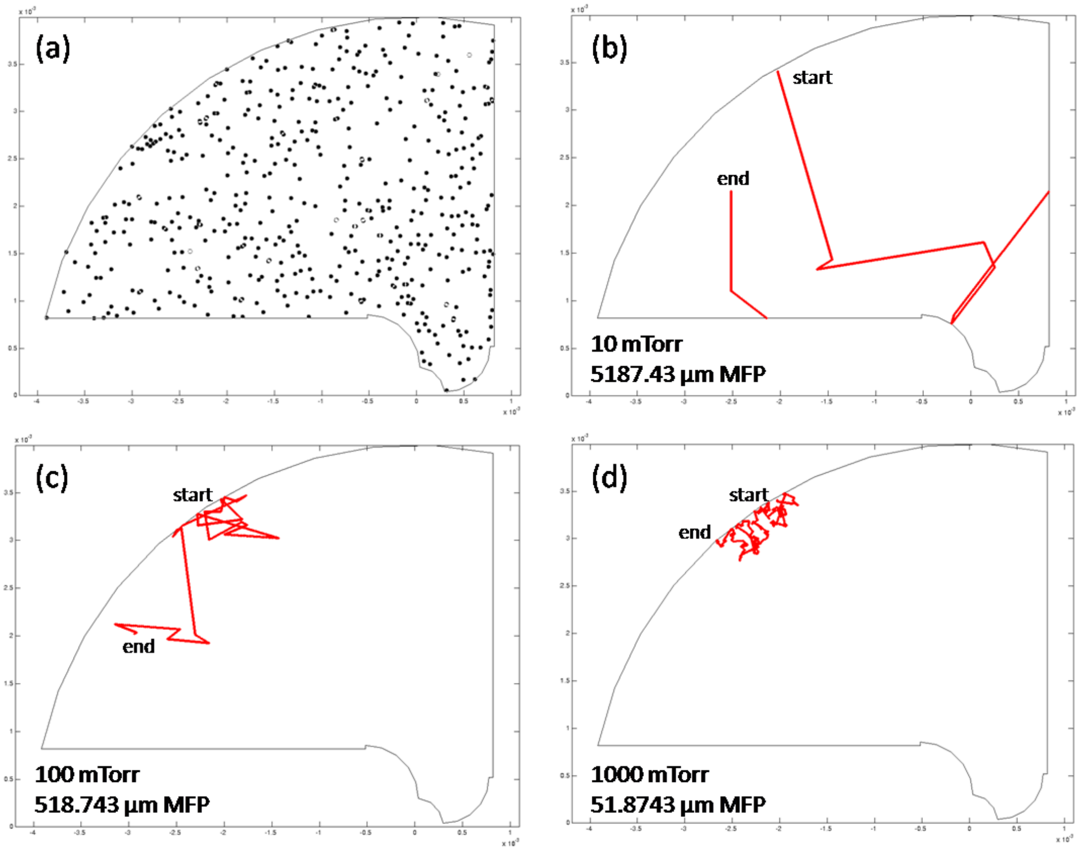

Figure 4.28 The movements of simulated particles were monitored during the simulation (a). The effect of simulated molecular collisions was checked by watching the route of single simulated particle (b to d). Note that the radius of the isothermal reservoir boundary was 4000 µm. The simulated straight distance of single particles matched well with the theoretical calculations of MFP (shown) at different pressures. The effect of particle-transfer by the periodic boundaries was also tested (b).

4.5.5b The Simulated Torques to the Micro-turbine under Several Air Pressures

We simulated the gas dynamics around the turbine under several different pressures: 10 mTorr, 100 mTorr, 400 mTorr, and 1000 mTorr. In each simulation, the gas molecules inside the simulation space were representative by 500,000 simulated particles. The effective hard-sphere constants, such as effective radius of air, were given by reference [4] and are listed in Table 4.1. The simulation procedure followed the flowchart in Figure 4.3. The most important output from this simulation was the torque applied at the micro-turbine by the gas molecules. The torque at the turbine comes from the striking of particles against the blades. We calculated the torque as following. If n is the number of particles that strike the turbine during a simulation time step τ, the torque is calculated by:

$$Torque(t) = 4 \cdot \frac{m_{air} N_{eff}}{\tau} \cdot \frac{\ell}{d} \sum_{i}^{n} \vec{x}_i \times \Delta \vec{v_i} \tag{4.54}$$

Where t is a simulated time, m_{air} is the effective molecular weight of air, N_{eff} the number of real molecules that each simulated particle represents, $\vec{x}_i$ the position where a particle strikes the turbine, ℓ the length of the micro-turbine (3 mm), d the dimension of cell, and $\Delta \vec{v_i}$ the velocity change at the particle upon striking. The constant "4" took account the number of blades. The calculated values of torque were averaged over the whole simulation time. We selected the simulated time for each modeling to be 0.001 second, a time length at which the average value of simulated torque became stable and the calculated special properties, such as temperature, formed smooth distributions over the simulation space.

To accurately calculate the torque generated by heating, we did a second group of simulation to model the air dynamics around an unheated micro-turbine. We simulated with the same setup but changed blade temperatures: both sides of the blades were at 25°C. The values of torque calculated from the second group of simulation (which did not equal zeros due to the inherited error of DSMC method) was subtracted from the result of the first group to give a corrected torque $Torque_{corrected}$:

$$Torque_{corrected} = Torque_{hot,cool} - Torque_{cool,cool} \tag{4.55}$$

The notation "hot, cool" in the above equation means the torque was from the model having hot and cool sides on the turbine blades; "cool, cool" means the torque from the modeling of an unheated micro-turbine.

The simulated $Torque_{corrected}$ at the micro-turbine is shown in Figure 4.29. The result shows that the simulated micro-turbine was under a torque of positive value, which means the rotating direction of the simulated micro-turbine will be counter-clockwise, and that the turbine will be rotating with the hot side (or convex side) retreating from a heating light source. Comparing the calculated torques under the four different air pressures, we also found that the rotating speed is maximized when the air pressure is about 400 mTorr, at which the mean free path of air molecules is about 130 μm and is roughly double the thickness of the blade of the micro-turbine (75 μm). The simulated rotation direction and the simulated optimized air pressure are both consistent with our experimental result shown in section 4.4. In the next section, we will use the simulated distributions of collision numbers, particle velocities, and particle densities to explain the light-driven rotation of the micro-turbine.

Table 4.1 The Hard-Sphere Constants for Air

Constant	Description	Value	Unit
m_{eff}	Effective molecular mass of air	4.8×10^{-26}	kg
n_{eff}	Effective number density of air molecule at 760 Torr and 0°C (or 273.15°k)	2.687×10^{25}	m^{-3}
D_{eff}	Effective diameter of air molecule	3.66×10^{-10}	m

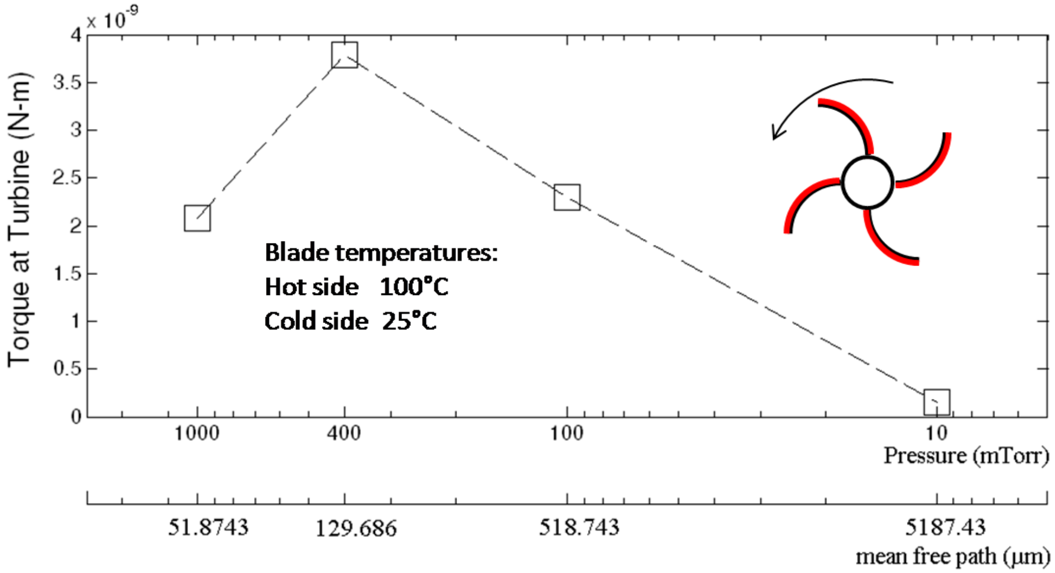

Figure 4.29 Simulation result: the torque at the turbine is counter-clockwise such that the turbine will rotate with the hot (convex) side of blade retreating from a heating light source. The simulation also shows that the rotation speed is maximized under a pressure around 400 mTorr, at which the mean free path of air is roughly double the thickness of the turbine blade. This simulated data is consistent with our experiment result in section 4.4.

4.5.5c Explanation of the Experimental Data

Figure 4.30(a) shows the distribution of spatial properties around a hot-and-cold micro-turbine at the air pressure of 1000 mTorr. The figure shows the distribution of collision frequency (as the number of collision per second per sampling cell) over the simulation space; the figure also includes the average gas momentum (in $kg.m/s$) at each sampling cell. Figure 4.30(b) shows the result from the same condition as in Figure 4.30(a), except that the temperatures at both sides of turbine blade were equally 25°C. Note that the particle movements around the edge of the turbine blade formed strong, initial momentum flow before the temperature difference was added; adding temperature difference biased the average flow around the blade, but the effect is not obvious from Figure 4.30(a). To focus on the momentum created by heating, we subtracted the momentum filed in Figure 4.30(a) by that of Figure 4.30(b) and got the distribution of a forced-momentum field shown in Figure 4.30(c). The result shows that the temperature different across the turbine blade adds a clockwise angular momentum to the gas molecule around the turbine. Following the 3rd law of Newtonian mechanics, this result explains the formation of the counter-clockwise torque applied to the micro-turbine. The simulated momentum field and also the distributions of collision suggest the following mechanism behind the clockwise motion of the simulated gas:

(1) The gas molecules heated by the hot side of one blade tend to flow toward the cool side of its neighboring blade due to higher momentum.

(2) Pushed by the molecules from the hot surface, the gas molecules at the cool surface tend to flow toward the blade's edge.

(3) After crossing the periodic boundary, the gas molecules arrived at the edge tend to move toward the hot side of the blade to fill the vacancy left by the gas molecules which are leaving the hot side.

(4) The gas movement builds a momentum cycle and generates torque.

We found that the continuity of the forced-momentum field was related to the frequency of collision. The collision frequency is proportional to the local density of simulated particles (Figure 4.31), which is higher in the space closer to the isothermal reservoir. In Figure 4.30(c), we see that the forced momentum filed is strongest and most continuous in the region next to the edge of the hot side of the blade. The momentum field becomes weaken and random in the region where the collision frequency becomes larger than about 2700 (per second per cell) or where the particle density is larger than 3.4×10^{22}(per cubic meter). At about 500 μm away from the micro-turbine, the elevated frequency of particle collisions stops the spread of momentum flow. The result from our study of particle movements at different gas pressures explains the limiting effect by collision frequency. Based on the study shown in Figure 4.28, the movements of particles are statistically confined to a dimension comparable to the theoretical mean free path. The transfer of momentum to a distance longer than the MFP is subjected to a high rate of particle collisions, which randomize and weaken the flow of momentum.

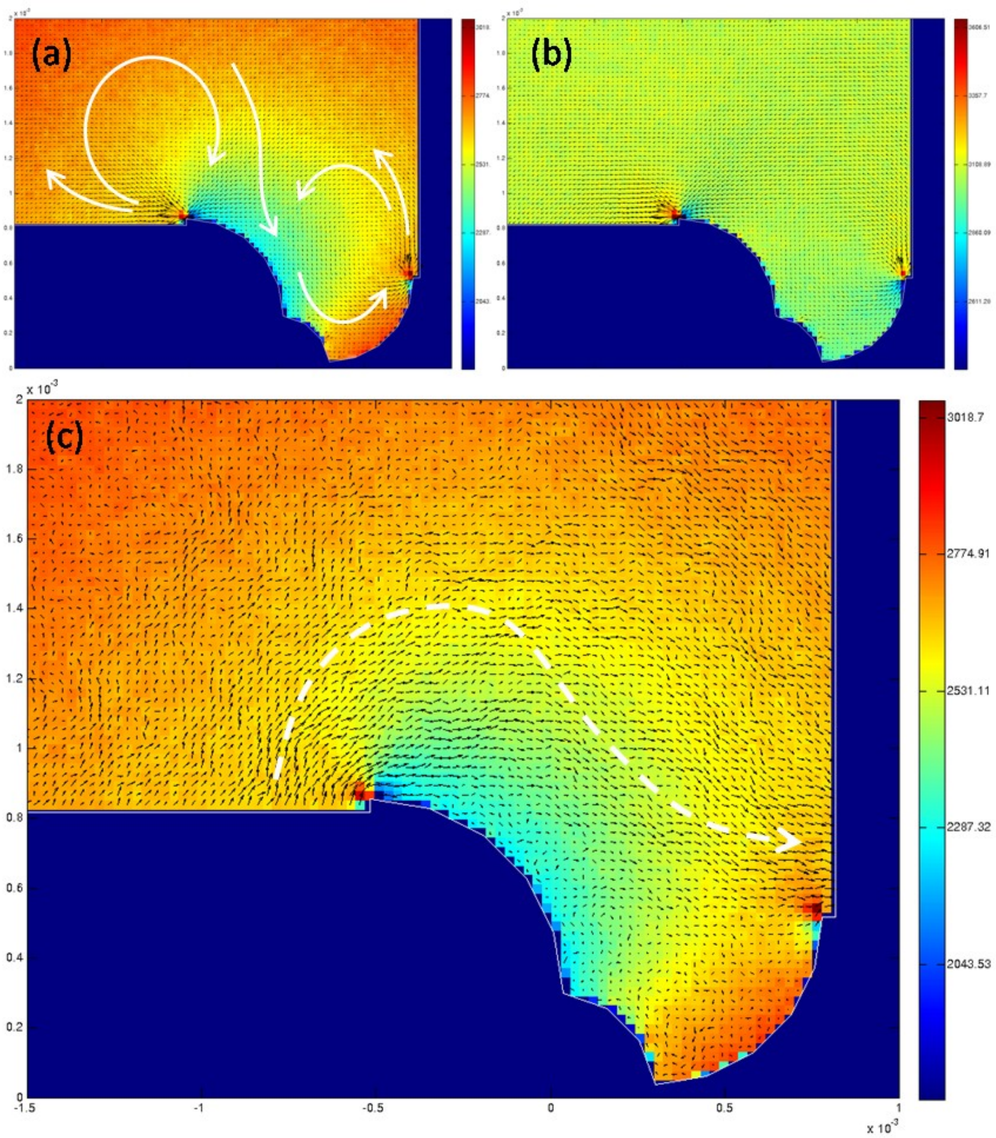

Figure 4.30 These figures show the simulated collision distribution, flows of gas momentum (a, b), and the flows of forced momentum caused by temperature difference across the turbine blade (c). The white arrows mark the trends of the fields. The simulation pressure was 1000 mTorr.

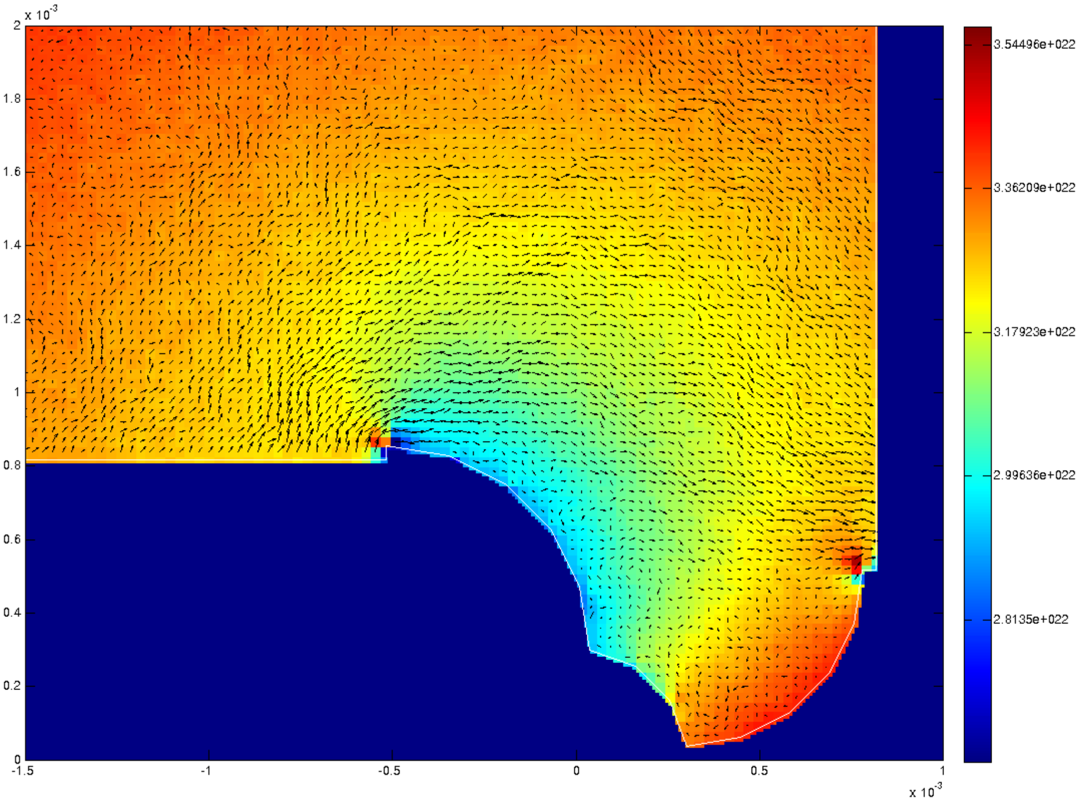

Figure 4.31 The simulated distribution of gas density (molecules per cubic meter) at 1000 mTorr is proportional to the collision distribution shown in Figure 4.30(c). This result is verified by the theoretical calculation of MFP.

4.4.5d Comparison between Simulation Results

We compared the simulation result from Figure 4.30 with the other simulations. Figure 4.32 shows the forced momentums at 400 mTorr. Compared to the gas at 1000 mTorr, the gas molecules at 400 mTorr were able to expand the flows of forced momentum wider, not only further apart from the turbine but also closer to the blade surface. Following our previous discussion, the gas molecules at 400 mTorr have a larger MFP and are more able to maneuver around the edges of the turbine blades, enhancing the circulation of momentums. Further reduction of gas pressure caused a negative effect. Figure 4.33 shows that the flows of forced momentum fade when the pressure is too low. In the case of 10 mTorr, the continuity of the forced momentum becomes non-observable. We found that the decay of forced momentum was caused by the overly low frequency of collision in the diluted gas; the particles move too randomly to build a well-defined momentum flow. Fewer gas molecules also give less force to the micro-turbine. Our simulation explains the optimized gas pressure for the light-driven micro-turbine. The optimization is from a maximized flow of forced momentum in the surrounding gas. To enhance the flow of forced momentum, one needs to seek a balance between the frequency of particle collision and the mobility of molecules. We also found a rule of thumb for the design of micro-turbine: the blade thickness should be about $1/2$ of the MFP of the gas molecules, such that a continuous flow of forced momentum can be built across the blade and drive the turbine at a maximum speed.

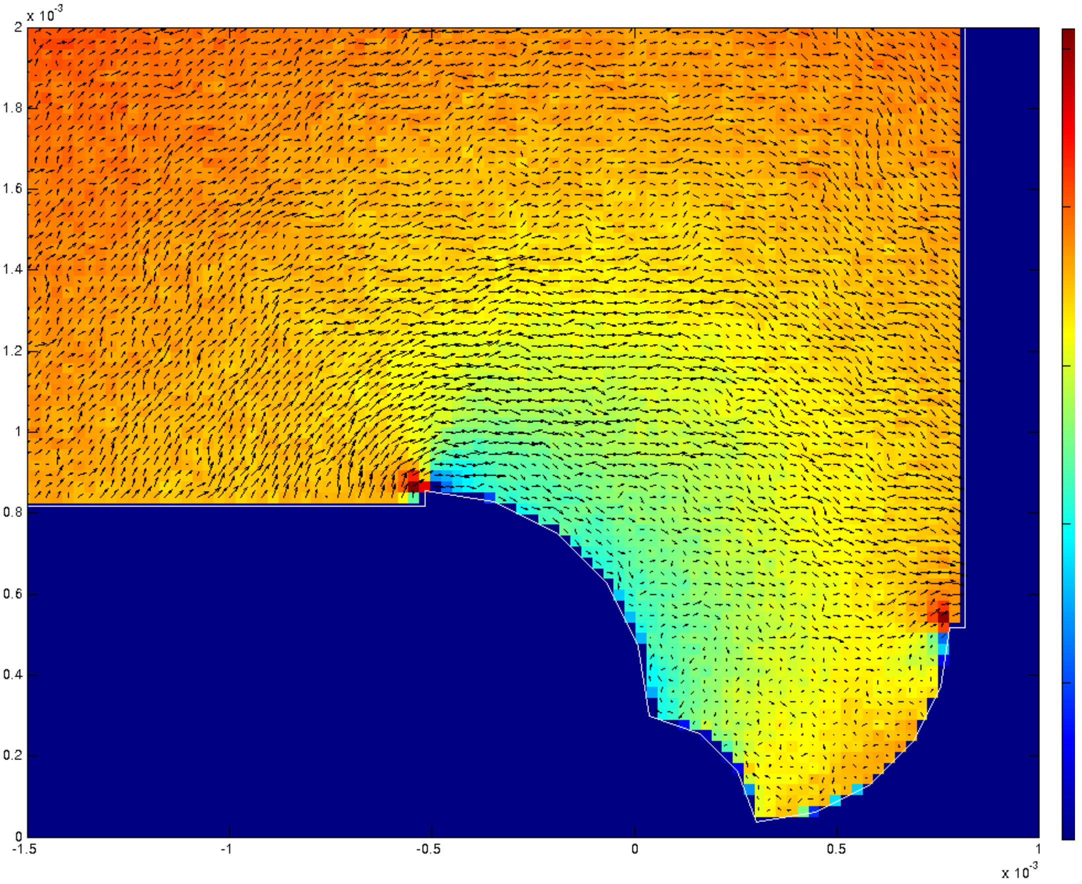

Figure 4.32 Compared to the gas at 1000 mTorr, the gas molecules at 400 mTorr were able to expand the range of continuous forced momentum wider, not only further apart from the turbine but also closer to the blade surface of the turbine. The micro-turbine at 400 mTorr thus gains a higher torque.

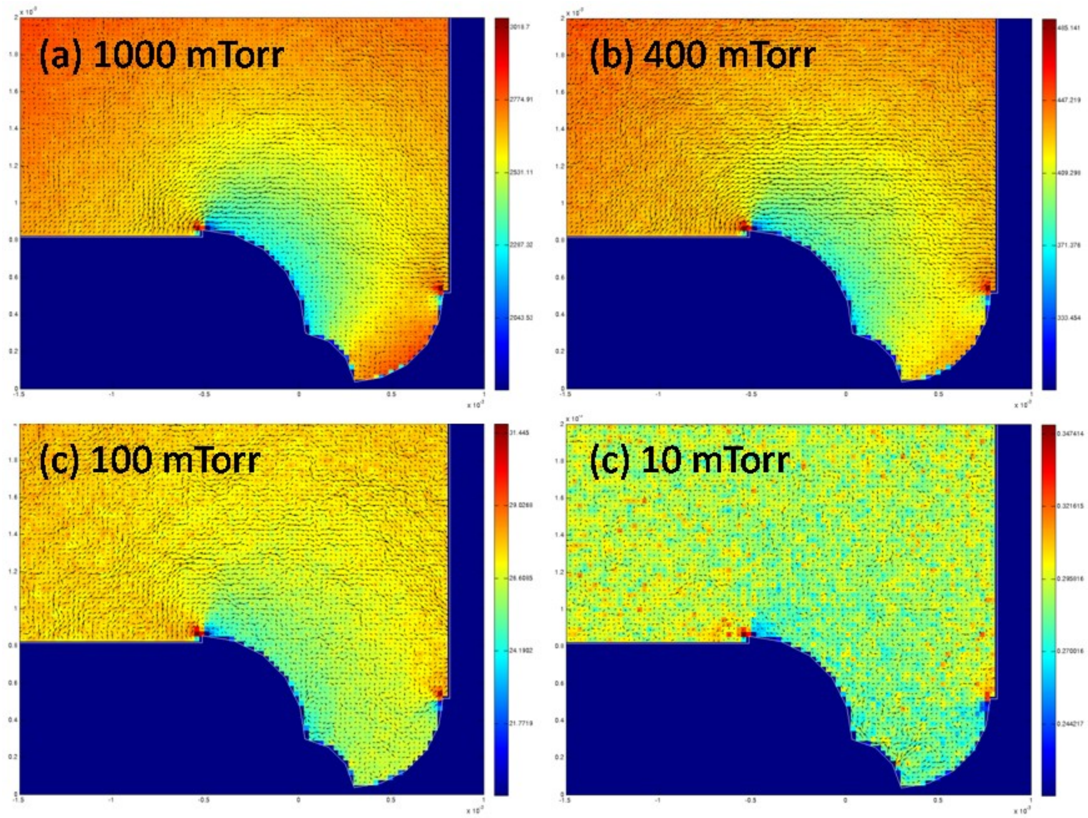

Figure 4.33 The strength of forced momentum fades when the pressure falls below 100 mTorr. In the case of 10 mTorr, the continuity of the forced momentum becomes non-observable from our simulation result.

4.4.5e The Roles of Blade Curvature and Temperature

We briefly studied the effect of reversing the blade curvatures and changing the temperatures of the micro-turbine. Figure 4.34(a) shows the forced flow vs. temperature distribution in a turbine of inversed blade temperatures. The air pressure is at 400 mTorr. The temperature at the convex side is 25˚C, and the concave side is at 100 ˚C. The result shows that a continuous forced momentum was developed successfully. Figure 4.34(b) shows the same turbine with both sides of the blades heated to 100 ˚C; the result shows that the development of a forced momentum was inefficient.

The values of calculated torques at the turbines of different heating conditions are compared in Table 4.2. The comparison shows that the temperature difference across the blade is important to drive the micro-turbine, even though the curvature of the blades can generate a minor effect. The result also shows that the turbine heated at the concave sides of the blades can rotate slightly faster than being heated at the convex sides of the blades. In our realistic design, however, the Au-nanoparticles are preferably coated at the convex side to gain a higher light exposure.

Table 4.2 Effect of different design of the micro-turbine at 400 mTorr

Surface Temperature (Convex)	Surface Temperature (Concave)	Torque (N-m)
100 ˚C	25 ˚C	3.7896×10^{-9}
25 ˚C	100 ˚C	-3.9220×10^{-9}
100 ˚C	100 ˚C	-0.30913×10^{-9}

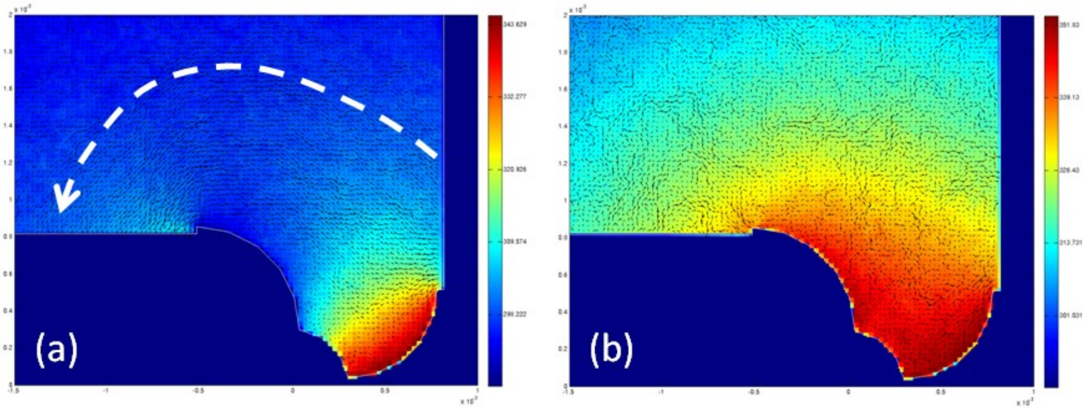

Figure 4.34 The gradient shows the temperature distribution over the simulation space. By heating the concave side of the turbine (a), the forced momentum is switched to counter-clockwise direction, giving the microturbine a clockwise torque. This torque is slightly larger than that created by heating the convex side (see Table 4.2). When both sides of the turbine blade are heated, the development of a forced momentum becomes inefficient, and the driving torque becomes one order lower. Compared to the temperature, the curvature of the turbine plays a minor role in the light-driving effect.

4.6 Conclusion

Many different topics were included at this chapter; these topics, however, are related to the design, fabrication, testing, and simulation of a micro-turbine driven by light. The setup and fabrication process using a DMD system were introduced. Examples were shown to highlight the capacity of this DMD system for three-dimensional, heterogeneous fabrication of polymeric microstructures. We successfully used the DMD system to combine two different materials and build the light-driven micro-turbine; one of the materials is an active chemical, ready for further modification. Formed by the active material, the convex side of the turbine blade was coated with PEI which reduces gold from a precursor. Gold nanoparticles were then built on the convex surfaces to absorb heat from a light source. Our experiment showed that the micro-turbine started to rotate under light exposure when the surrounding pressure was below 1000 mTorr, and the speed was maximized at about 400 mTorr, at which the theoretical mean free path of air is roughly twice the thickness of the turbine blades. Gas dynamics simulation based on the DSMC method yielded results which were very consistent with our experimental data. The simulation results were used to explain the mechanism behind the light-driving phenomenon, in which the mean free path of gas molecules and also the blade thickness take important roles.

4.7 References

1. Alexandrou, A. *Principles of Fluid Mechanics.* Upper Saddle River : Prentice-Hall, 2001. pp. 203-208.
2. Huang, K. *Statistical Mechanics.* 2. New York : John Wiley & Sons, 1987. p. 125.
3. Huang, K.. *Statistical Mechanics.* 2. New York : John Wiley & Sons, 1987. p. 93.
4. Bird, G. A. *Molecular Gas Dunamics.* Oxford : Clarendon Press, 1976. pp. 17-21.
5. Garcia, A. L. *Numerical Methods for Physics.* NJ : Prentice-Hall, 1994. pp. 319-347.
6. Han, L., Mapili, G., Chen, S.C., Roy, K., 2008, "*Projection Micro-Printing of Three-Dimensional Scaffolds for Tissue Engineering,*" Journal of Manufacturing Science and Engineering, **130**, pp. 021005-1-4.
7. Wu, S., Han, L., and Chen, S.C., 2009, "*Three-dimensional selective growth of nanoparticles on a polymer microstructure,*" Nanotechnology, **20**, p. 285312.
8. Lin, M. W., et al., 2008, "*Interfacial adhesion studies for step and flash imprint lithography,*" Proceedings of the SPIE, **6921**, pp. 69210E-69210E-12.
9. Palsson, B. and Bhatia, S.N., 2004, Tissue Engineering, Pearson Education, pp. 252-269.
10. Palsson, B. and Bhatia, S.N., 2004, Tissue Engineering, Pearson Education, pp. 172-188.
11. Palsson, B. and Bhatia, S.N., 2004, Tissue Engineering, Pearson Education, pp.172-188.
12. Madou, M. J. *Fundamentals of Microfabrication: the Science of Miniaturization. 2001,* New York, CRC Press, pp. 367-368.
13. Madou, M. J. *Fundamentals of Microfabrication: the Science of Miniaturization. 2001,* New York, CRC Press, pp. 183-249

14. Kelly, R.T., Pan, T. and Woolley, A.T., 2005, "*Phase-Changing Sacrificial Materials for Solvent Bonding of High-Performance Polymeric Capillary Electrophoresis Microchips,*" Analytical Chemistry, **77**, pp. 3536-3541.
15. Golden, A.P. and Tien, J., 2007, "*Fabrication of microfluidic hydrogels using molded gelatin as a sacrificial element,*" Lab on a Chip, **7**, pp. 720-725.
16. Calvert, S. and Englund, H.M., 1984, Handbook of Air Pollutio, Wiley, p. 103.
17. Einstein, A. 1924, Z. Physik, **27**.
18. Huang, K., 1987, Statistical Mechanics. John Wiley & Sons, New York, pp. 56-59.
19. Garcia, A.L. 1997, "*Direct Simulation Monte Carlo: Novel Applications and New Extensions,*" Proceedings of the 3rd Workshop on the Modeling of Chemical Reaction Systems.
20. Bird, G. A., 1976, Molecular Gas Dynamics,. Clarendon Press, Oxford, p. 311.
21. Alexandrou, A., 2001, Principles of Fluid Mechanics. Prentice-Hall,. Upper Saddle River, p. 503.
22. WIKIPEDIA. (Online) http://en.wikipedia.org/wiki/Crookes_radiometer.

Chapter 5: Conclusions

The design, fabrication, and mathematical modeling of three different light-driven microactuators were discussed in this dissertation. Experimental investigation and theoretical analysis of these microactuators showed interesting results, and these different studies have brought new concepts for the design and fabrication of miniature mechanical systems.

5.1 Coupling of Multiple Physics Effects in Light-driven Microactuators

Each of the microactuators was functioned based on cross-linked, multiple physics phenomenon. The microcantilever was activated under the coupling effects of photo-heating and thermal expansion. The photo-tunable microshells were based on both photo-chemistry effect and mechanical-deformation-induced plasomonics enhancement. The light driven microturbine was actuated by plasomonic enhancement among nanoparticles, which caused thermal convection in the surrounding rarefied gas molecules. These multiple physics effects dominate the function of a mechanical system, when the system size becomes small.

5.2 Importance of Microscopic Mathematical Modeling

The mathematical modeling of this dissertations showed that the effective theoretical models to explain the physics of miniature mechanical system could be very different from those for large scale counterparts. When light is projected onto a smooth surface coated by a gold film, for example, its optical effect can be calculated easily using a reflectivity constant, and the interaction between the gold film and its surroundings medium can be described using a smooth boundary between two spaces of distinct dielectric constants. In the study of Au microshells, however, the enhancement of electromagnetic field dominated the optical property, and electrodynamics calculation must be used to take account the size of gold nanospheres, which were smaller than the wavelength of light. It is also necessary to consider the nonlinearly enhanced absorption by surrounding medium, which stems from the field enhancement by the nanospheres. The modeling of light-driven microturbine also showed the importance of using microscaled gas dynamics to take account a system dimension smaller than the mean free path of surrounding gas.

This dissertation suggests that, to simulate a microscale mechanical system accurately, one has to take account the minimum dimension of the system and to consider if the bottom-line assumption of a theoretical model is valid for the microsystem. In the case of microturbine, for example, using Navier-Stoke theory to explain the dynamics of rarefied gas is invalid, because the Navier-Stoke equation is based on an assumption of continuous system gradients; this assumption fails when the molecules within a characteristic dimension are subject to major fluctuations of different properties.

5.3 There's Plenty of Room at the Bottom [1]

This dissertation highlighted the multi-physics nature of microactuators. Learned from the nature, one can see that biological microactuators normally functions by closely combined physics phenomena. For example, the rotating motion of ATPase [2], a biological micromotor, stems from interconnected chemical and mechanical effects. ATPase operates by the oxidation of adenosine triphosphate (ATP), which causes a conformation change in the protein and induces the rotation of a separated part in ATPase. Study elsewhere [3] also suggests that the function of ATPase can be accelerated by photons, which brings ATP molecule to a less stable energy state; an ATPase could be driven by light.

A man-made micro- or nano-actuator could be invented based on similar mechanism for biological microactuators. The key is fabrication apparatus. The DMD system used in this dissertation can build 3D, heterogeneous microactuator in the resolution of 10 micrometers. In the future, one can expect to see a technology capable of making microactuators comparable to the size of biological proteins; the driving mechanism for the microactuator could be based on the similar mechanism for the biological organisms. Studies for this kind of fabrication have already begun [4].

5.4 Reference

1. Quoted from Richard Feynman, in a speech given on December 29th, 1959, at the annual meeting of the American Physical Society at the California Institute of Technology.
2. D. Voet and J. G. Voet, 1990, Biochemistry, John Wiley & Sons, Canada, pp.493-96.
3. A. Ama, J. Rigau, R. W. Waynant, I. K. Ilev and J. J. Anders, 2006, 'The electric field induced by light can explain cellular responses to electromagnetic energy: A hypothesis of mechanism,' J. Photochem. Photobiol. B, **82**, pp. 152-160.
4. H. J. Kwon, K. Shikinaka, A. Kakugo, J. P. Gong, and Y. Osada, 2007, "Gel biomachine based on muscle proteins", Polymer Bulletin **58**, pp. 43–52.

Bibliography

A. Ama, J. Rigau, R. W. Waynant, I. K. Ilev and J. J. Anders, 2006, 'The electric field induced by light can explain cellular responses to electromagnetic energy: A hypothesis of mechanism,' J. Photochem. Photobiol. B, **82**, pp. 152-160.

A. Camposeo, N. Puccini, F. Fuso, M. Allegrini, E. Arimondo, A. Tuissi, *Laser deposition of shape-memory alloy for MEMS applications*, Appl. Surf. Sci. 208–209 (2003) 518–521.

Alexandrou, A. *Principles of Fluid Mechanics.* Upper Saddle River : Prentice-Hall, 2001. pp. 203-208.

Alexandrou, A., 2001, Principles of Fluid Mechanics. Prentice-Hall,. Upper Saddle River, p. 503.

Bachelot R, H'Dhili F, Barchiesi D, Lerondel G, Fikri R, Royer P, Landraud N, Peretti J, Chaput F, Lampel G, Boilot J and Lahlil K 2003 *J. Appl. Phys.* **94** 2060.

Banerjee, M., Datta, S. K., Saha, H., 2005, "Enhanced optical absorption in a thin silicon layer with nanovoids," Nanotechnology, **16**(9), pp. 1542-1548.

Bird, G. A. Molecular Gas Dunamics. Oxford : Clarendon Press, 1976. pp. 311.

Bird, G. A. *Molecular Gas Dunamics.* Oxford : Clarendon Press, 1976. pp. 17-21.

Bird, G. A., 1976, Molecular Gas Dynamics,. Clarendon Press, Oxford, p. 311.

C. Sones, S. Mailis, V. Apostolopoulos, I.E. Barry, C. Gawith, P.G.R. Smith, R.W. Eason, *Fabrication of piezoelectric micro-cantilevers in domain-engineered LiNbO3 single crystals*, J. Micromech. Microeng. 12 (2002) 53–57.

C.A. Savran, A.W. Sparks, J. Sihler, J. Li, W. Wu, D.E. Berlin, T.P. Burg, J. Fritz, M.A. Schmidt, S.R. Manalis, *Fabrication and characterization of a micromechanical sensor for differential detection of nanoscale motions, J. Microelectromech*. Syst. 11 (2002) 703–708.

Calvert, S. and Englund, H.M., 1984, Handbook of Air Pollutio, Wiley, p. 103.

Caruso F 2000 *Chem. Eur. J* **6** 413.

Chern, R., Liu, X., and Chang, C. 2007" Particle plasmons of metal nanospheres: Application of multiple scattering approach," *Phys. Review E* **76**, pp. 016609.

Choi, J.; Yamaguchi, J.; Morales, S.; Horowitz, R.; Zhao, Y.; Majumdar, A., 2003, "*Design and control of a thermal stabilizing system for a MEMS optomechanical uncooled infrared imaging camera,*" Sens. Actuators A, **104**, pp.132–142.

Chung D, Fukuda T, Takanishi Y, Ishikawa K, Matsuda H, Takezoe H and Osipov M A 2002 *J. Appl. Phys.* **92** 1841.

Craig F B and Donld R H 1983 Absorption and Scattering of Light by Small Particles, John Wiley & Sons, Canada, 325-29.

Craig F B and Donld R H 1983 *Absorption and Scattering of Light by Small Particles,* John Wiley & Sons, Canada, 136-39.

D. Karnopp, D.L. Margolis, R.C. Rosenberg, System Dynamics—Modeling and Simulation of Mechanical System, Wiley, 2000, pp.124.

D. Karnopp, D.L. Margolis, R.C. Rosenberg, System Dynamics—Modeling and Simulation of Mechanical System, Wiley, 2000, p.124.

D. Voet and J. G. Voet, 1990, Biochemistry, John Wiley & Sons, Canada, pp.493-96.

Decher G 1997 *Science* **277** 1232.

Decher G, Hong J D and Schmitt J 1992 *Thin Solid Films* **210** 831.

E.A. Wachter, T. Thundat, P.I. Oden, R.J. Warmack, P.G. Datskos, S.L. Sharp, Remote optical detection using microcantilevers, Rev. Sci. Instrum. 67 (1996) 3434–3439.

Einstein, A. 1924, Z. Physik, **27**.

F.P. Incropera, D.P. De Witt, Fundamentals of Heat and Mass Transfer, Wiley, New York, 1990.

Feringa B L 2001 *Molecular Switches* WILEY-VCH GmbH Weinheim Germany 399.

Feringa B. L., 2001, Molecular Switches, Wiley-VCH, GmbH, Weinheim, Germany, pp.399.

Garcia, A. L. *Numerical Methods for Physics.* NJ : Prentice-Hall, 1994. pp. 319-347.

Garcia, A.L. 1997, "*Direct Simulation Monte Carlo: Novel Applications and New Extensions,*" Proceedings of the 3rd Workshop on the Modeling of Chemical Reaction Systems.

Garcia, Alejandro L. Numerical Methods for Physics. NJ : Prentice-Hall, 1994. pp. 319-347.

Golden, A.P. and Tien, J., 2007, "*Fabrication of microfluidic hydrogels using molded gelatin as a sacrificial element,*" Lab on a Chip, **7**, pp. 720-725.

H. Goldstein, Classical Mechanics, Addison-Wesley, 1950, p. 347.

H. Goldstein, Classical Mechanics, Addison-Wesley, 1950, p. 347.

H. J. Kwon, K. Shikinaka, A. Kakugo, J. P. Gong, and Y. Osada, 2007, "Gel biomachine based on muscle proteins", Polymer Bulletin **58**, pp. 43–52.

Han L, Tang T, Chen S and Webber S E 2005 *International Conference on Bio-Nano-Information Fusion*, *LA,* USA.

Han, L, et al. 2008, "*Projection Micro-Printing of Three-Dimensional Scaffolds for Tissue Engineering*." Journal of Manufacturing Science and Engineering, **130**, pp. 021005-1-4.

Han, L., Mapili, G., Chen, S.C., Roy, K., 2008, "*Projection Micro-Printing of Three-Dimensional Scaffolds for Tissue Engineering,*" Journal of Manufacturing Science and Engineering, **130**, pp. 021005-1-4.

Huang, K. *Statistical Mechanics.* 2. New York : John Wiley & Sons, 1987. p. 125.

Huang, K., 1987, Statistical Mechanics. John Wiley & Sons, New York, pp. 56-59.

Huang, K.. *Statistical Mechanics.* 2. New York : John Wiley & Sons, 1987. p. 93.

Huang, Kerson. Statistical Mechanics. 2. New York : John Wiley & Sons, 1987. pp. 56-59.

Huang, T.T; Mosier, N.S.; Ladisch, R.L, 2006,"*Surface engineering of microchannel walls for protein separation and directed microfluidic flow*", Journal of Separation Science, 29, 1733-42.

Ikeda T, Nakano M, Yu Y, Tsutsumi O and Kanazawa A 2003 *Adv. Mater.* **15** 201.

J. Choi, J. Yamaguchi, S. Morales, R. Horowitz, Y. Zhao, A. Majumdar, *Design and control of a thermal stabilizing system for a MEMS optomechanical uncooled infrared imaging camera*, Sens. Actuators A 104 (2003) 132–142.

J.H. Williams Jr., Fundamentals of Applied Dynamics, Wiley, 1996.

J.M.Z. Ocampo, P.O. Vaccaro, T. Fleischmann, T. Wang, K. Kubota, T. Aida, T. Ohnishi, A. Sugimura, R. Izumoto, M. Hosoda, S. Nashima, *Optical actuation of micromirrors fabricated by the microorigami technique*, Appl. Phys. Lett. 83 (2003) 3647–3649.

Jackson J D 1999 Classical Electrodynamics 3rd ed John Wiley & Sons, USA, pp. 407-411.

Jackson J D 1999 Classical Electrodynamics 3rd ed John Wiley & Sons, USA, 407-411.

Jackson J D 1999 *Classical Electrodynamics* 3rd ed John Wiley & Sons, USA, 309-313.

Jackson, J. D. 1999, *Classical Electrodynamics* 3rd ed John Wiley & Sons, USA, pp. 352-56.

Joannnopoulos J D, Meade R D and Winn J N 1995 *Photonic Crystal: Molding the Flow of Light* Princeton University Press Princeton NJ.

Johnson P B and Christy R W 1972 *Phys. Rev. B* **6** 4370-9.

Johnson, P. B. and Christy, R. W., 1972, "Optical Constants of the Noble Metals," *Phys. Rev. B*., 6, pp. 4370-79.

Kawata, S., 2001, Near-Field Optics and Surface Plasmon Polaritons, Springer, New York.

Kelly, R.T., Pan, T. and Woolley, A.T., 2005, "*Phase-Changing Sacrificial Materials for Solvent Bonding of High-Performance Polymeric Capillary Electrophoresis Microchips,*" Analytical Chemistry, **77**, pp. 3536-3541.

Kittel, C., 1971, Introduction to Solid State Physics 4th ed. Wiley Canada, pp. 248.

Kreibig, U. and Vollmer, M., 1995 Optical Properties of Metal Clusters, Springer, New York.

L.G. Shamanaeva, *Thermooptical mechanism of sound generation by high-power laser radiation propagating in the atmosphere*, Russ. Phys. J. 44 (2001) 1187–1196.

Li M, Keller P, Li B, Wang X and Brunet M 2003 *Adv. Mater.* **15** 569.

Li Y, He Y, Tong X and Wang X 2005 *J. Am. Chem. Soc.* **127** 2402.

Lin, M. W., et al., 2008, "*Interfacial adhesion studies for step and flash imprint lithography,*" Proceedings of the SPIE, **6921**, pp. 69210E-69210E-12.

Mackowski, D. W. 1991 "Analysis of Radiative Scattering for Multiple Sphere Configurations," *Proceedings: Mathematical and Physical Sciences*, **433** (1889), pp. 599-614.

Mackowski, D. W. 1991 "Analysis of Radiative Scattering for Multiple Sphere Configurations," *Proceedings: Mathematical and Physical Sciences*, **433** (1889), pp. 599-614.

Madou, M. J. *Fundamentals of Microfabrication: the Science of Miniaturization. 2001,* New York, CRC Press, pp. 367-368.

Madou, M. J. *Fundamentals of Microfabrication: the Science of Miniaturization. 2001,* New York, CRC Press, pp. 183-249

Madou, M. J., 2001, Fundamentals of Microfabrication: the Science of Miniaturization. New York, CRC Press, pp. 1-71.

Madou, M. J., 2001, Fundamentals of Microfabrication: the Science of Miniaturization. New York, CRC Press, pp. 77-118.

Maier S A and Atwater H A 2005 Appl. Phys. Rev. **98** 011101-1-10.

MatWeb, http://www.matweb.com/.

Mayya K S, Gittins D I, Dibaj A M and Caruso F 2001 *Nano. Lett.* **1** 727.

Mie G 1908 "Beiträge zur Optik trüber Medien speziell kolloidaler Metallösungen" *Ann. Phys.* **25** 376-445.

Mie, G., 1908, "Beiträge zur Optik trüber Medien speziell kolloidaler Metallösungen," *Ann. Phys.* **25** 376-445.

Nomura W, Ohtsu M and Yatsui T 2005 *App. Phys. Lett.* **86** 181108.

P.V. O’Neil, Advanced Engineering Mathematics, Belmont, 3rd ed., 1991.

Palmer K F and Williams D 1974 *J. Opt. Soc. Am.* **64** 1107-1110.

Palsson, B. and Bhatia, S.N., 2004, Tissue Engineering*,* Pearson Education, pp. 252-269.

Palsson, B. and Bhatia, S.N., 2004, Tissue Engineering*,* Pearson Education, pp. 172-188.

Palsson, B. and Bhatia, S.N., 2004, Tissue Engineering*,* Pearson Education, pp.172-188.

R.W. Fox, A.T. McDonald, Introduction to Fluid Mechanics, Wiley, Canada, 1994, pp. 418–422.

Rechberger W, Hohenau A, Leitner A, Krenn JR, Lamprecht B and Aussenegg FR 2003 *Opt. Commun* .**220** 137–141.

Richard Feynman, in a speech given on December 29th, 1959, at the annual meeting of the American Physical Society at the California Institute of Technology.

S. Baglio, S. Castorina, L. Fortuna, N. Savalli, *Modeling and design of novel photo-thermo-mechanical microactuators*, Sens. Actuators A 101 (2002) 185–193.

S. Chen, C.P. Grigoropoulos, H.K. Park, P. Kerstens, A.C. Tam, *Photothermal displacement measurement of transient melting and surface deformation during pulsed laser heating*, Appl. Phys. Lett. 73 (1998) 2093–2095.

S. Timoshenko, *Analysis of bi-metallic thermostates*, J. Opt. Soc. Am. 11 (1925) 233.

S. Zhou, X. Sun, W.N. Carr, *A monolithic variable inductor network using microrelays with combined thermal and electrostatic actuation*, J. Micromech. Microeng. 9 (1999) 45–50.

Schmitt J, Mächtle P, Eck D, Möhwald H and Helm C A 1999 *Langmuir **15*** 3256-3266.

Schneider G and Decher G 2004 *Nano. Lett.* **4** 1833.

Segelstein, D., 1981, "The Complex Refractive Index of Water," M.S. Thesis, University of Missouri, Kansas City, Missouri, USA.

Shvalagin, V. V., Stroyuk, A. L., and Kuchmii, S. Y., 2007, “Photochemical synthesis *of ZnO/Ag nanocomposites,” J. Nanoparticle Research*, **9**(3), pp. 427-440.

Sukhorukov G B, Shchukin D G, Dong W, Möhwald H, Lulevich V V and Vinogradova O I 2004 *Macromol. Chem. Phys.* **205** 530.

Tamaru H, Kuwata H, Miyazaki H T and Miyano K 2002 *Appl. Phys. Lett.* **80** 1826.

Tian Y and Tatsuma T 2005 *J. Am. Chem. Soc.* **127** 7632 – 7637.

Tolga Atay T, Song J and Nurmikko A V 2004 *Nano. Lett.* **4** 1627-31.

Vandenbem, C. and Vigneron, J. P., 2005, “Mie resonances of dielectric spheres in face-centered cubic photonic crystals,” J. Opt. Soc. Am. A, **22** (6), pp. 1042-47.

W.D. Callister, Materials Science and Engineering: An Introduction, Wiley, New York, 2003.

Weaver, J. H. and Frederikse, H. P. R. 2001, Optical Properties of Selected Elements (82 Ed), CRC Press, Boca Raton, FL, USA.

WIKIPEDIA. (Online) http://en.wikipedia.org/wiki/Crookes_radiometer.

Wu, S., Han, L., and Chen, S.C., 2009, “*Three-dimensional selective growth of nanoparticles on a polymer microstructure,*” Nanotechnology, **20**, p. 285312.

Y. Li, Y. He, X. Tong, X. Wang, *J. Am. Chem. Soc.* **2005**, 127, 2402.

Yu Y, Nakano M and Ikeda T 2003 *Nature* **425** 145.

Yu, Y. and Ikeda, T., 2005, "*Photodeformable Polymers: A New Kind of Promising Smart Material for Micro- and Nano-Applications*", Macromolecular Chemistry and Physics, **206**, pp. 1705-08.

Vita

Li Hsin Han was born in Taipei, the Republic of China (Taiwan) on August 29th, 1974, to Sha and Yi Chung Han. He has a sister, Shawna Han, and a brother, Li Kang Han. He received his high school diploma from Taipei Chang Kuo High School in 1992.

From 1992 to 1996, he attended National Taiwan University (NTU) where he received a B.S. in Mechanical Engineering. He attended the graduate program of NTU for the next two years and received a M.S. in Mechanical Engineering in 1998, with specialization in Robotics. From 1998 to 2000, he joined the artillery force of ROC National Army, where he served as a platoon commander and also a 2nd lieutenant. After the military service, he became a patent agent and then a salesman from 2000 to 2002. He married Erica Tseng in 2002. They have two daughters, Camille Han and Kaelyn Han, who were born in 2007 and 2009.

In 2002, to pursue his Ph.D., he joined Dr. Shaochen Chen's research group in Mechanical Systems and Designs area within the Department of Mechanical Engineering. He also joined the Doctoral Nanotechnology Portfolio program at The University of Texas at Austin and graduated with a Certification in Nanotechnology in 2009.

Li Hsin is first author on four peer-reviewed journal papers and he co-authored several additional journal papers and conference proceedings. He received a Continuing Fellowship of UT Austin from 2006 to 2007. Three United States patents were awarded to Li Hsin for his work in catheter probe for cardiovascular imaging. Li-Hsin is also a casual violinist.

Permanent address: 12F-3, No. 3, Lane 29, San-Min Rd, Taipei, Taiwan

This dissertation was typed by Li Hsin Han.